

Nanoscale Biological Materials

Journal of Nanomaterials

Guest Editors: Kilho Eom, Serdal Kirmizialtin, Yaling Liu, and Zhiping Xu





Nanoscale Biological Materials

Journal of Nanomaterials

Nanoscale Biological Materials

Guest Editors: Kilho Eom, Serdal Kirmizialtin, Yaling Liu,
and Zhiping Xu



Copyright © 2016 Hindawi Publishing Corporation. All rights reserved.

This is a special issue published in "Journal of Nanomaterials." All articles are open access articles distributed under the Creative Commons Attribution License, which permits unrestricted use, distribution, and reproduction in any medium, provided the original work is properly cited.

Editorial Board

- Domenico Acierno, Italy
Katerina Aifantis, USA
Nageh K. Allam, USA
Margarida Amaral, Portugal
Martin Andersson, Sweden
Raul Arenal, Spain
Ilaria Armentano, Italy
Vincenzo Baglio, Italy
Lavinia Balan, France
Thierry Baron, France
Andrew R. Barron, USA
Hongbin Bei, USA
Daniel Bellet, France
Stefano Bellucci, Italy
Enrico Bergamaschi, Italy
Samuel Bernard, France
D. Bhattacharyya, New Zealand
Sergio Bietti, Italy
Giovanni Bongiovanni, Italy
T. Borca-Tasciuc, USA
Mohamed Bououdina, Bahrain
Torsten Brezesinski, Germany
C. Jeffrey Brinker, USA
Christian Brosseau, France
Philippe Caroff, Australia
Victor M. Castaño, Mexico
Albano Cavaleiro, Portugal
Bhanu P. S. Chauhan, USA
Shafiq Chowdhury, USA
Jin-Ho Choy, Republic of Korea
Kwang-Leong Choy, UK
Yu-Lun Chueh, Taiwan
Elisabetta Comini, Italy
Giuseppe Compagnini, Italy
David Cornu, France
M. A. Correa-Duarte, Spain
P. Davide Cozzoli, Italy
Shadi A. Dayeh, USA
Luca Deseri, USA
Yong Ding, USA
Philippe Dubois, Belgium
Zehra Durmus, Turkey
Joydeep Dutta, Oman
Ali Eftekhari, USA
Samy El-Shall, USA
- Ovidiu Ersen, France
Claude Estournès, France
Andrea Falqui, KSA
Matteo Ferroni, Italy
Elena J. Foster, USA
Ilaria Fratoddi, Italy
Alan Fuchs, USA
Miguel A. Garcia, Spain
Siddhartha Ghosh, Singapore
P. K. Giri, India
Russell E. Gorga, USA
Jihua Gou, USA
Jean M. Greneche, France
Smrati Gupta, Germany
K. Hamad-Schifferli, USA
Simo-Pekka Hannula, Finland
Michael Harris, USA
Yasuhiko Hayashi, Japan
F. Hernandez-Ramirez, Spain
Michael Z. Hu, USA
Nay Ming Huang, Malaysia
Shaoming Huang, China
Zafar Iqbal, USA
Balachandran Jeyadevan, Japan
Xin Jiang, Germany
Rakesh Joshi, Australia
Jeong-won Kang, Republic of Korea
Hassan Karimi-Maleh, Iran
Antonios Kelarakis, UK
Alireza Khataee, Iran
Ali Khorsand Zak, Iran
Philippe Knauth, France
Ralph Krupke, Germany
Christian Kübel, Germany
Prashant Kumar, UK
Eric Le Bourhis, France
Jun Li, Singapore
Meiyong Liao, Japan
Shijun Liao, China
Silvia Licocchia, Italy
Wei Lin, USA
Nathan C. Lindquist, USA
Zainovia Lockman, Malaysia
Nico Lovergine, Italy
Jim Low, Australia
- Jue Lu, USA
Ed Ma, USA
Laura M. Maestro, Spain
Gaurav Mago, USA
Muhamamd A. Malik, UK
Devanesan Mangalaraj, India
Sanjay R. Mathur, Germany
Tony McNally, UK
Yogendra Mishra, Germany
Paulo Cesar Morais, Brazil
Paul Munroe, Australia
Jae-Min Myoung, Republic of Korea
Rajesh R. Naik, USA
Albert Nasibulin, Russia
Toshiaki Natsuki, Japan
Koichi Niihara, Japan
Natalia Noginova, USA
Sherine Obare, USA
Won-Chun Oh, Republic of Korea
Atsuto Okamoto, Japan
Abdelwahab Omri, Canada
U. Paik, Republic of Korea
Piersandro Pallavicini, Italy
Edward A. Payzant, USA
Alessandro Pegoretti, Italy
Ton Peijs, UK
O. Perales-Pérez, Puerto Rico
Jorge Pérez-Juste, Spain
Alexey P. Popov, Finland
Philip D. Rack, USA
Peter Reiss, France
Orlando Rojas, USA
Marco Rossi, Italy
Ilker S. Bayer, Italy
Cengiz S. Ozkan, USA
Sudipta Seal, USA
Shu Seki, Japan
V. Šepelák, Germany
Huaiyu Shao, Japan
Prashant Sharma, USA
Donglu Shi, USA
Bhanu P. Singh, India
Surinder Singh, USA
Vladimir Sivakov, Germany
Ashok Sood, USA



Adolfo Speghini, Italy
Marinella Striccoli, Italy
Xuping Sun, KSA
Ashok K. Sundramoorthy, USA
Angelo Taglietti, Italy
Bo Tan, Canada
Leander Tapfer, Italy
Valeri P. Tolstoy, Russia
Muhammet S. Toprak, Sweden
R. Torrecillas, Spain
Achim Trampert, Germany

Takuya Tsuzuki, Australia
Tamer Uyar, Turkey
Bala Vaidhyanathan, UK
Luca Valentini, Italy
Rajender S. Varma, USA
Ester Vazquez, Spain
Ajayan Vinu, Australia
Ruibing Wang, Macau
Shiren Wang, USA
Yong Wang, USA
Magnus Willander, Sweden

Ping Xiao, UK
Zhi Li Xiao, USA
Yangchuan Xing, USA
Doron Yadlovker, Israel
Yoke K. Yap, USA
Kui Yu, Canada
William Yu, USA
Michele Zappalorto, Italy
Renyun Zhang, Sweden

Contents

Nanoscale Biological Materials

Kilho Eom, Serdal Kirmizialtin, Yaling Liu, and Zhiping Xu
Volume 2016, Article ID 5403560, 2 pages

Optimal Synthesis of Horizontally Aligned Single-Walled Carbon Nanotubes and Their Biofunctionalization for Biosensing Applications

Dawoon Jung, Hyun Woo Park, Gidong Ma, Chang Young Lee, Taeyun Kwon, and Jae-Hee Han
Volume 2016, Article ID 5140241, 8 pages

Nanomechanical Characterization of Amyloid Fibrils Using Single-Molecule Experiments and Computational Simulations

Bumjoon Choi, Taehee Kim, Sang Woo Lee, and Kilho Eom
Volume 2016, Article ID 5873695, 16 pages

Lipid Reconstitution-Enabled Formation of Gold Nanoparticle Clusters for Mimetic Cellular Membrane

Jiyoung Nam, Yong-Tae Kim, Aeyeon Kang, Kook-Han Kim, KyoRee Lee,
Wan Soo Yun, and Yong Ho Kim
Volume 2016, Article ID 2860859, 7 pages

Effects of End-Terminal Capping on Transthyretin (105–115) Amyloid Protofibrils Using Steered Molecular Dynamics

Myeongsang Lee, Hyunsung Choi, and Sungsoo Na
Volume 2016, Article ID 1863065, 10 pages

Sensitivity Analysis for the Mechanical Properties of DNA Bundles

Young-Joo Kim and Do-Nyun Kim
Volume 2016, Article ID 6287937, 7 pages

Emerging Utilization of Chrysin Using Nanoscale Modification

Joohee Jung
Volume 2016, Article ID 2894089, 7 pages

Development of a Time-Dependent Friction Model for Frictional Aging at the Nanoscale

Seung Yub Baek and Kyungmok Kim
Volume 2016, Article ID 7908345, 6 pages

Editorial

Nanoscale Biological Materials

Kilho Eom,¹ Serdal Kirmizialtin,² Yaling Liu,³ and Zhiping Xu⁴

¹*Biomechanics Laboratory, College of Sport Science, Sungkyunkwan University (SKKU), Suwon 16419, Republic of Korea*

²*Chemistry Program, New York University Abu Dhabi, Abu Dhabi, UAE*

³*Department of Mechanical Engineering and Mechanics, Lehigh University, Bethlehem, PA 18015, USA*

⁴*Department of Engineering Mechanics, Tsinghua University, Beijing 100084, China*

Correspondence should be addressed to Kilho Eom; kilhoeom@skku.edu

Received 27 July 2016; Accepted 27 July 2016

Copyright © 2016 Kilho Eom et al. This is an open access article distributed under the Creative Commons Attribution License, which permits unrestricted use, distribution, and reproduction in any medium, provided the original work is properly cited.

Biological materials at nanoscale such as proteins, antibodies, lipids, and nucleic acids have been highlighted not only for their important roles in life sciences but also for their wide range of applications in engineering and materials science. Understanding the design principles of biomaterials allows for gaining great insight into the creation and control of novel materials with interesting functional properties. Therefore it is of great importance to characterize the biomaterials' microstructures, self-assembly mechanism, and dynamics in high spatial and temporal resolution. During the last two decades, with technological advances in experimental instrumentation and methodology (e.g., single-molecule experiments) and advances in hardware and software that lead to more realistic computer simulations (e.g., atomistic, coarse-grained, and continuum simulations), the structures, properties, functions, and dynamics of nanoscale biological materials have been extensively studied. For instance, single-molecule experiments and atomistic simulations have revealed the underlying mechanisms of protein folding, protein dynamics, protein aggregation, RNA/DNA unzipping, and interactions between nanoscale biological materials (e.g., protein) with other chemical compounds (e.g., drug molecule). Understanding of these fundamental processes at atomic scale has driven multiple applications in biomedical engineering such as developing functional biomaterials with rational design.

With the advancements in the area of nanoscale biological materials as described above, this special issue is aimed towards presenting the current state-of-the-art approaches

in understanding the structures and dynamics of biological materials as well as their relationship with materials properties and hence the functions of the nanoscale biological materials including, but not limited to, DNA, RNA, protein, lipid, and self-assembled structures formed from these building blocks. This special issue covers different aspect of characterization of nanoscale biological materials from both computational and experimental viewpoints.

As a first example of these nanoscale biological materials, amyloid fibrils are discussed in this issue. Amyloid fibrils are a hallmark of neurodegenerative diseases, yet they have received great attention due to their remarkable structural stability. The mechanical strength of fibrils is comparable to that of mechanically strong protein materials such as spider silk. In the review paper entitled "Nanomechanical Characterization of Amyloid Fibrils Using Single-Molecule Experiments and Computational Simulations," B. Choi et al. described the recent efforts to characterize the mechanical properties of amyloid fibrils using single-molecule experiments (e.g., atomic force microscopy-based experiments) and computer simulations (e.g., atomistic and coarse-grained simulations). As described in the review paper, experimental and computer simulation approaches provide an estimate of elastic modulus for amyloid fibrils to be in the order of 1 to 10 GPa, which is comparable to the elastic modulus of a spider silk protein that is renowned as a mechanically strong protein material. M. Lee et al., in their paper "Effects of End-Terminal Capping on Transthyretin (105–115) Amyloid Protofibrils Using Steered Molecular Dynamics,"

explored the stability and mechanical properties of amyloid fibrils made of transthyretin (TTR). Using steered molecular dynamics simulations they provide great insight into the underlying mechanisms of the end-terminal capping effect on the fibril stability and the mechanical response of TTR amyloid fibrils. While deoxyribonucleic acid (DNA) is an important biomolecule that performs physiological functions such as delivering the genetic information, it has recently been considered as a building block for developing novel large-scale functional structures such as DNA origami. The mechanical properties (e.g., flexibility) of individual DNA molecules are known to play key role in the process of forming DNA origami structures. In a paper entitled "Sensitivity Analysis for the Mechanical Properties of DNA Bundles," Y.-J. Kim and D.-N. Kim studied the role of the mechanical properties of DNA bundles in forming the three-dimensional structural motifs such as DNA junctions and strand breaks by performing sensitivity analysis on a six-helix DNA bundle structure using finite element modeling approaches.

Functionalization of nanomaterials with biological molecules has played a vital role in developing a nanobiointerface platform, which can be used in many ways such as for biosensing or drug delivery. J. Nam et al., in their paper entitled "Lipid Reconstitution-Enabled Formation of Gold Nanoparticle Clusters for Mimetic Cellular Membrane," delineated the formation of gold nanoparticle clusters encapsulated with reconstituted phospholipid bilayers for facilitating cellular uptake, a process necessary for nanomaterial-based drug delivery. J. Jung, in her review paper entitled "Emerging Utilization of Chrysin Using Nanoscale Modification," discussed the current state-of-the-art approaches in nanoencapsulation and conjugation for overcoming the utilization of chrysin in pharmaceutical applications. In a paper, entitled "Optimal Synthesis of Horizontally Aligned Single-Walled Carbon Nanotubes and Their Biofunctionalization for Biosensing Applications," D. Jung et al. discussed how carbon nanotubes can be used to capture disease-related biomolecules in high sensitivity. They presented the detailed optimal synthesis conditions for such horizontally aligned carbon nanotube arrays functionalized with chemical molecules for biosensing and optical applications. Moreover, nanoscale friction and adhesion are one of the most important physical parameters in designing a nanobiointerface system and a challenging phenomenon to explain using physical principles. S. Y. Baek and K. Kim, in their paper entitled "Development of a Time-Dependent Friction Model for Frictional Aging at the Nanoscale," presented the theoretical model of nanoscale frictional aging based on a cohesive zone model. Their model was validated using numerical simulations and was used successfully to interpret the recent experimental data.

The guest editors hope that this special issue can inspire the readers and stimulate further research in the area of nanoscale biological materials, in particular, the characterization of the relationship between their structures, properties, and functions. These studies will doubtlessly lead to the exploration of novel applications in engineering and materials science while they further elucidate the physical principles behind the properties of biomaterials at nanoscale.

Acknowledgments

The editors are grateful to the authors for their contributions to this special issue and the anonymous reviewers for their fruitful discussions and comments.

*Kilho Eom
Serdal Kirmizialtin
Yaling Liu
Zhiping Xu*

Research Article

Optimal Synthesis of Horizontally Aligned Single-Walled Carbon Nanotubes and Their Biofunctionalization for Biosensing Applications

Dawoon Jung,¹ Hyun Woo Park,¹ Gidong Ma,¹ Chang Young Lee,²
Taeyun Kwon,³ and Jae-Hee Han¹

¹Department of Energy IT, Gachon University, Seongnam 13120, Republic of Korea

²School of Energy and Chemical Engineering, Ulsan National Institute of Science and Technology (UNIST), Ulsan 44919, Republic of Korea

³SKKU Advanced Institute of Nano Technology, Sungkyunkwan University (SKKU), Suwon 16419, Republic of Korea

Correspondence should be addressed to Taeyun Kwon; taeyunkwon@gmail.com and Jae-Hee Han; jhhan388@gachon.ac.kr

Received 17 February 2016; Accepted 30 May 2016

Academic Editor: Serdal Kirmizialtin

Copyright © 2016 Dawoon Jung et al. This is an open access article distributed under the Creative Commons Attribution License, which permits unrestricted use, distribution, and reproduction in any medium, provided the original work is properly cited.

As an influential candidate for highly sensitive biomolecule sensor, which can capture disease related biomolecules, carbon nanotube is useful material due to its unique properties. To adopt as a sensing platform, it is strongly needed to find optimal refined synthetic condition. In order to find the optimal synthetic conditions of horizontally aligned CNT, we performed quantity control of the mixed gases of H₂ and CH₄ injected. We successfully find that the formation of amorphous-like carbon was critically affected by some gas condition such as the flow rate of injected gases and ratios of gas mixture. Moreover, it should be noted that our horizontally aligned carbon nanotube array platform developed would offer another potential in developing nanoscale light source, where light emission results from electron-hole carrier recombination.

1. Introduction

In the past decades, it has been attractive to the community to develop the novel bioassay toolkits, which allow the fast, reliable, label-free, and highly sensitive detection of specific biological species, eventually resulting in early diagnosis of diseases such as cancer [1–4]. To the best of our knowledge, the detection sensitivity of conventional toolkits, such as DNA microarray, based on fluorescence imaging is not as good as that required for early cancer diagnosis due to the relatively large sensing surface and ineffectiveness of fluorescence, for example, low durability, and fluorescence quenching [5–7].

Scanning probe microscopy- (SPM-) based detection methods have recently served as a sensing toolkit that is able to sensitively identify the specific target biomolecules owing to the high spatial resolution of AFM (being even up to nanometer scale) [8–13]. For instance, tapping mode Atomic Force Microscopy (tmAFM) and Kelvin probe force

microscopy (KPFM) have enabled the sensitive detection of biomolecules such as DNA, RNA, and proteins [8, 13]. In addition, SPM does not require the cumbersome processing of samples such as the labeling of fluorescence dyes to target biomolecules, which implies that the fabrication of the sensing substrate is cost-effective and straightforward.

In addition to using SPM as an imaging toolkit, the preparation of nanoscale pattern is necessary in order for SPM-based sensing to achieve the high detection sensitivity. One of ways to prepare the nanoscale pattern is to consider carbon nanotube (CNT), which is useful material due to its unique properties. Specifically, it is easy to chemically modify the surface of CNT, particularly chemically attaching biological probes (e.g., aptamer, DNA, and RNA) to CNT surface. This easiness of the biological functionalization of CNT surface leads to the preparation of carbon nanotube-patterned surface that is able to specifically and selectively capture target biomolecules. In addition, as the diameter of

CNT is in the order of 1 to at most 10 nm, the very minute amount of target biomolecules can be specifically captured to the small area of CNT-patterned surface, which indicates the high detection sensitivity of CNT-patterned surface.

Based on aforementioned CNT-patterned surface along with SPM imaging technique, we have shown that a horizontally aligned carbon nanotube- (HACNT-) patterned surface enables the specific detection of biomolecules with ultra-sensitivity for early cancer diagnostics [14, 15]. In particular, it is shown that HACNT-patterned surface-based detection system is able to sense specific target biomolecules such as proteins (e.g., thrombin) and tumor marker. The detection limit of our detection system based on SPM imaging and HACNT-patterned surface is as low as single-molecule level, which is much better than the detection limit of other conventional bioassay toolkits.

For sensitive detection based on aforementioned CNT-patterned surface, it is important to prepare the optimally patterned CNTs on the surface. In our previous works, the optimal patterning of CNTs on the surface has not been fully studied yet. For instance, when CNT pattern is not optimally designed, it is likely that amorphous carbon can undesirably be formed when CNT is chemically grown; this amorphous carbon may prevent the CNT-patterned surface from exhibiting the high detection sensitivity. In this work, we provide the optimal fabrication condition that allows us to prepare the well-designed CNT-patterned surface, which can serve as a biosensing platform. Moreover, we describe the optimal condition for chemical functionalization of CNTs patterned on the surface for specific and selective detection. In particular, we delineate the functionalization of CNTs with rhodamine dyes. The surface patterned with CNTs functionalized with rhodamine can act as a nanoscale optical device that may respond to the environmental change [16, 17].

2. Experimental Methods

2.1. Carbon Nanotube Synthesis and Functionalization. In order to synthesize the HACNT array, a thermal chemical vapor deposition (CVD) system (SciEnTech Co., Ltd.) was employed. In our previous work, the mechanism and details of thermal CVD system to grow the array are well described [14, 15, 18]. In brief, the thermal CVD system we used in this work consists of hydrocarbon feedstock gas (methane, CH₄, 99.9%) as atomic carbon source for the nanotube growth, both hydrogen (H₂, 99.999%) and argon (Ar, 99.999%) as catalytic carrier gases, and a SiO₂/Si substrate with iron (Fe) catalyst layer. The growth time was fixed to 3 hours; the growth temperature varied between 1000 and 1100°C at atmospheric pressure. To functionalize the synthesized HACNT array with 4-aminophenyl-diazonium tetrafluoroborate salt (NH₂-diazonium), the array was dipped into a solution of NH₂-diazonium with a small amount of NaOH for catalyst for this chemical reaction with stirring at 50°C for 1 hour. After the NH₂-diazonium functionalization, the array was redipped into a solution of rhodamine-b-isothiocyanate (RITC) dyes with stirring at room temperature for 10 hours. The morphology of the HACNT array after synthesis and a

subsequent functionalization was characterized using scanning electron microscopy (SEM, Hitachi S-4700).

2.2. Atomic Force Microscopy Imaging. All images of CNT were acquired using a tapping mode at the scanned location. The SPM-based measurement was performed using Innova (Veeco Inc., Santa Barbara, CA, USA) with Nanocontroller V (Veeco Inc.) under an ambient condition at room temperature. To obtain images, we have utilized TESP-V2 tip (Veeco Inc.) as a scanning probe. Here, TESP-V2 tip has the normal resonant frequency of 320 kHz and tip radius of ~8 nm. The tapping mode AFM (tmAFM) images were acquired based on scanning speed of 1 μm/s, which is suitable to guarantee the high-quality images. We obtained the tmAFM images for the scan size of 2 μm × 2 μm, which is a proper scan size to image a couple of CNTs on the substrate. All SPM images were generated from Nanoscope software V7.2.

2.3. Raman Spectroscopy. The degree of the functionalization of the HACNT array with NH₂-diazonium and RITC was characterized using Raman spectroscopy (WITec, Alpha 300 M+, 532 nm laser excitation, and 300 nm spatial resolution). In particular, Raman spectra of the sample were obtained after the sample was fully dried at room temperature. Raman mapping was carried out with a spectral area of 10 × 10 μm² using a customized built-in software, where points per line and scan speed were 100 and 13 seconds/line, respectively.

3. Results and Discussion

Figure 1(a) shows a schematic illustration of a horizontally aligned carbon nanotube (HACNT) array on a SiO₂/Si substrate grown by chemical vapor deposition (CVD) method. In the case of HACNT array growth, individual carbon nanotubes are generally known to get nucleated from catalyst metals prepatterned at the one end of the substrate and then subsequently extend their length with a process time through the *kite mechanism* by which carbon nanotubes being grown are floating above the underlying substrate in the same direction with feedstock gas flow injected into a reactor during synthesis [19]. Figure 1(b) depicts a schematic diagram representing a process of surface functionalization of individual carbon nanotubes of the HACNT array with NH₂-diazonium after the array synthesis and then subsequent RITC functionalization. The amine groups functionalized on the outer surface of carbon nanotubes are generally expected to act as an electron donor to give electrons towards the nanotube because of their relatively high reduction potential over the valence band of the semiconducting single-walled carbon nanotubes [20, 21]. In addition, the NH₂-diazonium functionalization on the nanotubes would allow mediation of a further functionalization of RITC on the NH₂-diazonium functionalized nanotube assembly by replacing NH₂-group with RITC, which exhibits fluorescence in the visible light wavelength regime [22].

Scanning electron microscopic (SEM) images of the HACNT arrays are shown in Figure 2, where the effect of total flow rate of feedstock gases during the synthesis on the

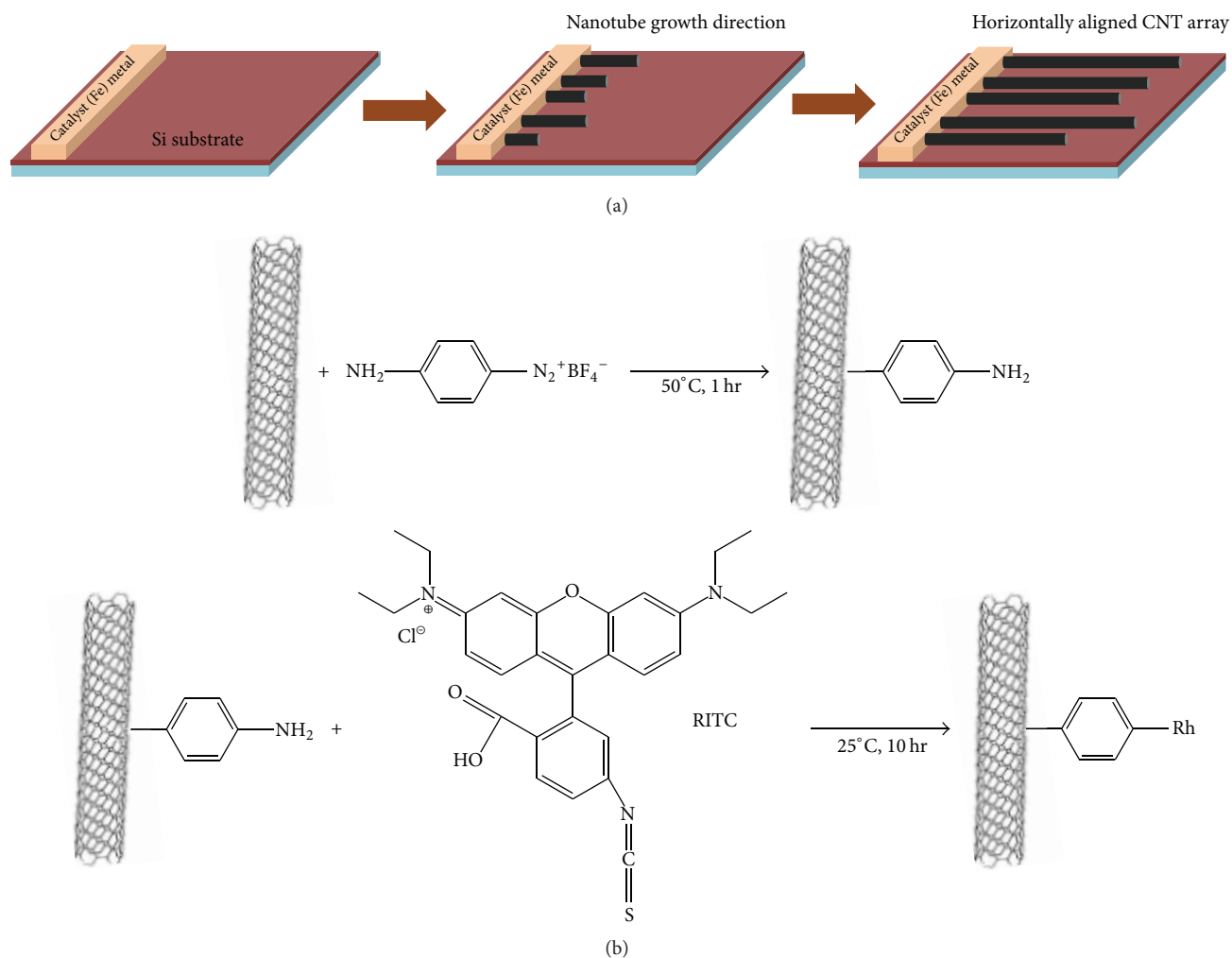


FIGURE 1: Schematic illustrations of (a) fabrication of a horizontally aligned carbon nanotube (HACNT) array by chemical vapor deposition (CVD) method on a Si substrate and (b) subsequent functionalization of HACNT with NH_2 -diazonium, followed by rhodamine dye moieties.

growth morphology and density of the arrays is provided when a relative flow rate ratio of hydrogen (H_2) and methane (CH_4) gas was kept constant as two. In each subset of the Figure 2, the left (or right) image shows the appearance of the nanotubes in the array grown near (or far away from) the Fe catalyst metal in the nanotube growth region, which is indicated by a red arrow in an upper-left panel of the Figure 2. As total flow rate of the feedstock gases was increased from 4.5 to 9.0 standard cubic centimeter (SCCM), the growth density of each sample was found to be different although the morphologies seemed to be similar (Figures 2(a)–2(d)). Interestingly, when the total flow rate was 9 SCCM (Figure 2(d)), it was hard to find the initial nucleation of the nanotubes allowing their substantial growth afterwards. This result would be possibly because the hydrogen atoms could either etch away the carbon atoms, which are thermally dissociated from CH_4 feedstock gas, or replace the dangling bonds of the carbon atoms prior to forming a normal nanotube structure [23]. It is expected that there would be a certain total flow rate that corresponds to the optimal quantity making the nanotubes initiate their growth even if a relative

flow rate ratio of the feedstock gases was maintained to be constant. Otherwise, the growth of the HACNT array would be deactivated (Figure 2(d)).

To determine the effect of the relative flow rate ratio of H_2 and CH_4 compared to the result shown in Figure 2, where the flow ratio is two, the flow ratio using the same gases was slightly decreased to one and a half (Figure 3). Then, as similarly shown in Figure 2, we have systematically increased the total flow rate of the feedstock gases from 3.75 to 7.5 SCCM (Figures 3(a)–3(c)). In this case, the flow rate of H_2 gas injected was reduced by 75% at a given flow rate of CH_4 gas as compared with that in Figure 2. As the total flow rate was increased (Figures 3(a)–3(c)), the morphology and density of the HACNT arrays were markedly changed as compared with the result shown in Figure 2. More specifically, when the total flow rate was increased from 3.75 SCCM (Figure 3(a)) to 6.25 SCCM (Figure 3(b)) by a factor of ~ 1.7 , it was observed that the surface of the carbon nanotubes in the array grown was covered by a large amount of the amorphous-like carbon. This morphological appearance is quite obviously compared with that shown in Figure 2,

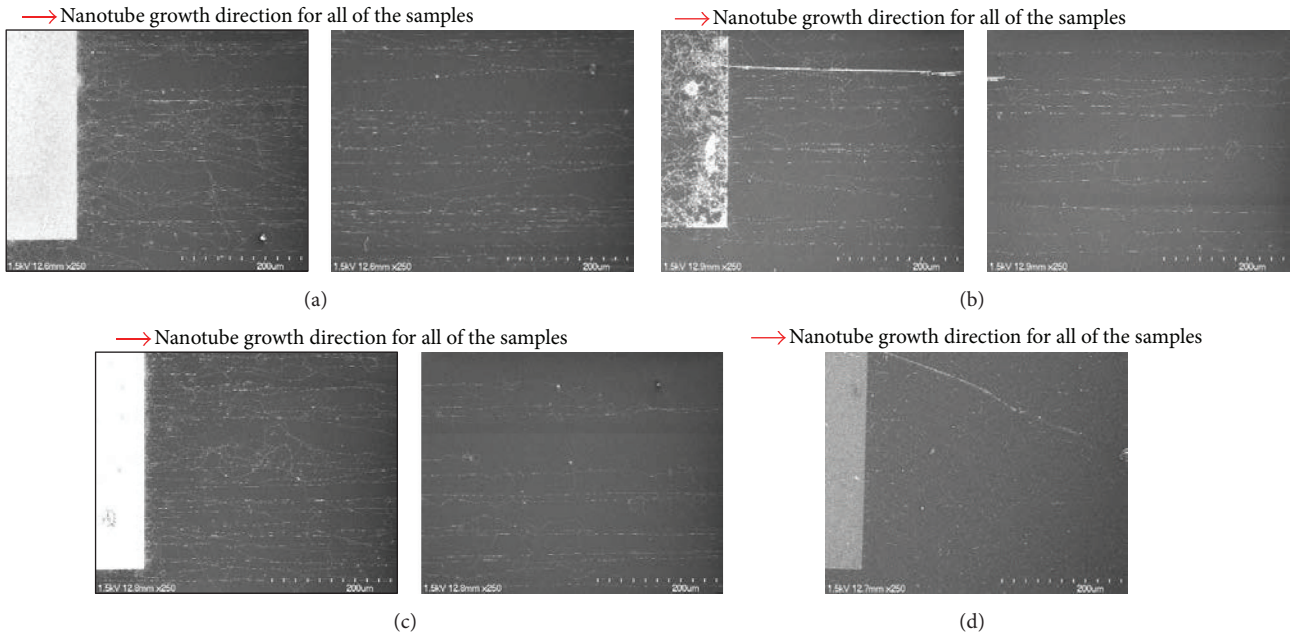


FIGURE 2: Scanning electron microscopy (SEM) images representing an effect of total flow rate (in unit of standard cubic centimeter (SCCM)) of feedstock gases while maintaining a relative flow rate ratio of H_2 and CH_4 , which is two, during HACNT arrays growth on their morphologies and densities. Total flow rate varies at (a) 4.5, (b) 6.0, (c) 7.5, and (d) 9.0, respectively. Note that no tubes were nearly grown at the total flow rate of 9.0. Left (or right) image of each subfigure set corresponds to a regime of the array grown near (or far from) Fe catalyst in the growth direction.

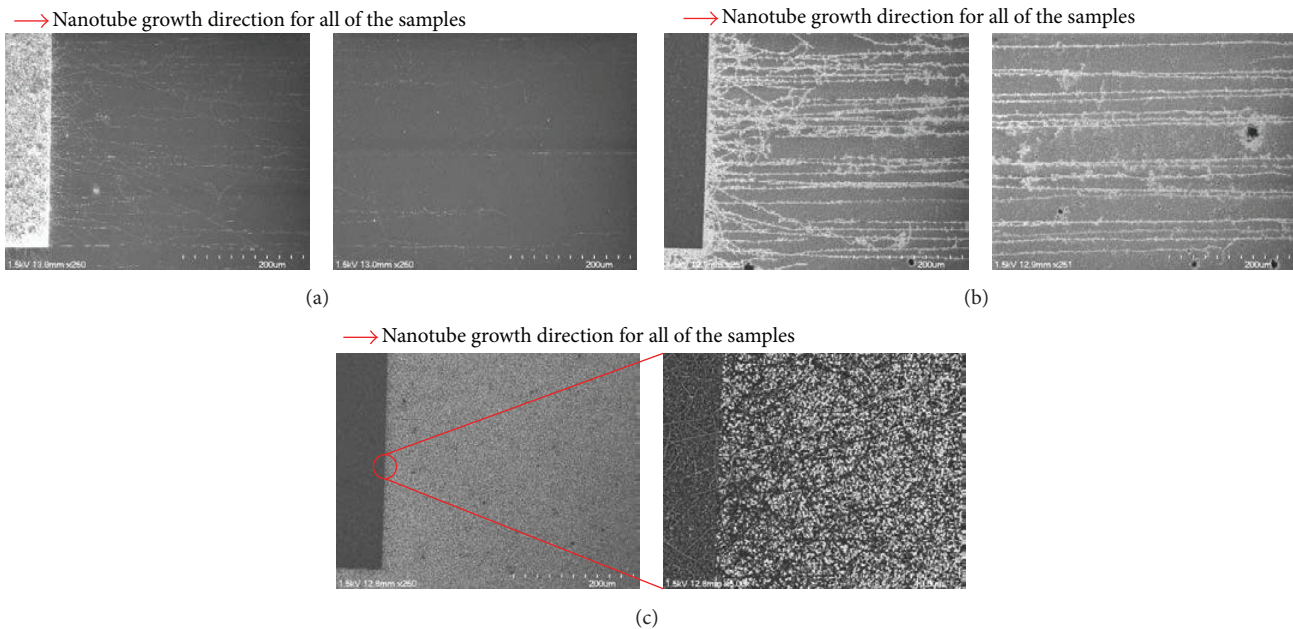


FIGURE 3: SEM images indicating an effect of a different relative flow rate of H_2 and CH_4 gases, which is one and a half, compared to the results of Figure 2, on the morphologies and densities of HACNT arrays grown with the total flow rates of (a) 3.75, (b) 6.25, and (c) 7.5, respectively. Note that few tubes were grown and covered with amorphous-like carbon debris at the total flow rate of 7.5.

where the same amount of the total flow rate was increased (Figures 2(a) and 2(c)). Moreover, when the total flow rate was increased to 7.5 SCCM, which equals an increase by a factor of 2 compared to that shown in Figure 3(a), the HACNT array was found to be rarely grown, and most of the substrate

seemed to be coated with thick layers of the amorphous-like carbon. In brief, with the results of Figures 2 and 3 mentioned above, the mechanism of patterned carbon nanotube growth can be described as follows: if the relative flow rate ratio of H_2 and CH_4 is decreased by a certain percentage (despite the

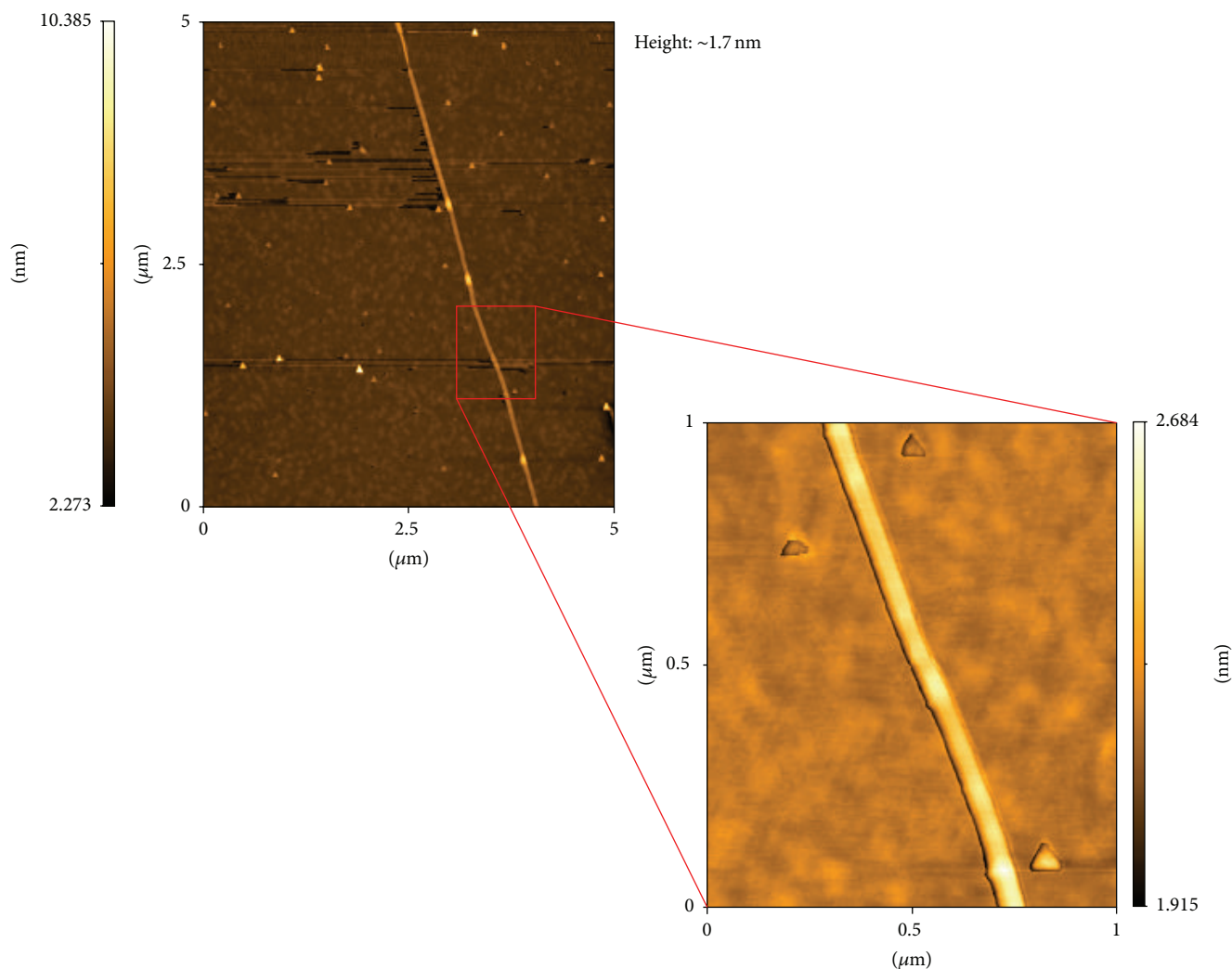


FIGURE 4: Atomic force microscopy (AFM) images of a representative HACNT array.

total flow rates of feedstock gases injected into a reactor being the same), the carbon atoms produced from CH_4 gas would not be able to properly form a lattice structure of the carbon nanotube due to decrease in numbers of the hydrogen atoms created from H_2 gas, which are supposed to act as *scavengers* for the carbon atoms in the gas phase reaction [24].

Figure 4 shows AFM images of the HACNT-patterned surface. As shown in Figure 4, the diameter of CNT horizontally grown on the surface is found to be ~ 1.7 nm. Here, we note that CNT horizontally grown on the surface was fabricated based on the optimal synthesis condition as described above.

Figure 5 depicts the results of 1-dimensional (1D) spectra and 2-dimensional (2D) mapping images from Raman spectroscopy on the samples that were prepared as schematically shown in Figure 1(b). Specifically, the Raman images were shown for a pristine CNT (Figures 5(a)–5(c)), CNT functionalized with NH_2 -diazonium (Figures 5(d)–5(f)), and CNT chemically modified with RITC molecules (Figures 5(g)–5(i)), respectively. In Raman spectroscopy, the G-band corresponds to planar vibrations of carbon atoms and is present

in most graphite-like materials. The D-band is present in all graphite-like carbons and originates from structural defects. The radial breathing mode (RBM) corresponds to radial expansion-contraction of the nanotube. And the G' -band arises from a two-phonon, intervalley, second-order Raman scattering process [25, 26]. From these images, we have the following observations: first, when the carbon nanotubes in the HACNT array were functionalized with NH_2 -diazonium, the overall G-band intensities decreased over the whole spectral regime investigated, compared to the bare ones (Figures 5(a) and 5(d)). However, the number density of bright spots in the D-band images (Figures 5(b) and 5(e)) increased, which would probably correspond to the region with NH_2 -diazonium functionalization. These results indicate that the NH_2 -diazonium functionalization would create the defect sites on the surface of carbon nanotubes. Overall, both the G-band and D-band images (Figures 5(g) and 5(h)) of the carbon nanotubes functionalized with NH_2 -diazonium and a subsequent RITC molecules show lower spectral intensities compared to those mentioned above. A possible reason for this would be a large amount of loss of the carbon

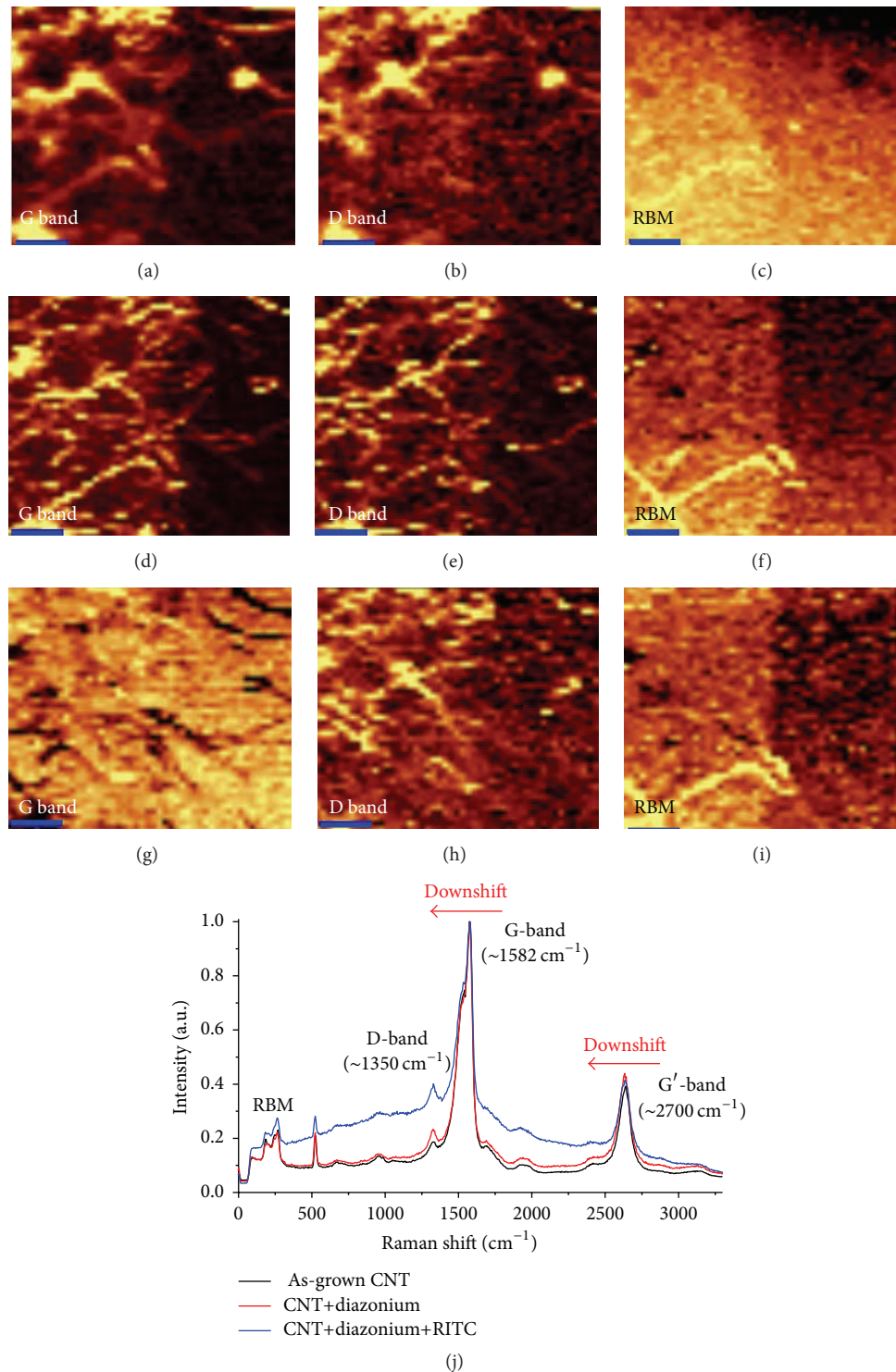


FIGURE 5: 2D Raman mapping images recorded at ((a), (b), (c)) intact individual carbon nanotubes in the HACNT array, ((d), (e), (f)) the same tubes functionalized with NH_2 -diazonium, and ((g), (h), (i)) the same tubes functionalized with NH_2 -diazonium/rhodamine dye in sequence. All scale bars represent $2\ \mu\text{m}$. (j) Three Raman spectra for each sample are depicted, indicating radial breathing mode (RBM), D-band, G-band, and G'-band.

nanotubes during the RITC functionalization. But it is still observed that the D-band intensities in some of the regions (Figure 5(h)) became brighter than in those shown in Figure 5(e), revealing the higher degree of the functionalization. The NH_2 -diazonium and a subsequent functionalization of RITC molecules on the carbon nanotubes seem to produce the RBM images with little difference. Figure 5(j) depicts the representative three 1D Raman spectra of each sample discussed above. Interestingly, it was observed that the D-/G-band intensity ratio increased, and the G' -band position downshifted ($\sim 15\text{--}20\text{ cm}^{-1}$) with both NH_2 -diazonium and RITC functionalization (the resolution of the system was $\sim 1\text{ cm}^{-1}$). It should be noted here that the functionalization of CNT surface with NH_2 -diazonium would probably act as a defect site onto a SWNT surface, which makes the D-/G-band intensity ratio increase in the Raman spectra. Furthermore, the reason for both G-band and G' -band can be attributed to the fact that NH_2 -diazonium functionalization would donate electrons into carbon atom (n-doped) in a SWNT; therefore the carbon-carbon (C-C) bond at the edge of a SWNT would become extended which would directly cause the Raman softening (i.e., Raman downshift) [20, 27].

4. Conclusion

In this work, we have determined optimal synthetic conditions of the CNT horizontally aligned on the surface with quantity control of the mixed gases of H_2 and CH_4 injected. It was revealed that the formation of amorphous-like carbon was critically affected by gas condition such as the flow rate of injected gases and ratios of gas mixture. It is expected that the optimal synthetic conditions studied in this work enable us to prepare the high-quality CNT-patterned surface, which may be employed for selective and sensitive biosensing applications. In addition, it should be noted that the HACNT array platform developed in this work would offer another potential in developing nanoscale light source, where light emission results from electron-hole carrier recombination. This property should enable electroluminescence (EL) in the array, which can detect subtle changes from the environments (i.e., biological and chemical). This implies that CNT-patterned surface described in this work can be considered for establishing a nanoscale optical device. Our study may provide insight into optimization of the synthesis of the HANCT array, which enables not only highly sensitive detection platforms for sensing diseases-related biomolecules, but also a new type of nanoscale light source that are able to detect environmental changes. Future work will be directed towards further development of HACNT-based biosensing platform, which may allow for diagnosis of fatal diseases such as cancer.

Competing Interests

The authors declare that they have no competing interests.

Authors' Contributions

Dawoon Jung and Hyun Woo Park contributed equally to this work.

Acknowledgments

Jae-Hee Han appreciates the financial support from Civil-Military Technology Cooperation Program (Grant no. 14-CM-EB-08), Agency for Defense Development through Chemical and Biological Defense Research Center, and National Research Foundation of Korea (NRF) under Grant no. 2012R1A1A1015734. Chang Young Lee acknowledges the financial support from NRF under Grant no. 2013R1A1A2073264. Taeyun Kwon appreciates the financial support from the National Research Foundation of Korea (NRF) under Grant no. 2015R1A2A1A15052758.

References

- [1] K. Eom, H. S. Park, D. S. Yoon, and T. Kwon, "Nanomechanical resonators and their applications in biological/chemical detection: nanomechanics principles," *Physics Reports*, vol. 503, no. 4-5, pp. 115-163, 2011.
- [2] J.-S. Park, M. K. Cho, E. J. Lee et al., "A highly sensitive and selective diagnostic assay based on virus nanoparticles," *Nature Nanotechnology*, vol. 4, pp. 259-264, 2009.
- [3] S. Wang, H. Wang, J. Jiao et al., "Three-dimensional nanostructured substrates toward efficient capture of circulating tumor cells," *Angewandte Chemie—International Edition*, vol. 48, no. 47, pp. 8970-8973, 2009.
- [4] G. Lee, K. Eom, J. Park et al., "Real-time quantitative monitoring of specific peptide cleavage by a proteinase for cancer diagnosis," *Angewandte Chemie International Edition*, vol. 51, no. 24, pp. 5837-5841, 2012.
- [5] S. P. Fodor, R. P. Rava, X. C. Huang, A. C. Pease, C. P. Holmes, and C. L. Adams, "Multiplexed biochemical assays with biological chips," *Nature*, vol. 364, no. 6437, pp. 555-556, 1993.
- [6] M. Schena, D. Shalon, R. W. Davis, and P. O. Brown, "Quantitative monitoring of gene expression patterns with a complementary DNA microarray," *Science*, vol. 270, no. 5235, pp. 467-470, 1995.
- [7] D. Liu, A. Bruckbauer, C. Abell et al., "A reversible pH-driven DNA nanoswitch array," *Journal of the American Chemical Society*, vol. 128, no. 6, pp. 2067-2071, 2006.
- [8] D. Zhou, K. Sinniah, C. Abell, and T. Rayment, "Label-free detection of DNA hybridization at the nanoscale: a highly sensitive and selective approach using atomic-force microscopy," *Angewandte Chemie—International Edition*, vol. 42, no. 40, pp. 4934-4937, 2003.
- [9] S. Husale, H. H. J. Persson, and O. Sahin, "DNA nanomechanics allows direct digital detection of complementary DNA and microRNA targets," *Nature*, vol. 462, no. 7276, pp. 1075-1078, 2009.
- [10] A. K. Sinensky and A. M. Belcher, "Label-free and high-resolution protein/DNA nanoarray analysis using Kelvin probe force microscopy," *Nature Nanotechnology*, vol. 2, no. 10, pp. 653-659, 2007.
- [11] C. Leung, H. Kinns, B. W. Hoogenboom, S. Howorka, and P. Mesquida, "Imaging surface charges of individual biomolecules," *Nano Letters*, vol. 9, no. 7, pp. 2769-2773, 2009.
- [12] O. K. Wong, M. Guthold, D. A. Erie, and J. Gelles, "Interconvertible lac repressor-DNA loops revealed by single-molecule experiments," *PLoS Biology*, vol. 6, no. 9, article e232, 2008.

- [13] J. Park, J. Yang, G. Lee et al., "Single-molecule recognition of biomolecular interaction via kelvin probe force microscopy," *ACS Nano*, vol. 5, no. 9, pp. 6981–6990, 2011.
- [14] K. Nam, K. Eom, J. Yang et al., "Aptamer-functionalized nanopattern based on carbon nanotube for sensitive, selective protein detection," *Journal of Materials Chemistry*, vol. 22, no. 44, pp. 23348–23356, 2012.
- [15] T. Kwon, J. Park, G. Lee et al., "Carbon nanotube-patterned surface-based recognition of carcinoembryonic antigens in tumor cells for cancer diagnosis," *The Journal of Physical Chemistry Letters*, vol. 4, no. 7, pp. 1126–1130, 2013.
- [16] P. Avouris, M. Freitag, and V. Perebeinos, "Carbon-nanotube photonics and optoelectronics," *Nature Photonics*, vol. 2, no. 6, pp. 341–350, 2008.
- [17] X. Xie, A. E. Islam, M. A. Wahab et al., "Electroluminescence in aligned arrays of single-wall carbon nanotubes with asymmetric contacts," *ACS Nano*, vol. 6, no. 9, pp. 7981–7988, 2012.
- [18] K. Eom, K. Nam, H. Jung et al., "Controllable viscoelastic behavior of vertically aligned carbon nanotube arrays," *Carbon*, vol. 65, pp. 305–314, 2013.
- [19] W. J. Hong, Y. X. Xu, G. W. Lu, C. Li, and G. Q. Shi, "Transparent graphene/PEDOT-PSS composite films as counter electrodes of dye-sensitized solar cells," *Electrochemistry Communications*, vol. 10, no. 10, pp. 1555–1558, 2008.
- [20] B. Das, R. Voggu, C. S. Rout, and C. N. R. Rao, "Changes in the electronic structure and properties of graphene induced by molecular charge-transfer," *Chemical Communications*, no. 41, pp. 5155–5157, 2008.
- [21] Y.-J. Do, J.-H. Lee, H. Choi et al., "Manipulating electron transfer between single-walled carbon nanotubes and diazonium salts for high purity separation by electronic type," *Chemistry of Materials*, vol. 24, no. 21, pp. 4146–4151, 2012.
- [22] M. F. Al-Kadhemy, I. F. Alsharuee, and A. A. D. Al-Zuky, "Analysis of the effect of the concentration of rhodamine B in ethanol on the fluorescence spectrum using the 'Gauss Mod' function," *Journal of Physical Science*, vol. 22, no. 2, pp. 77–86, 2011.
- [23] B. C. Liu, S. C. Lyua, T. J. Lee et al., "Synthesis of single- and double-walled carbon nanotubes by catalytic decomposition of methane," *Chemical Physics Letters*, vol. 373, no. 5-6, pp. 475–479, 2003.
- [24] J.-H. Han, C. H. Lee, D. Jung et al., "NH₃ effect on the growth of carbon nanotubes on glass substrate in plasma enhanced chemical vapor deposition," *Thin Solid Films*, vol. 409, no. 1, pp. 120–125, 2002.
- [25] P. C. Eklund, J. M. Holden, and R. A. Jishi, "Vibrational modes of carbon nanotubes; spectroscopy and theory," *Carbon*, vol. 33, no. 7, pp. 959–972, 1995.
- [26] M. S. Dresselhaus, G. Dresselhaus, R. Saito, and A. Jorio, "Raman spectroscopy of carbon nanotubes," *Physics Reports*, vol. 409, no. 2, pp. 47–99, 2005.
- [27] A. C. Ferrari, "Raman spectroscopy of graphene and graphite: disorder, electron-phonon coupling, doping and nonadiabatic effects," *Solid State Communications*, vol. 143, no. 1-2, pp. 47–57, 2007.

Review Article

Nanomechanical Characterization of Amyloid Fibrils Using Single-Molecule Experiments and Computational Simulations

Bumjoon Choi,¹ Taehee Kim,² Sang Woo Lee,¹ and Kilho Eom³

¹Department of Biomedical Engineering, Yonsei University, Wonju 26493, Republic of Korea

²College of Sport Science, Sungkyunkwan University (SKKU), Suwon 16419, Republic of Korea

³Biomechanics Laboratory, College of Sport Science, Sungkyunkwan University (SKKU), Suwon 16419, Republic of Korea

Correspondence should be addressed to Kilho Eom; kilhoeom@skku.edu

Received 11 February 2016; Revised 29 April 2016; Accepted 5 May 2016

Academic Editor: Silvia Licoccia

Copyright © 2016 Bumjoon Choi et al. This is an open access article distributed under the Creative Commons Attribution License, which permits unrestricted use, distribution, and reproduction in any medium, provided the original work is properly cited.

Amyloid fibrils have recently received much attention due to not only their important role in disease pathogenesis but also their excellent mechanical properties, which are comparable to those of mechanically strong protein materials such as spider silk. This indicates the necessity of understanding fundamental principles providing insight into how amyloid fibrils exhibit the excellent mechanical properties, which may allow for developing biomimetic materials whose material (e.g., mechanical) properties can be controlled. Here, we describe recent efforts to characterize the nanomechanical properties of amyloid fibrils using computational simulations (e.g., atomistic simulations) and single-molecule experiments (e.g., atomic force microscopy experiments). This paper summarizes theoretical models, which are useful in analyzing the mechanical properties of amyloid fibrils based on simulations and experiments, such as continuum elastic (beam) model, elastic network model, and polymer statistical model. In this paper, we suggest how the nanomechanical properties of amyloid fibrils can be characterized and determined using computational simulations and/or atomic force microscopy experiments coupled with the theoretical models.

1. Introduction

Amyloid fibrils, which are formed by self-assembly process (i.e., protein aggregation) [1–4], have recently received significant attention due to not only their important role in disease pathologies [5–9] but also their excellent nanomechanical properties [10]. In particular, amyloid materials have been found to be associated with various diseases such as neurodegenerative diseases [5–7] (e.g., Alzheimer's disease and Parkinson's disease), type II diabetes [8], and cardiovascular disease [11]. These amyloid materials exhibit multiscale structural feature [10] such that they are amyloid small aggregate (e.g., amyloid oligomer) at nanoscale, amyloid fibril at submicron scale, and amyloid plaques at micron scale. More remarkably, amyloid materials such as oligomers and fibrils are the ordered structures made of β -strands [1]. This ordered structure of amyloid materials is responsible for their insolubility in physiological condition and also for their remarkable (mechanical) properties. Specifically, β strand-rich protein structures (e.g., amyloid) are stable due

to hydrogen bonds that sustain (and stabilize) β -sheet-rich structures [12, 13]. In addition, recent experimental studies [14, 15] report that the mechanical properties of amyloid fibril are determined from the content of β -sheets comprising the fibril in such a way that as the β -sheet content increases the mechanical properties (e.g., elastic modulus) of the fibril are improved.

The nanomechanical properties of amyloid fibrils have recently been measured based on experimental and computational techniques. In particular, atomic force microscopy (AFM) or cryo-electron microscopy (EM) imaging techniques coupled with polymer chain statistics have allowed for estimating the bending property (i.e., persistent length) of amyloid fibrils [16, 17]. Specifically, the mechanical properties of protein fibrils are measured based on their fluctuation behavior, which can be obtained from AFM images or cryo-EM images. Recently, this imaging-based mechanical characterization has been implemented in FiberApp [18], which is an open software for analyzing the structures and mechanical

properties of protein fibrils based on AFM images. Moreover, AFM nanoindentation technique has enabled the mechanical characterization of amyloid fibrils [19–21]. In addition, computational simulations based on atomistic and/or elastic network models have been extensively employed for characterizing the nanomechanical properties of amyloid fibrils [10, 22–24]. Based on experimental and computational techniques, the elastic modulus of amyloid fibrils is measured in the order of 1 to 10 GPa [10, 22–24], which is comparable to that of a spider silk protein [25], which is known as one of the mechanically strong proteins. Moreover, the toughness of amyloid small aggregates with their size of ~ 3 nm is measured as ~ 30 kcal·mol⁻¹·nm⁻³ [23], which is very close to that of spider silk crystal with its size of ~ 2 nm. Recent experimental [26] and computational studies [22, 23] report an important role that the length scale of protein fibrils plays in their nanomechanical properties. This length scale effect in the nanomechanical properties of amyloid fibrils is attributed to the fact that the deformation mechanism of the fibrils depends on their length scale.

The remarkable mechanical properties of amyloid fibrils have recently been found to play a pivotal role in their biological functions such as disease pathologies [36]. For instance, it has recently been reported that the mechanical disruption of cell membrane due to amyloid fibril [37] is ascribed to the fact that the elastic modulus of amyloid fibrils is in the order of 1 to 10 GPa [10], whereas the elastic modulus of cell membrane is in the order of 100 kPa [38]. This observation suggests an evidence that the nanomechanical properties of amyloid fibrils are highly correlated with their biological functions. Moreover, a recent study by Tanaka and coworkers [39] reports that prion infectivity is determined from the fracture toughness (brittleness) of prion fibrils such that the softer the fibril, the higher the prion infectivity. In addition, as described in our recent study [30], the size-dependent elastic properties of HET-s prion fibrils provide insight into their critical size related to prion infectivity. These observations highlight a role that the nanomechanical properties of amyloid fibrils play in their pathological functions.

In this paper, we describe recent attempts to characterize the nanomechanical properties of amyloid fibrils by using experiments and simulations, as the mechanical characterization of the fibrils is of great importance for further understanding of their biological functions. This paper is organized as follows: Section 2 summarizes theoretical models such as elastic network model, elastic beam model, and polymer chain model, which can be coupled with experiments or computational simulations in order to measure the mechanical properties of amyloid fibrils. In Section 3, we provide the recent efforts to characterize the nanomechanical properties of amyloid fibrils with using single-molecule experiments based on atomic force microscopy (AFM). Section 4 is dedicated to the review of computational efforts to measure the mechanical properties of amyloid fibrils as well as gain insight into their deformation mechanisms. In Section 5, we conclude this paper with providing remarks and further directions that can be considered for future works.

2. Theoretical Models

In this section, we summarize theoretical models that are useful in analyzing the experimental and simulation results to extract the nanomechanical properties of amyloid fibrils. Here, we note that the principles of computational simulations such as atomistic simulation and normal mode analysis are not included in this review, but the principles of these simulations including steered molecular dynamics (SMD) simulations are well described in [40–44]. In addition, though we describe recent experimental attempts to characterize the mechanical properties of amyloid fibrils, we skip the details of AFM experimental methods (e.g., AFM imaging and indentation), which are well summarized in [45]. In the following, we provide theoretical models such as polymer chain model, elastic network model, and continuum elastic beam model.

2.1. Polymer Chain Model: Polymer Chain Statistics. Polymer chain models have allowed for understanding the fluctuation behavior of one-dimensional polymer molecules [46]. Among polymer chain models, a wormlike chain (WLC) model [47] has been widely accepted for analyzing the fluctuation behavior of a biological molecule [48, 49] such as DNA chain [50, 51] and protein fibril, for example, microtubule [52]. The WLC model assumes that a biological fibril is composed of rigid subchains. The energy (V) required to bend an angle (θ) between two subchains located a distance ξ apart is given by

$$V = \frac{E_B I}{2\xi} \theta^2, \quad (1)$$

where E_B and I are elastic modulus and cross-sectional moment of inertia for a biological fibril, respectively. A probability distribution function for an angle θ obeys Boltzmann's distribution such as

$$p(\theta) = \sqrt{\frac{E_B I}{2\xi k_B T}} \exp\left(-\frac{E_B I}{2\xi k_B T} \theta^2\right), \quad (2)$$

where k_B and T are Boltzmann's constant and absolute temperature, respectively. Here, it should be noted that the persistent length (L_p) of a biological fibril is defined as $L_p = E_B I / k_B T$. The ensemble averages for an angle θ and its cosine value are given by [49]

$$\langle \theta^2 \rangle = \frac{\xi}{L_p}, \quad (3)$$

$$\langle \cos \theta \rangle = \exp\left(-\frac{\xi}{2L_p}\right). \quad (4)$$

The mean-squared value of the end-to-end distance (R) of a biological fibril in a two-dimensional space (i.e., on the surface) is represented in the form of [51]

$$\frac{\langle R^2 \rangle}{L^2} = 4 \left(\frac{L}{L_p}\right) \left[1 - \frac{2L_p}{L} \left\{1 - \exp\left(-\frac{L}{2L_p}\right)\right\}\right], \quad (5)$$

where L is a contour length of a biological fibril.

2.2. Elastic Network Model. Coarse-grained (CG) model enables not only the computationally efficient dynamic analysis of protein molecules [41, 53–56] but also the insight into a role that the structure of protein molecules plays in their dynamics and mechanics. The computational efficacy of CG model is due to the modeling strategy in that minimal degrees of freedom are used to model a protein structure with simplified interaction potential field.

Among CG models, an elastic network model (ENM) [41, 57–64] is not only a most simple and computationally efficient model, but also a minimalist model which can provide an insight into the role of protein structure on the mechanics and dynamics of a protein molecule. The basic idea of ENM is to consider only the α -carbon atoms of a protein structure, while interaction between these α -carbon atoms is simplified as harmonic interaction. The potential field of ENM is given by

$$V = \frac{\gamma}{2} \sum_{i,j} \left(|\vec{r}_i - \vec{r}_j| - |\vec{r}_i^0 - \vec{r}_j^0| \right)^2 \cdot H(R_c - |\vec{r}_i^0 - \vec{r}_j^0|), \quad (6)$$

where γ is the force constant of a harmonic potential defined between two α -carbon atoms i and j , \vec{r}_i is the position vector of the i th α -carbon atom, superscript 0 indicates the equilibrium state, R_c is a cut-off distance (that is typically defined as $R_c = 10\text{--}14 \text{ \AA}$), and $H(x)$ is a Heaviside unit step function defined as $H(x) = 1$ if $x > 0$; otherwise, $H(x) = 0$. This ENM coupled with normal mode analysis is able to provide the elastic properties of amyloid fibrils, which is well described in [22, 27].

2.3. Continuum Model: Elastic Beam Model. Amyloid fibrils can be modeled as a one-dimensional beam model due to their structural feature in that their length is much larger than their thickness. Here, we consider the vibrational and deformation behaviors of the fibril based on Euler-Bernoulli beam theory. In addition, we present the Timoshenko beam theory useful for understanding the length-dependent mechanical properties of amyloid fibrils.

2.3.1. Vibrational Behavior of Fibril Structure. Let us consider the vibrational (bending) motion of amyloid fibril. The equation of motion for a fibril modeled based on Euler-Bernoulli beam [65] is given by

$$\rho A \partial_t^2 w(x, t) + \partial_x^2 [EI \partial_x^2 w(x, t)] = 0, \quad (7)$$

where ρ , A , E , and I represent the density, cross-sectional area, elastic modulus, and cross-sectional moment of inertia of the fibril, respectively, $w(x, t)$ is its transverse deflection, and a coordinate x is defined along the fibril axis. With assuming $w(x, t) = u(x) \cdot \exp[j\omega t]$, the equation of motion given by (7) becomes an eigenvalue problem as follows:

$$\omega^2 \rho A u = EI \partial_x^4 u. \quad (8)$$

Consequently, the frequency of the fibril is represented in the form of

$$\omega = \left(\frac{\lambda}{L} \right)^2 \sqrt{\frac{EI}{\rho A}}, \quad (9)$$

where L is the length of an amyloid fibril and λ is a boundary condition-dependent constant. Equation (9) clearly demonstrates that it is straightforward to compute the elastic modulus (or equivalently, bending rigidity) of an amyloid fibril if its natural frequency was measured from computational simulations (e.g., atomistic simulations or ENM simulations) or experiments (based on 4D electron microscopy). In addition, the torsional shear modulus and axial elastic modulus of amyloid fibrils can be also characterized based on measuring their natural frequencies corresponding to torsional (twisting) and axial stretching deformation modes, respectively. The details of extracting these torsional shear modulus and axial elastic modulus based on the elastic beam model are well described in [22, 27].

2.3.2. Mechanical (Bending) Deformation of Fibril. Let us take into account the force-driven (bending) deformation of an amyloid fibril. The governing equation for the bending deformation of a fibril due to a force is given by [66]

$$\partial_x^2 [EI \partial_x^2 w(x)] = q(x), \quad (10)$$

where $q(x)$ is a distributed load acting on the fibril. In case of a force, F , acting on the specific location ($x = x_0$) of the fibril, the governing equation given by (11) becomes the following equation:

$$\partial_x^2 [EI \partial_x^2 w(x)] = F \cdot \delta(x - x_0). \quad (11)$$

Here, $\delta(x)$ is a Dirac delta function. Consequently, the force-displacement relationship of deformed fibril is given by

$$W = \frac{FL^3}{aEI}, \quad (12)$$

where W is displacement at the location where a force is applied; that is, $W = w(x_0)$; a is a constant that depends on boundary condition and the location at which a force is applied. It is straightforward to extract the bending rigidity (or bending elastic modulus) of an amyloid fibril, if its force-displacement relationship (i.e., F versus W) is obtained from simulation or experiment.

2.3.3. Timoshenko Beam Model: Length-Dependent Property. For understanding the effect of fibril length on the bending properties of protein fibril, recent studies [22, 23, 27, 30, 52, 67] have employed the Timoshenko beam theory [68], which assumes that the deformation of the fibril is attributed to both shear and bending deformations. The total deflection of the fibril is represented in the form of

$$W = \frac{FL^3}{aEI} + \frac{cFL}{bG_s A}, \quad (13)$$

where G_s and A represent the shear modulus and cross-sectional area of an amyloid fibril, respectively, b is a boundary condition-dependent constant, and c is a shear coefficient that depends on the cross-sectional shape of an amyloid fibril.

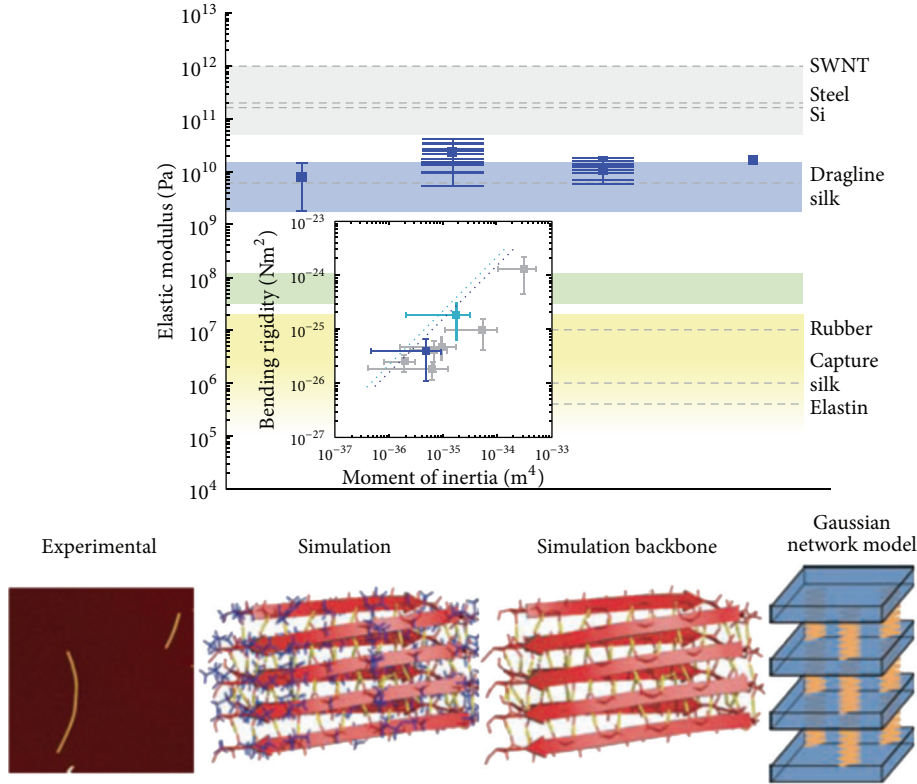


FIGURE 1: Nanomechanical properties of amyloid fibrils and the role of intermolecular forces in the nanomechanical properties. The elastic modulus of amyloid fibrils is measured in a range of 1 to 10 GPa (blue region in the graph), and this elastic modulus is comparable to that of dragline silk. The nanomechanical properties of amyloid fibrils are measured based on AFM-based single-molecule experiments and simulations such as full-atomistic simulations, backbone-based atomistic simulations, and elastic network model (as shown in figures from lower left panel to lower right panel, resp.). Figures are adopted with permission from [32].

From (13), the effective bending rigidity of an amyloid fibril is given by

$$\tilde{E}I = EI \left(1 + \frac{a}{b} \frac{cEI}{G_s AL^2} \right)^{-1}. \quad (14)$$

The Timoshenko beam theory given by (14) provides the length-dependent bending rigidity of an amyloid fibril, which is ascribed to competition between shear and bending deformations.

3. Single-Molecule Force Spectroscopy-Based Mechanical Characterization of Amyloid Fibrils

Single-molecule force spectroscopy based on optical tweezer or AFM is a useful experimental toolkit that allows for mechanical characterization of protein materials at molecular scale [69–72]. For a recent decade, single-molecule force spectroscopy has been utilized to probe the mechanical properties of amyloid fibrils [10, 45]. Here, we briefly provide the recent key efforts to experimentally characterize the nanomechanical properties of amyloid fibrils using force spectroscopy based on AFM.

In recent years, Knowles and coworkers [32] have reported the nanomechanical properties of amyloid fibrils

using AFM imaging experiments coupled with polymer chain statistics that is described in Section 2.1. In particular, they measured the fluctuation of angle between two tangent vectors, which results in the extraction of mechanical properties such as persistent length—for example, see (3)—from the AFM images of amyloid fibrils. The nanomechanical properties of several amyloid fibrils such as α -lactalbumin fibril, insulin β -chain fibril, β -lactoglobulin fibril, insulin fibril, and TTR (105–115) fibril were measured using AFM imaging experiments coupled with polymer chain statistics. The bending elastic modulus of these fibrils is measured in a range of 1 to 10 GPa (Figure 1). They found that, based on AFM experiments and simulations such as atomistic simulations and ENM, the excellent mechanical properties of these fibrils are attributed to intermolecular forces that act between β -sheet layers (Figure 1). In addition, they reported that the elastic modulus of amyloid fibril is close to that of mechanically strong spider silk protein and that the fracture property of amyloid fibril is related to the growth mechanisms of amyloid fibrils [26].

Recently, Adamcik and colleagues have reported the nanomechanical properties of multistranded amyloid fibrils using AFM imaging experiments together with polymer chain statistics [16] (Figure 2). They reported that amyloid fibrils can be formed as a multistranded fibril that is

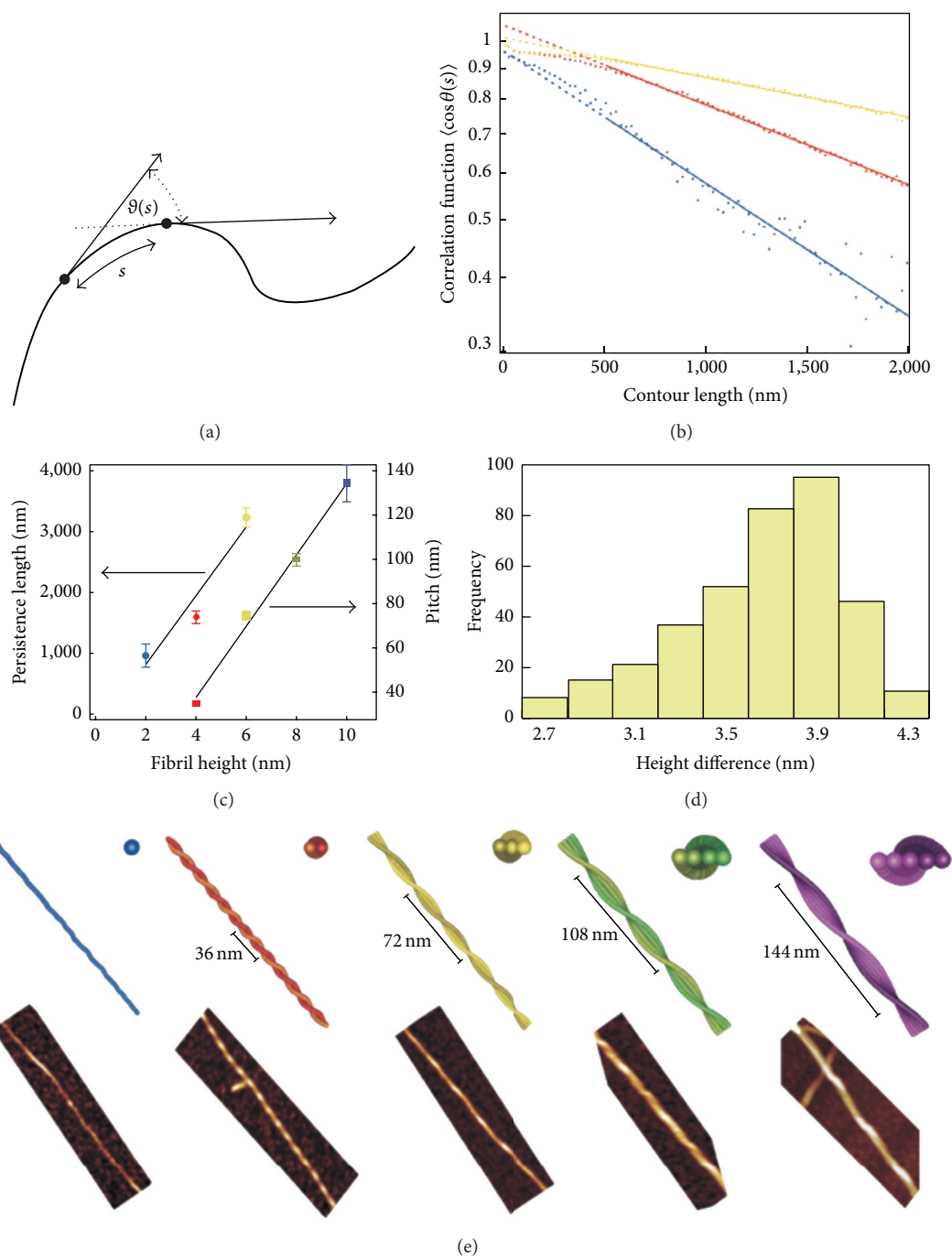


FIGURE 2: Nanomechanical properties of multistranded amyloid fibrils. (a) Schematic illustration of measuring the angle between two tangent vectors to extract the mechanical properties of the fibril using polymer chain statistics. (b) The ensemble averages of correlation functions (defined as cosine values of angles) for a multistranded fibril made of single (blue), two (red), and three (yellow) filaments, respectively, are measured from AFM experiments. The measured experimental results (indicated by blue, red, and yellow dots) are well fitted to theoretical predictions from polymer chain statistics (indicated by blue, red, and yellow lines). (c) Persistence length and helical pitch for amyloid fibrils composed of single, two, and three filaments, respectively. (d) The distribution of the difference between maximum and minimum AFM heights (thicknesses) of amyloid fibrils. (e) AFM images (shown in lower panel) and corresponding coarse-grained models (shown in upper panel) provide the left-handed multistranded amyloid fibrils made of one to five filaments, respectively. Figures are adopted with permission from [16].

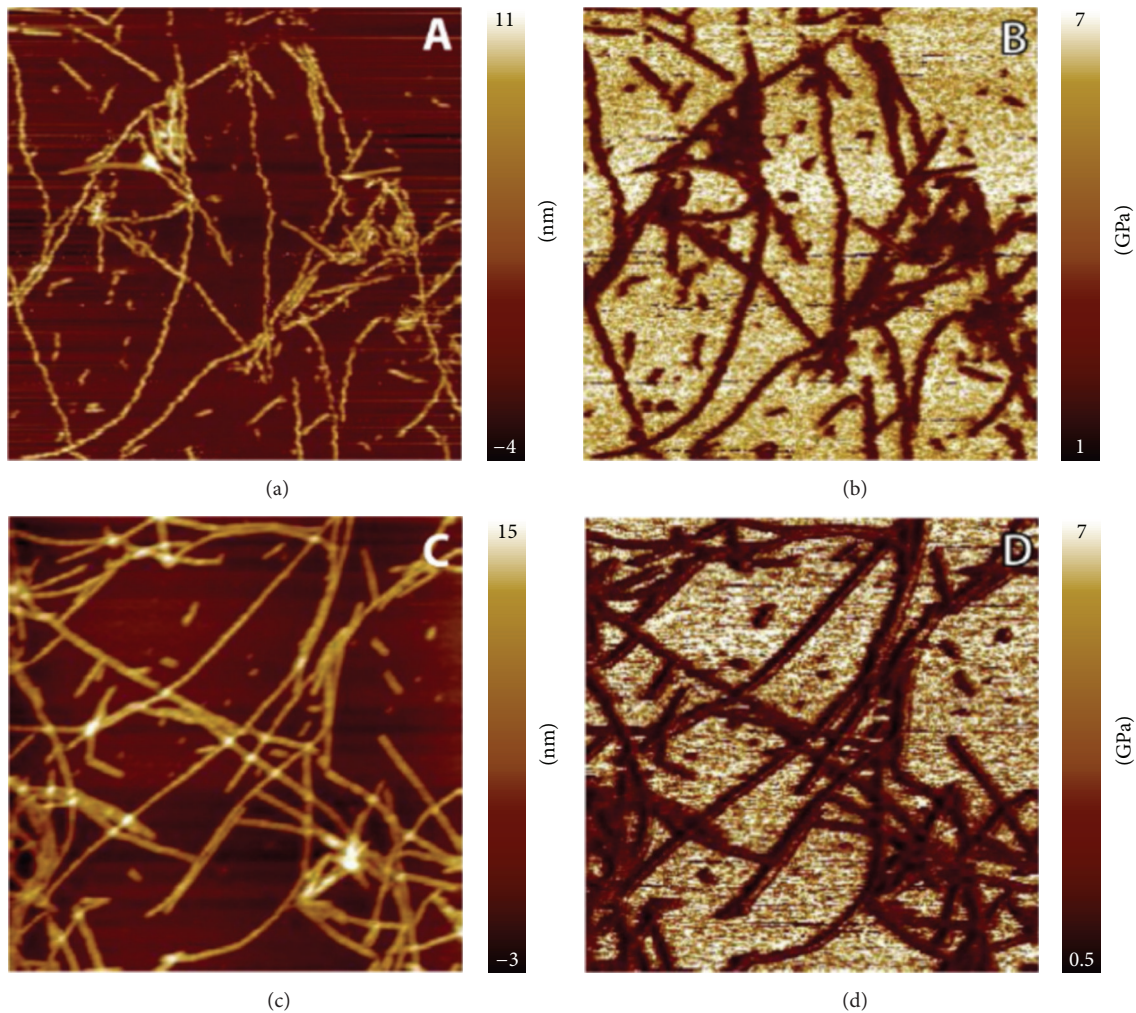


FIGURE 3: AFM peak force QNM- (quantitative nanomechanical mapping-) based experiments of α -synuclein amyloid fibrils. (a) and (c) show the AFM topographic images of the fibrils, while (b) and (d) present the AFM peak force QNM images of the fibrils. Here, (a) and (b) are obtained from AFM QNM experiments of the fibrils in liquid environment, while (c) and (d) are acquired based on AFM QNM imaging of the fibrils in ambient condition. Figures are adopted from [20] under Creative Commons Attribution (CCA).

composed of single to five filaments. They found that the helical structure of a multistranded amyloid fibril is determined by interaction between filaments comprising the fibril. In addition, the persistent length of amyloid fibril is critically dependent on the number of filaments comprising the fibril such that the persistent length of the fibril increases with respect to the number of filaments. This has been elucidated based on helical ribbon model, which suggests that the increase of persistent length with respect to the number of filaments is attributed to the fact that the cross-sectional moment of inertia of the fibril increases with respect to the number of filaments. Furthermore, Usov and Mezzenga elaborated the theoretical model based on continuum elastic (beam) theory in order to understand the nanomechanical properties of amyloid fibrils with respect to their various conformations based on AFM experiments of the fibrils [73].

In addition to AFM imaging experiment, AFM-based nanoindentation has been considered to characterize the

mechanical properties of amyloid fibrils. Adamcik and colleagues employed an AFM-based peak force QNM (quantitative nanomechanical mapping) technique to characterize the nanomechanical properties of β -lactoglobulin amyloid fibrils [19]. They found that the elastic modulus of β -lactoglobulin fibril is estimated as 3.3 GPa. A recent study by Sweers and coworkers [20] has suggested that the elastic modulus of α -synuclein fibril was measured as 1.3~2.1 GPa from AFM-based peak force QNM experiments (Figure 3). A previous study by Guo and Akhremitchev [21] reports the elastic modulus of insulin fibrils using AFM indentation experiments. Their study provides that the elastic modulus of insulin fibril is measured in a range of 5 to 50 MPa. In recent years, Gsponer and colleagues [28] utilized the AFM experiments (based on amplitude modulation-frequency modulation imaging, referred to as AM-FM imaging) to measure the mechanical properties of prion amyloid fibrils. They found that the radial elastic modulus of prion fibrils

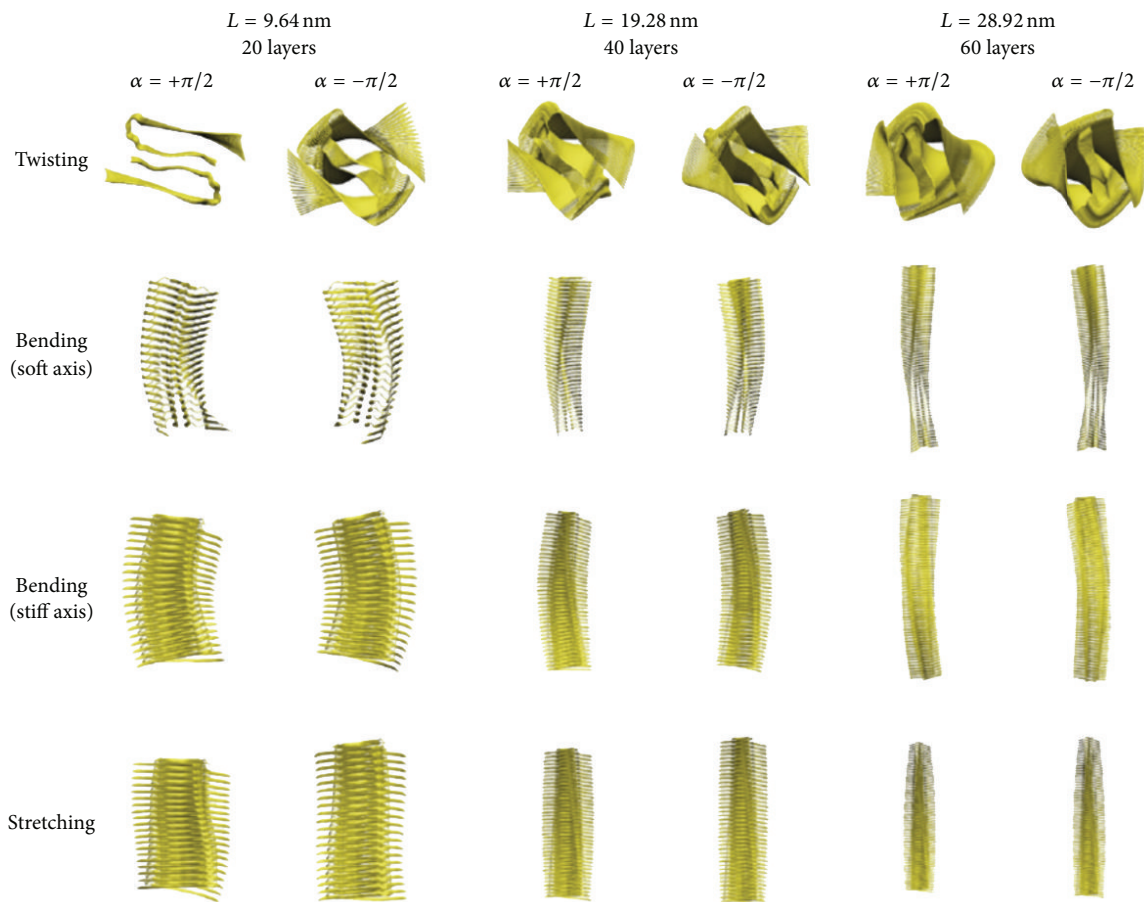


FIGURE 4: Vibrational characteristics of $A\beta$ amyloid fibrils computed from elastic network model. Four low-frequency vibrational modes correspond to the twisting, two bending, and axial stretching modes, respectively. Here, low-frequency vibrational modes are shown for three different types of $A\beta$ amyloid fibrils with their length of 9.64, 19.28, and 28.92 nm, respectively. Figures are adopted with permission from [27].

is measured in a range of 0.5 to 1.3 GPa and that this radial elastic property critically depends on their thickness in such a way that the radial elastic modulus of the fibrils decreases as their thickness increases.

4. Computational Simulation-Based Mechanical Characterization of Amyloid Fibrils

4.1. Nanomechanical Characterization Based on the Vibration of Amyloid Fibrils. A recent study by Xu and coworkers [27] considers ENM simulations to measure the vibrational characteristics of $A\beta$ fibrils and their elastic properties. They found that the low-frequency dynamic modes of these fibrils correspond to twisting, bending, or axial stretching deformation modes (Figure 4) and that the elastic moduli of amyloid fibrils are dependent on their length scales. In addition, they report that the twisting (or helical) conformation of amyloid fibrils results in their isotropic bending property when the fibril length is >150 nm. Recently, our previous study [22] reports the nanomechanical properties of human

islet amyloid polypeptide (hIAPP) fibrils, which are formed based on four different types of steric zipper patterns, based on ENM simulations. We found that as the fibril length increases, the torsional and axial stretching deformation modes of the fibril become the high-frequency dynamic modes, while the bending deformation mode corresponds to the low-frequency mode independent of fibril length (Figure 5(a)). This indicates that the thermal fluctuation behavior of an amyloid fibril is mostly contributed by the bending deformation mode, that is, a low-frequency mode. In addition, we have shown that the dependence of the bending rigidity (or persistent length) of amyloid fibrils on their length scales is well fitted to Timoshenko beam model (Figure 5(b)), which suggests that the bending property of the fibrils is attributed to competition between shear and bending deformation modes. Moreover, we have also studied the nanomechanical properties of prion amyloid fibrils based on ENM [30]. It is found that the mechanical properties of prion fibrils significantly depend on their β -helical structures and that the length-dependent mechanical properties of prion fibrils provide an insight into their critical size, at which prion infectivity is maximized.

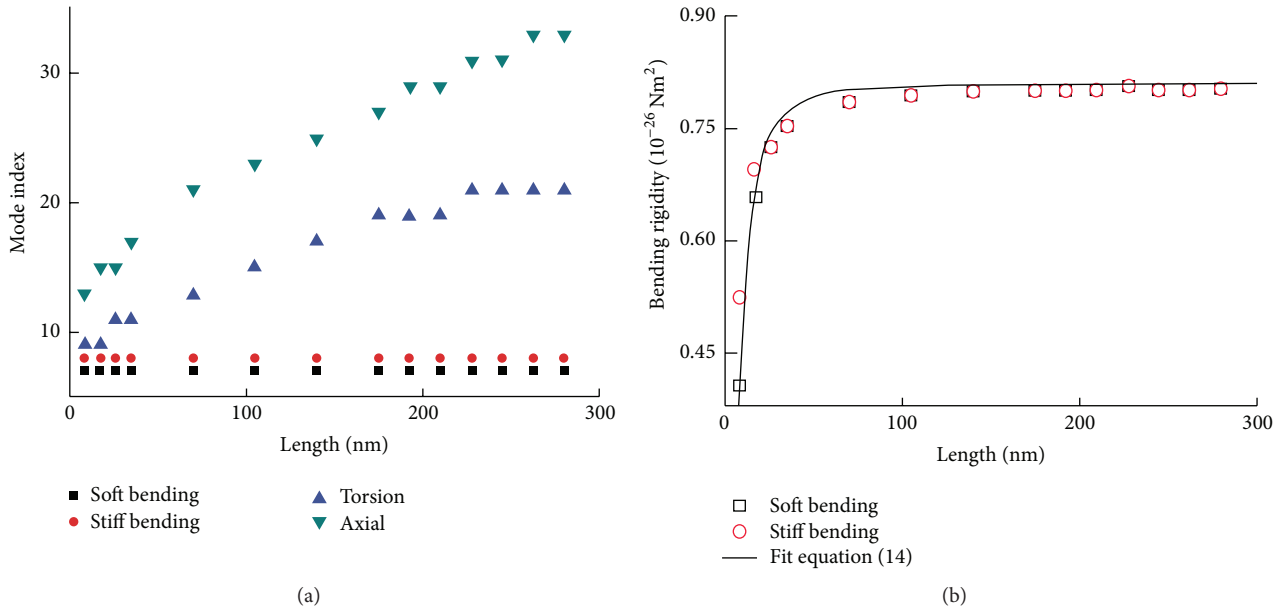


FIGURE 5: Length-dependent vibrational and nanomechanical properties of human islet amyloid polypeptide (hIAPP) fibrils computed from the elastic network model. (a) The mode index for three dominant deformation modes such as bending, torsional, and axial stretching deformation modes, respectively, is shown as a function of fibril length. As the fibril length increases, the torsional and axial deformation modes become the high-frequency vibrational modes, while the bending deformation modes are the low-frequency vibrational modes without any dependence on the fibril length. (b) The bending rigidity of hIAPP amyloid fibrils is shown as a function of their length scales based on ENM simulations. Figures are adopted with permission from [22].

In recent years, we have studied the vibrational characteristics of hIAPP (20–29) fibrils, which are formed based on the eight possible conformations of the fibrils as suggested in [33, 74] (Figure 6(a)), based on atomistic molecular dynamics (MD) simulations together with continuum elastic beam model [24]. We have shown that the fibril structure becomes stable when the fibril is formed based on antiparallel stacking of β -sheets (Figure 6(b)) and that the frequencies of the fibrils for their bending deformation modes are measured in the order of 0.2 THz, which is much larger than the frequencies measured by 4D electron microscopy experiments [36]. The discrepancy between frequencies measured from MD simulations and 4D electron microscopy experiments is attributed to the fact that the fibril length considered for MD simulation is less by a few orders of magnitude than that for 4D electron microscopy experiment. In addition, we have shown that the bending rigidity of hIAPP fibril becomes optimized when the fibril is formed based on the antiparallel stacking and that the mutation of phenylalanine to leucine in hIAPP (20–29) leads to the decrease of not only the structural stability but also the bending rigidity of hIAPP (20–29) fibril. Moreover, a recent study by Chang et al. [75] reports the effect of aromatic residue (i.e., phenylalanine) on the vibrational characteristics and mechanical properties of $A\beta$ amyloid fibrils using MD simulations coupled with continuum elastic beam model. They found that aromatic residue such as phenylalanine plays a key role in stabilizing the structure of amyloid fibrils and in optimizing their mechanical properties.

Our recent study [34] reports the structure and vibrational (or equivalently mechanical) properties of a multistranded amyloid fibril by using atomistic MD simulations coupled with ENM. Specifically, MD simulation was used to understand the structure of a multistranded β_2 -microglobulin fibril, whereas ENM was utilized to characterize their vibrational and mechanical properties (Figure 7(a)). Our previous study found that the dependence of the helical structure of β_2 -microglobulin fibril on the number of filaments comprising the fibril is attributed to the nonbonded interactions between filaments, which is consistent with AFM-based experimental study of β -lactoglobulin fibril [16]. In particular, MM-PBSA calculations suggest that as the number of filaments comprising the β_2 -microglobulin fibril increases, the molecular mechanics energy of the fibril is decreased and it is mostly contributed by nonbonded energy such as electrostatic and van der Waals interaction energies [34]. Moreover, our previous study suggests the persistent length of amyloid fibrils as a function of the number of filaments comprising the fibril with using ENM simulation coupled with continuum beam model. The dependence of the persistent length on the number of filaments is well fitted to a scaling law of $L_p \propto [(nq)^2 - \sin^2(nq)]^{1/2}$ for a helical fibril model [73] (Figure 7(b)).

4.2. Mechanical Deformation Mechanisms of Amyloid Fibrils. Mechanical characterization of amyloid fibrils based on measuring their vibrational characteristics is insufficient to gain insight into the mechanical behaviors and properties

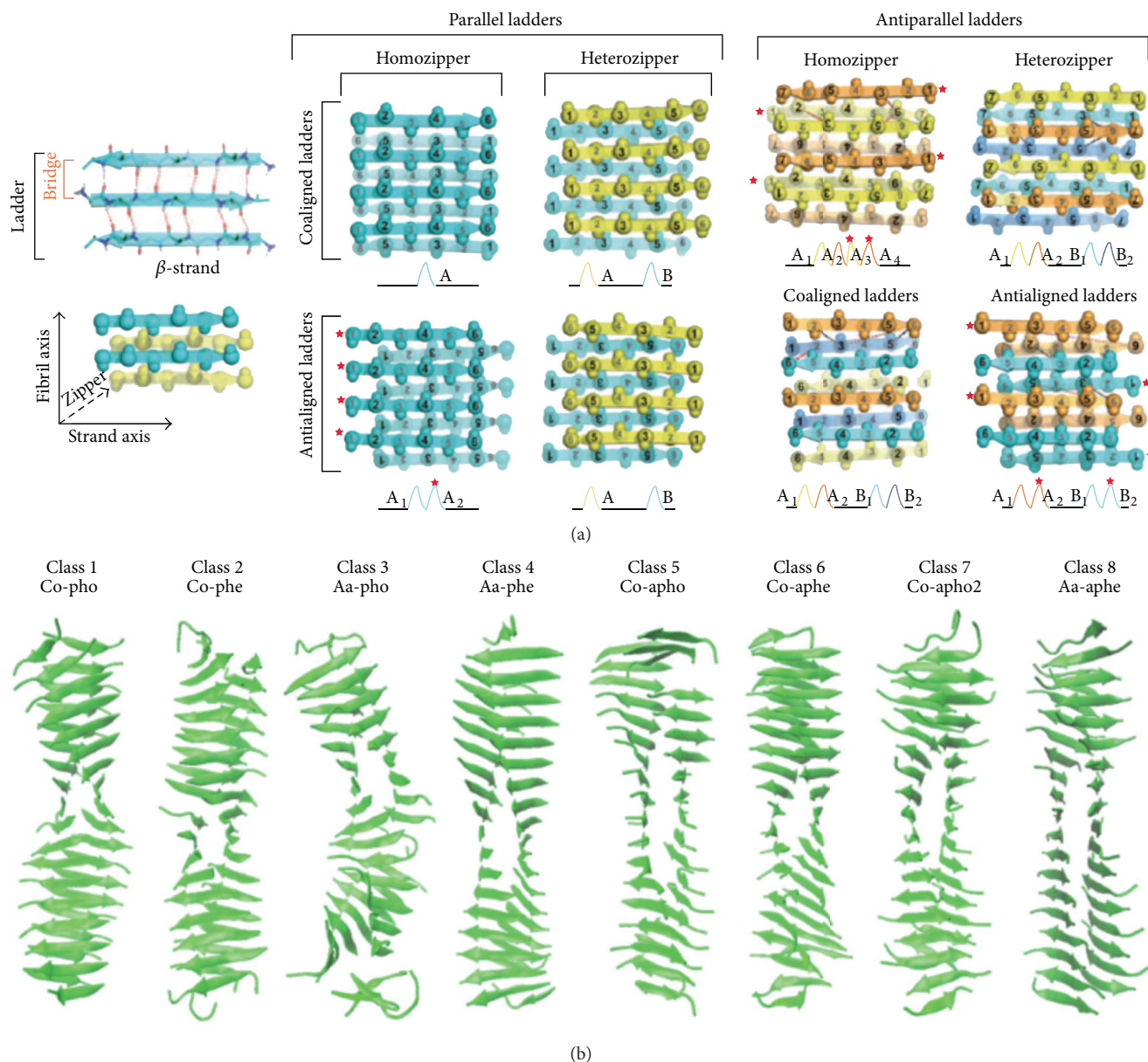


FIGURE 6: (a) Structural models of amyloid fibrils. These structural models are theoretically provided based on β -sheet stacking patterns such as parallel or antiparallel stacking. Figures are adopted with permission from [33]. (b) Atomistic molecular dynamics simulations provide the equilibrium structures of hIAPP amyloid fibrils based on the structural models. Figures are adopted from [24] under Creative Commons Attribution (CCA).

of amyloid fibrils, as the vibrational properties of the fibrils are correlated with only their elastic moduli [76]. In particular, the vibrational characteristics of amyloid fibrils cannot provide the quantitative insight into the fracture behaviors and properties of amyloid fibrils. Here, we take a look at the mechanical deformation mechanisms and properties of amyloid fibrils based on two types of deformation modes such as (i) axial deformation and (ii) bending-like deformation.

First, we consider recent attempts to characterize the axial deformation behavior of amyloid fibrils. A recent study by Dong et al. [35] reports the axial extension of prion fibrils

using optical tweezer force spectroscopy. In their experiment [35], it is found that the prion fibrils can resist force up to 250 pN and that discontinuities in the force-extension curve (before the fibril is ruptured) are observed possibly due to the partial unfolding of prion proteins comprising the fibril (Figure 8). SMD simulation-based study by Lee et al. [77] provides that the mechanical behavior of polymorphic amyloid fibrils is critically dependent on their molecular structures. In particular, an amyloid fibril formed based on antiparallel stacking of β -sheets can sustain a force even up to ~ 1500 pN. This value of the force is larger than a force that other fibrils, which are formed based on other stacking

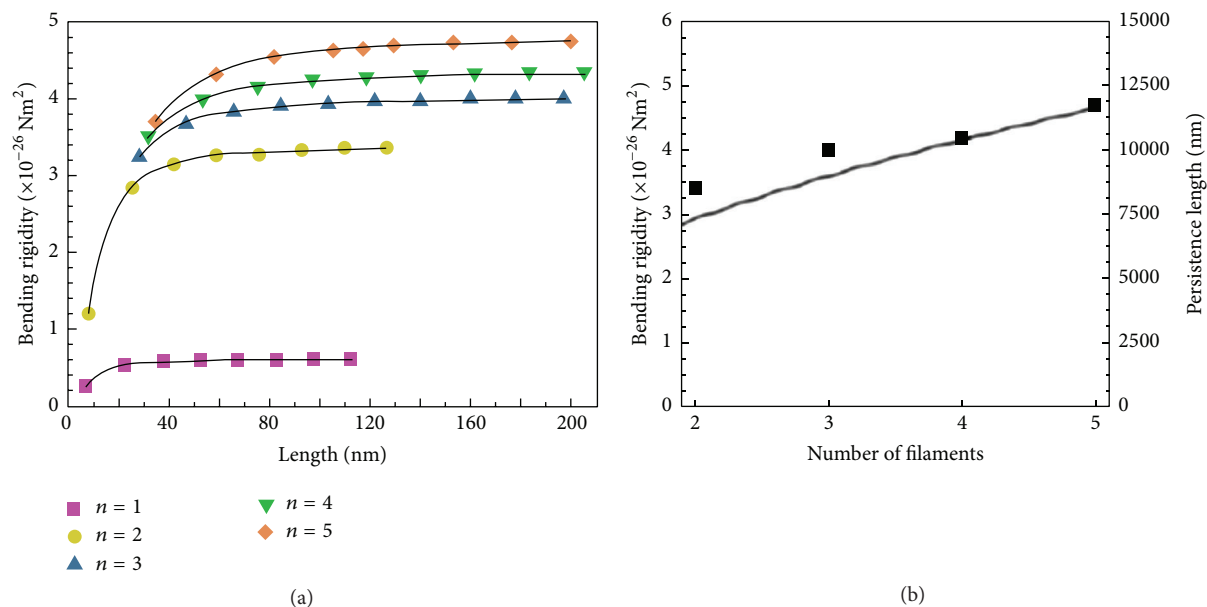


FIGURE 7: Nanomechanical properties of β_2 -microglobulin fibrils made of one to five filaments, respectively. (a) The length-dependent effective bending rigidity of β_2 -microglobulin fibrils composed of one to five filaments, respectively. (b) The intrinsic bending rigidity of β_2 -microglobulin fibrils made of two to five filaments, respectively, is shown as a function of the number of filaments comprising the fibrils. The dots indicate the results of ENM simulations, while solid line presents the theoretical prediction from continuum helical fibril model. Figures are adopted with permission from [34].

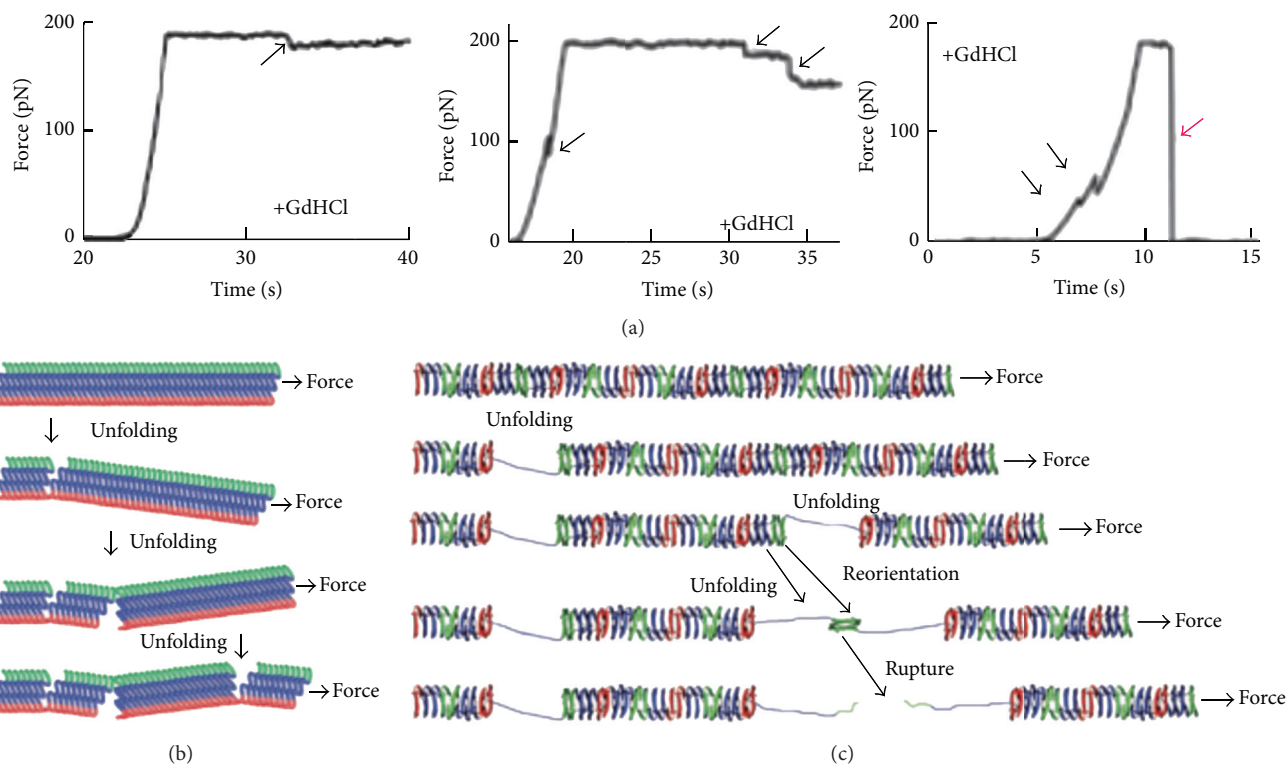


FIGURE 8: Optical tweezer-based stretching experiment of prion fibrils. (a) Three representative force curves for prion fibril when it is extended with a constant pulling speed. Arrows indicate discontinuities in a force-extension curve due to partial unfolding of prion proteins. (b) Fracture mechanism of amyloid fibril made of β -helices due to partial unfolding. (c) Fracture mechanism of amyloid fibril made of β -sheets due to partial unfolding. Figures are adopted with permission from [35].

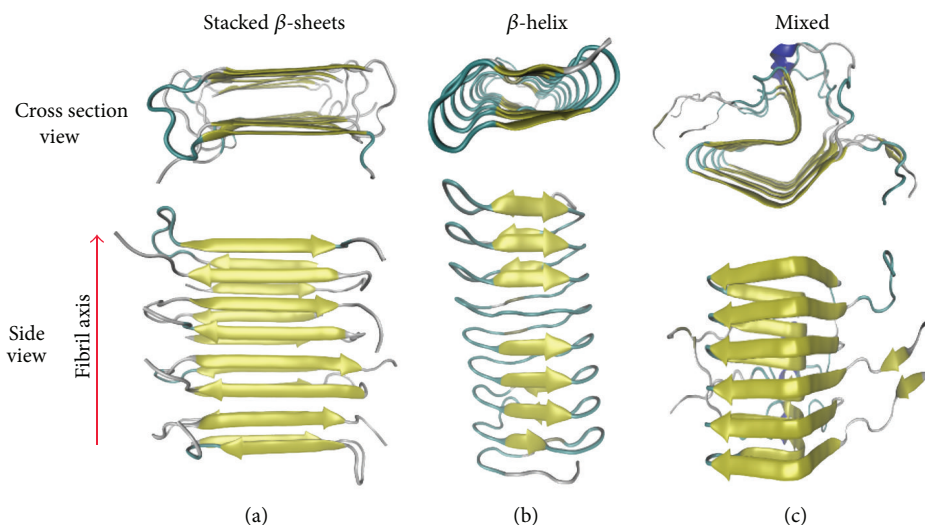


FIGURE 9: Three different structural types of amyloid fibrils. Amyloid fibrils can be formed based on (a) stacked β -sheets, (b) β -helices, or (c) stacked β -helices. Figures are redrawn using VMD package for these three types of structures, whose information is provided in the protein data bank (PDB) with PDB codes of 2LNQ, 1P9H, and 2KJ3, respectively.

patterns, can resist. In recent years, Solar and Buehler [29] report the tensile deformation and failure of amyloid fibrils using SMD simulations. They considered three types of amyloid fibrils based on their structural features (Figure 9): (a) a fibril formed based on stacking of β -sheets, (b) a fibril constructed based on β -helix, and (c) a fibril established based on mixed structure, that is, stacking of β -helices. The mechanical strength of an amyloid fibril can be maximized (i.e., up to 1000 MPa) when it is formed based on a mixed structure. By contrast, the strength is estimated as 200~400 MPa for a fibril formed by stacking of β -sheets, and it is measured as ~600 MPa for the fibril constructed based on β -helix.

Now, we take into account recent efforts to characterize the bending deformation of an amyloid fibril. A previous study by Smith et al. [26] reports the three-point bending-like deformation of an amyloid fibril using atomic force microscopy (AFM) experiment. It is found that the insulin amyloid fibril exhibits the elastic modulus of ~3.3 GPa, mechanical strength of ~600 MPa, and bending rigidity of $\sim 9.1 \times 10^{-26} \text{ N}\cdot\text{m}^2$, respectively. Our previous study [23] considers the bending deformation mechanisms of amyloid fibrils using SMD simulations. In our previous study, it was found that the deformation mechanism of amyloid fibrils is significantly dependent on their length scales (Figure 10(a)). In particular, when a short fibril is deformed, it undergoes shear-like deformation. By contrast, the bending deformation occurs when a long fibril is deformed. Furthermore, it was shown that Timoshenko beam model is able to capture the length-dependent stiffness of amyloid fibrils (Figure 10(b)) and that their length-dependent fracture behavior (Figure 10(c)) is attributed to the length-dependent mechanisms of hydrogen bond ruptures [23]. In addition, our recent study [78] has shown the effect of boundary conditions in the fracture behavior of amyloid fibrils. Moreover, a recent

study by Kim et al. [79] provides the anisotropic bending deformation mechanisms of hIAPP amyloid fibrils using atomistic SMD simulations. Their study has shown that the fracture property (e.g., rupture force) of amyloid fibril is critically dependent on bending direction, which highlights the important role of loading mode in the fracture properties of amyloid fibrils.

5. Discussion

In this review article, we address recent attempts to characterize the nanomechanical properties of amyloid fibrils measured from computational simulations and/or AFM experiments together with theoretical models. The nanomechanical properties of amyloid fibrils are summarized in Table 1, which shows that the elastic modulus of amyloid fibrils is evaluated in the order of 1 to 10 GPa and that their mechanical strength is measured in the order of 1 GPa. It should be noted that though both amyloid fibril and spider silk crystal are made of stacked β -sheets, the mechanical strength of amyloid fibril is less than that of a spider silk crystal, which is attributed to the different orientation of stacked β -sheets with respect to the fibril axis [31].

Here, we note that most of recent works reviewed in this work do not consider the effect of physiological conditions in the nanomechanical properties of amyloid fibrils. It has recently been found that physiological conditions play a crucial role in the formation and structure of amyloid proteins. For instance, a recent study by Lee et al. [80] reports a critical role that the physiological condition such as the pH of a solvent plays in the morphology of amyloid fibrils. In addition, Mizuno and coworkers [81] found the dependence of HET-s prion amyloid fibril structure on the pH of a solvent. Moreover, it has been debated whether metal ion promotes the formation of amyloid oligomers or fibrils, as previous

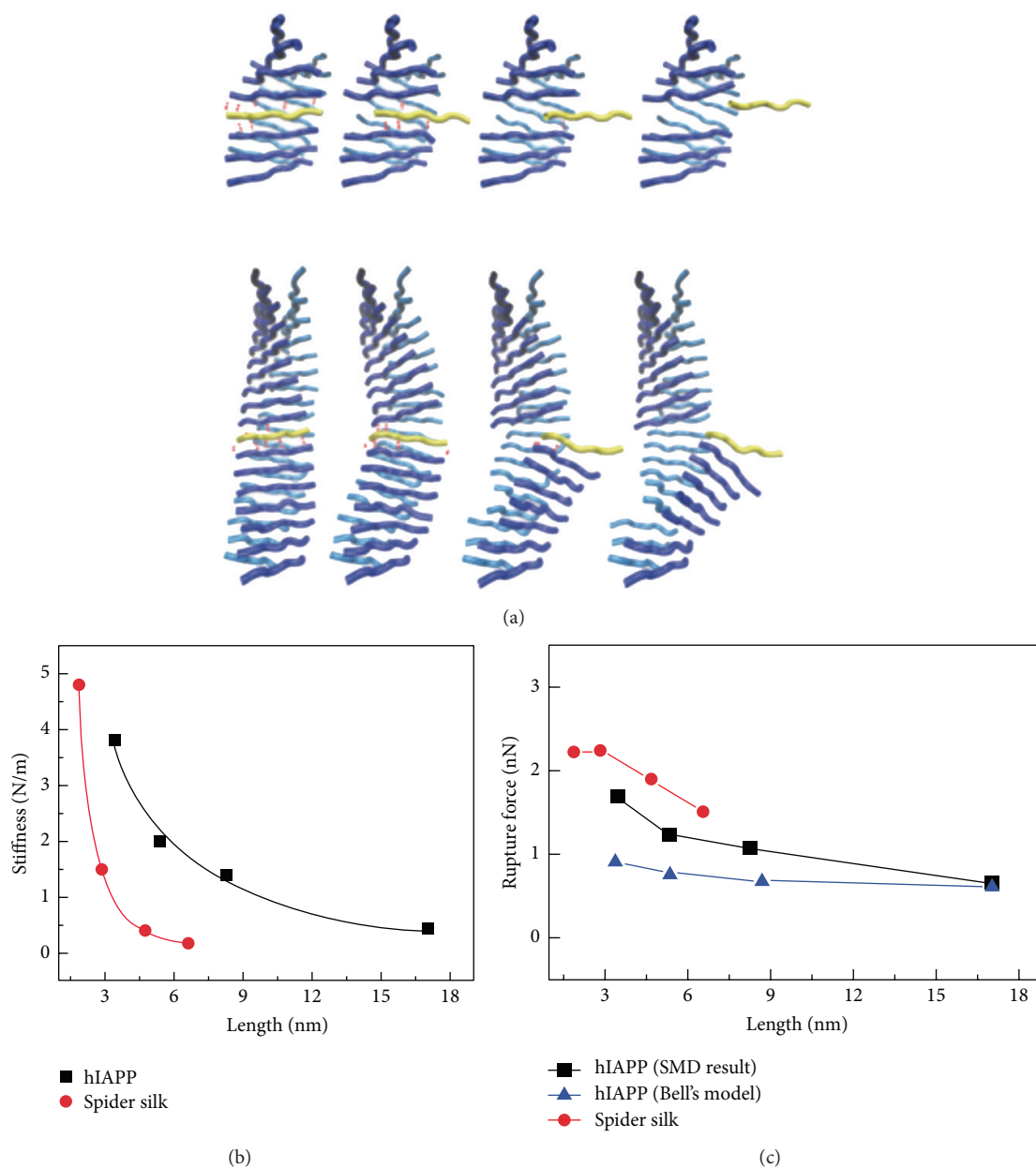


FIGURE 10: (a) Length-dependent mechanical deformation mechanisms of amyloid fibrils. The upper panel shows the shear-like deformation of a short fibril, while the lower panel provides the bending deformation of a long fibril. (b) Length-dependent elastic stiffness of amyloid fibrils (black) and spider silk crystals (red). (c) Length-dependent rupture forces of amyloid fibrils (black) and spider silk crystals (red). Figures are adopted with permission from [23].

studies [82–84] report that the high concentration of metal ions was found for patients suffering from neurodegenerative diseases. In addition, recent studies [85, 86] have shown the important role of metal ion in the formation and structure of amyloid fibrils. Despite these recent studies showing the role of physiological condition in the formation and structure of amyloid proteins, how physiological condition may make an impact on the nanomechanical properties of amyloid fibrils has remained elusive. Future studies may be directed towards understanding how physiological

conditions affect the nanomechanical properties of amyloid fibrils.

In conclusion, this review article summarizes the excellent nanomechanical properties of amyloid fibrils, which are measured with using experiments (based on AFM) and computational simulations (based on atomistic simulations or ENM). The nanomechanical characterization of amyloid fibrils may allow for further insight into not only the mechanics-driven biological functions of the fibrils but also the design principles showing how the

TABLE 1: Nanomechanical properties of amyloid fibrils measured from simulations and experiments.

Material	Measurement method	Length (nm)	Bending rigidity ($\times 10^{-26}$ N·m ²)	Young's modulus (GPa)	Shear modulus (GPa)	Strength (GPa)	Ref.
hIAPP ₂₀₋₂₉ fibril	Steered molecular dynamics (simulation)	3.41–17.5	7.73–37.7		5.97–6.71	4–8	[23]
hIAPP ₂₀₋₂₉ fibril	Elastic network model (simulation)	10–300	~8	12–14	1.1		[22]
hIAPP ₂₀₋₂₉ fibril	Molecular dynamics (simulation)	10	0.01–0.04	0.4–0.6			[24]
A β ₁₋₄₀ fibril	Cryoelectron microscopy (experiment)	500–1000	~13		0.0127		[17]
A β ₁₋₄₀ fibril	Elastic network model (simulation)	~30	21–63		4.3–5.6		[27]
β -lactoglobulin fibril	AFM imaging experiment	500–15,000	0.4–1.6	~4			[16]
β -lactoglobulin fibril	AFM indentation experiment (peak force QNM)	500–15,000		3.3			[19]
Mouse prion fibril	AFM experiments (AM-FM imaging)	>1000		0.5–1.36			[28]
α -synuclein fibril	AFM indentation (peak force QNM)	>1000		1.2 \pm 0.2			[20]
Insulin fibril	AFM bending experiment	>~1500	~9.1		~0.28		[26]
Insulin fibril	AFM imaging experiment	>~2000	~17		~0.13		[26]
HET-s prion fibril	Steered molecular dynamics (simulation)	5.38		9.8		0.917	[29]
HET-s prion fibril	Elastic network model (simulation)	8.93	0.115	1.5			[30]
Spider silk crystal	Steered molecular dynamics (simulation)	2–7	~2.8		4.6		[12]
Spider silk crystal	Steered molecular dynamics (simulation)			30–70			[31]

properties of protein materials can be determined or controlled.

Disclosure

The funder had no role in publishing this paper.

Competing Interests

The authors declare there are no competing interests regarding the publication of this paper.

Authors' Contributions

Bumjoon Choi and Taehee Kim made equal contribution to this work.

Acknowledgments

This work was supported by the National Research Foundation of Korea (NRF), under Grant no. NRF-2015RIA2A2A04002453, and Korea Institute of Science and

Technology Information (KISTI) under Grant no. KSC-2015-C3-051 (to Kilho Eom) and NRF under Grant no. NRF-2013RIA1A2053613 (to Sang Woo Lee).

References

- [1] I. Cherny and E. Gazit, "Amyloids: not only pathological agents but also ordered nanomaterials," *Angewandte Chemie—International Edition*, vol. 47, no. 22, pp. 4062–4069, 2008.
- [2] B. H. Toyama and J. S. Weissman, "Amyloid structure: conformational diversity and consequences," *Annual Review of Biochemistry*, vol. 80, pp. 557–585, 2011.
- [3] J. E. Straub and D. Thirumalai, "Toward a molecular theory of early and late events in monomer to amyloid fibril formation," *Annual Review of Physical Chemistry*, vol. 62, pp. 437–463, 2011.
- [4] G. Lee, W. Lee, H. Lee, C. Y. Lee, K. Eom, and T. Kwon, "Self-assembled amyloid fibrils with controllable conformational heterogeneity," *Scientific Reports*, vol. 5, Article ID 16220, 2015.
- [5] M. B. Pepys, "Amyloidosis," *Annual Review of Medicine*, vol. 57, pp. 223–241, 2006.
- [6] F. Chiti and C. M. Dobson, "Protein misfolding, functional amyloid, and human disease," *Annual Review of Biochemistry*, vol. 75, pp. 333–366, 2006.

- [7] G. Merlini and V. Bellotti, "Molecular mechanisms of amyloidosis," *The New England Journal of Medicine*, vol. 349, no. 6, pp. 583–596, 2003.
- [8] J. W. M. Höppener, B. Ahrén, and C. J. M. Lips, "Islet amyloid and type 2 diabetes mellitus," *The New England Journal of Medicine*, vol. 343, no. 6, pp. 411–419, 2000.
- [9] C. Haass and D. J. Selkoe, "Soluble protein oligomers in neurodegeneration: lessons from the Alzheimer's amyloid β -peptide," *Nature Reviews Molecular Cell Biology*, vol. 8, no. 2, pp. 101–112, 2007.
- [10] T. P. J. Knowles and M. J. Buehler, "Nanomechanics of functional and pathological amyloid materials," *Nature Nanotechnology*, vol. 6, no. 8, pp. 469–479, 2011.
- [11] C. Rapezzi, C. C. Quarta, L. Riva et al., "Transthyretin-related amyloidoses and the heart: a clinical overview," *Nature Reviews Cardiology*, vol. 7, no. 7, pp. 398–408, 2010.
- [12] S. Keten, Z. Xu, B. Ihle, and M. J. Buehler, "Nanoconfinement controls stiffness, strength and mechanical toughness of β -sheet crystals in silk," *Nature Materials*, vol. 9, no. 4, pp. 359–367, 2010.
- [13] K. Eom, P.-C. Li, D. E. Makarov, and G. J. Rodin, "Relationship between the mechanical properties and topology of cross-linked polymer molecules: parallel strands maximize the strength of model polymers and protein domains," *The Journal of Physical Chemistry B*, vol. 107, no. 34, pp. 8730–8733, 2003.
- [14] C. C. Vandennakker, M. F. M. Engel, K. P. Velikov, M. Bonn, and G. H. Koenderink, "Morphology and persistence length of amyloid fibrils are correlated to peptide molecular structure," *Journal of the American Chemical Society*, vol. 133, no. 45, pp. 18030–18033, 2011.
- [15] F. S. Ruggeri, J. Adamcik, J. S. Jeong, H. A. Lashuel, R. Mezzenga, and G. Dietler, "Influence of the β -sheet content on the mechanical properties of aggregates during amyloid fibrillization," *Angewandte Chemie—International Edition*, vol. 54, no. 8, pp. 2462–2466, 2015.
- [16] J. Adamcik, J.-M. Jung, J. Flakowski, P. De Los Rios, G. Dietler, and R. Mezzenga, "Understanding amyloid aggregation by statistical analysis of atomic force microscopy images," *Nature Nanotechnology*, vol. 5, no. 6, pp. 423–428, 2010.
- [17] C. Sachse, N. Grigorieff, and M. Fändrich, "Nanoscale flexibility parameters of Alzheimer amyloid fibrils determined by electron cryo-microscopy," *Angewandte Chemie—International Edition*, vol. 49, no. 7, pp. 1321–1323, 2010.
- [18] I. Usov and R. Mezzenga, "FiberApp: an open-source software for tracking and analyzing polymers, filaments, biomacromolecules, and fibrous objects," *Macromolecules*, vol. 48, no. 5, pp. 1269–1280, 2015.
- [19] J. Adamcik, A. Berquand, and R. Mezzenga, "Single-step direct measurement of amyloid fibrils stiffness by peak force quantitative nanomechanical atomic force microscopy," *Applied Physics Letters*, vol. 98, no. 19, Article ID 193701, 2011.
- [20] K. Sweers, K. van der Werf, M. Bennink, and V. Subramaniam, "Nanomechanical properties of α -synuclein amyloid fibrils: a comparative study by nanoindentation, harmonic force microscopy, and Peakforce QNM," *Nanoscale Research Letters*, vol. 6, no. 1, article 270, 2011.
- [21] S. Guo and B. B. Akhremitchev, "Packing density and structural heterogeneity of insulin amyloid fibrils measured by AFM nanoindentation," *Biomacromolecules*, vol. 7, no. 5, pp. 1630–1636, 2006.
- [22] G. Yoon, J. Kwak, J. I. Kim, S. Na, and K. Eom, "Mechanical characterization of amyloid fibrils using coarse-grained normal mode analysis," *Advanced Functional Materials*, vol. 21, no. 18, pp. 3454–3463, 2011.
- [23] B. Choi, G. Yoon, S. W. Lee, and K. Eom, "Mechanical deformation mechanisms and properties of amyloid fibrils," *Physical Chemistry Chemical Physics*, vol. 17, no. 2, pp. 1379–1389, 2015.
- [24] G. Yoon, M. Lee, J. I. Kim, S. Na, and K. Eom, "Role of sequence and structural polymorphism on the mechanical properties of amyloid fibrils," *PLoS ONE*, vol. 9, no. 2, article e88502, 2014.
- [25] J. M. Gosline, P. A. Guerette, C. S. Ortlepp, and K. N. Savage, "The mechanical design of spider silks: from fibroin sequence to mechanical function," *Journal of Experimental Biology*, vol. 202, no. 23, pp. 3295–3303, 1999.
- [26] J. F. Smith, T. P. J. Knowles, C. M. Dobson, C. E. MacPhee, and M. E. Welland, "Characterization of the nanoscale properties of individual amyloid fibrils," *Proceedings of the National Academy of Sciences of the United States of America*, vol. 103, no. 43, pp. 15806–15811, 2006.
- [27] Z. Xu, R. Pappalardo, and M. J. Buehler, "Alzheimer's $A\beta(1-40)$ amyloid fibrils feature size-dependent mechanical properties," *Biophysical Journal*, vol. 98, no. 10, pp. 2053–2062, 2010.
- [28] G. Lamour, C. K. Yip, H. Li, and J. Gsponer, "High intrinsic mechanical flexibility of mouse prion nanofibrils revealed by measurements of axial and radial young's moduli," *ACS Nano*, vol. 8, no. 4, pp. 3851–3861, 2014.
- [29] M. Solar and M. J. Buehler, "Tensile deformation and failure of amyloid and amyloid-like protein fibrils," *Nanotechnology*, vol. 25, no. 10, Article ID 105703, 2014.
- [30] G. Yoon, Y. K. Kim, K. Eom, and S. Na, "Relationship between disease-specific structures of amyloid fibrils and their mechanical properties," *Applied Physics Letters*, vol. 102, no. 1, Article ID 011914, 2013.
- [31] S. Xiao, S. Xiao, and F. Gräter, "Dissecting the structural determinants for the difference in mechanical stability of silk and amyloid β -sheet stacks," *Physical Chemistry Chemical Physics*, vol. 15, no. 22, pp. 8765–8771, 2013.
- [32] T. P. Knowles, A. W. Fitzpatrick, S. Meehan et al., "Role of intermolecular forces in defining material properties of protein nanofibrils," *Science*, vol. 318, no. 5858, pp. 1900–1903, 2007.
- [33] J. T. Nielsen, M. Bjerring, M. D. Jeppesen et al., "Unique identification of supramolecular structures in amyloid fibrils by solid-state NMR spectroscopy," *Angewandte Chemie—International Edition*, vol. 48, no. 12, pp. 2118–2121, 2009.
- [34] G. Yoon, M. Lee, K. Kim et al., "Morphology and mechanical properties of multi-stranded amyloid fibrils probed by atomistic and coarse-grained simulations," *Physical Biology*, vol. 12, no. 6, Article ID 066021, 2015.
- [35] J. Dong, C. E. Castro, M. C. Boyce, M. J. Lang, and S. Lindquist, "Optical trapping with high forces reveals unexpected behaviors of prion fibrils," *Nature Structural and Molecular Biology*, vol. 17, no. 12, pp. 1422–1430, 2010.
- [36] A. W. P. Fitzpatrick, S. T. Park, and A. H. Zewail, "Exceptional rigidity and biomechanics of amyloid revealed by 4D electron microscopy," *Proceedings of the National Academy of Sciences of the United States of America*, vol. 110, no. 27, pp. 10976–10981, 2013.
- [37] M. F. M. Engel, L. Khemtémourian, C. C. Kleijer et al., "Membrane damage by human islet amyloid polypeptide through fibril growth at the membrane," *Proceedings of the National Academy of Sciences of the United States of America*, vol. 105, no. 16, pp. 6033–6038, 2008.

- [38] S. E. Cross, Y.-S. Jin, J. Rao, and J. K. Gimzewski, "Nanomechanical analysis of cells from cancer patients," *Nature Nanotechnology*, vol. 2, no. 12, pp. 780–783, 2007.
- [39] M. Tanaka, S. R. Collins, B. H. Toyama, and J. S. Weissman, "The physical basis of how prion conformations determine strain phenotypes," *Nature*, vol. 442, no. 7102, pp. 585–589, 2006.
- [40] M. J. Buehler, S. Keten, and T. Ackbarow, "Theoretical and computational hierarchical nanomechanics of protein materials: deformation and fracture," *Progress in Materials Science*, vol. 53, no. 8, pp. 1101–1241, 2008.
- [41] K. Eom, G. Yoon, J.-L. Kim, and S. Na, "Coarse-grained elastic models of protein structures for understanding their mechanics and dynamics," *Journal of Computational and Theoretical Nanoscience*, vol. 7, no. 7, pp. 1210–1226, 2010.
- [42] K. Eom, *Simulations in Nanobiotechnology*, CRC Press: Taylor & Francis Group, Boca Raton, Fla, USA, 2011.
- [43] M. Sotomayor and K. Schulten, "Single-molecule experiments in vitro and in silico," *Science*, vol. 316, no. 5828, pp. 1144–1148, 2007.
- [44] M. J. Buehler and S. Keten, "Colloquium: failure of molecules, bones, and the Earth itself," *Reviews of Modern Physics*, vol. 82, no. 2, pp. 1459–1487, 2010.
- [45] J. Adamcik and R. Mezzenga, "Study of amyloid fibrils via atomic force microscopy," *Current Opinion in Colloid and Interface Science*, vol. 17, no. 6, pp. 369–376, 2012.
- [46] K. F. Freed, "Functional integrals and polymer statistics," *Advances in Chemical Physics*, vol. 22, pp. 1–128, 1972.
- [47] H. Yamakawa and M. Fujii, "Wormlike chains near the rod limit: path integral in the WKB approximation," *The Journal of Chemical Physics*, vol. 59, no. 12, pp. 6641–6644, 1973.
- [48] S. Kumar and M. S. Li, "Biomolecules under mechanical force," *Physics Reports*, vol. 486, no. 1-2, pp. 1–74, 2010.
- [49] T. Strick, J.-F. Allemand, V. Croquette, and D. Bensimon, "Twisting and stretching single DNA molecules," *Progress in Biophysics and Molecular Biology*, vol. 74, no. 1-2, pp. 115–140, 2000.
- [50] A. K. Mazur, "Wormlike chain theory and bending of short DNA," *Physical Review Letters*, vol. 98, no. 21, Article ID 218102, 2007.
- [51] C. Rivetti, M. Guthold, and C. Bustamante, "Scanning force microscopy of DNA deposited onto mica: equilibration versus kinetic trapping studied by statistical polymer chain analysis," *Journal of Molecular Biology*, vol. 264, no. 5, pp. 919–932, 1996.
- [52] F. Pampaloni, G. Lattanzi, A. Jonáš, T. Surrey, E. Frey, and E.-L. Florin, "Thermal fluctuations of grafted microtubules provide evidence of a length-dependent persistence length," *Proceedings of the National Academy of Sciences of the United States of America*, vol. 103, no. 27, pp. 10248–10253, 2006.
- [53] G. Voth, *Coarse-Graining of Condensed Phase and Biomolecular Systems*, CRC Press, 2008.
- [54] A. J. Rader, "Coarse-grained models: getting more with less," *Current Opinion in Pharmacology*, vol. 10, no. 6, pp. 753–759, 2010.
- [55] P. Sherwood, B. R. Brooks, and M. S. P. Sansom, "Multiscale methods for macromolecular simulations," *Current Opinion in Structural Biology*, vol. 18, no. 5, pp. 630–640, 2008.
- [56] C. Hyeon and D. Thirumalai, "Capturing the essence of folding and functions of biomolecules using coarse-grained models," *Nature Communications*, vol. 2, article 487, 2011.
- [57] M. M. Tirion, "Large amplitude elastic motions in proteins from a single-parameter, atomic analysis," *Physical Review Letters*, vol. 77, no. 9, pp. 1905–1908, 1996.
- [58] A. R. Atilgan, S. R. Durell, R. L. Jernigan, M. C. Demirel, O. Keskin, and I. Bahar, "Anisotropy of fluctuation dynamics of proteins with an elastic network model," *Biophysical Journal*, vol. 80, no. 1, pp. 505–515, 2001.
- [59] I. Bahar and A. J. Rader, "Coarse-grained normal mode analysis in structural biology," *Current Opinion in Structural Biology*, vol. 15, no. 5, pp. 586–592, 2005.
- [60] I. Bahar, C. Chennubhotla, and D. Tobi, "Intrinsic dynamics of enzymes in the unbound state and relation to allosteric regulation," *Current Opinion in Structural Biology*, vol. 17, no. 6, pp. 633–640, 2007.
- [61] F. Tama and C. L. Brooks III, "Symmetry, form, and shape: guiding principles for robustness in macromolecular machines," *Annual Review of Biophysics and Biomolecular Structure*, vol. 35, pp. 115–133, 2006.
- [62] K. Eom, S.-C. Baek, J.-H. Ahn, and S. Na, "Coarse-graining of protein structures for the normal mode studies," *Journal of Computational Chemistry*, vol. 28, no. 8, pp. 1400–1410, 2007.
- [63] H. Jang, S. Na, and K. Eom, "Multiscale network model for large protein dynamics," *The Journal of Chemical Physics*, vol. 131, no. 24, Article ID 245106, 2009.
- [64] C. Atilgan, O. B. Okan, and A. R. Atilgan, "Network-based models as tools hinting at nonevident protein functionality," *Annual Review of Biophysics*, vol. 41, no. 1, pp. 205–225, 2012.
- [65] L. Meirovitch, *Analytical Methods in Vibrations*, Macmillan, New York, NY, USA, 1967.
- [66] J. M. Gere, *Mechanics of Materials*, Thomson Learning, 6th edition, 2003.
- [67] A. Kis, S. Kasas, B. Babić et al., "Nanomechanics of Microtubules," *Physical Review Letters*, vol. 89, no. 24, 2002.
- [68] S. P. Timoshenko, "LXVI. On the correction for shear of the differential equation for transverse vibrations of prismatic bars," *Philosophical Magazine Series 6*, vol. 41, no. 245, pp. 744–746, 1921.
- [69] K. C. Neuman, T. Lionnet, and J.-F. Allemand, "Single-molecule micromanipulation techniques," *Annual Review of Materials Research*, vol. 37, pp. 33–67, 2007.
- [70] D. P. Allison, P. Hinterdorfer, and W. H. Han, "Biomolecular force measurements and the atomic force microscope," *Current Opinion in Biotechnology*, vol. 13, no. 1, pp. 47–51, 2002.
- [71] E. M. Puchner and H. E. Gaub, "Force and function: probing proteins with AFM-based force spectroscopy," *Current Opinion in Structural Biology*, vol. 19, no. 5, pp. 605–614, 2009.
- [72] K. Eom, J. Yang, J. Park et al., "Experimental and computational characterization of biological liquid crystals: a review of single-molecule bioassays," *International Journal of Molecular Sciences*, vol. 10, no. 9, pp. 4009–4032, 2009.
- [73] I. Usov and R. Mezzenga, "Correlation between nanomechanics and polymorphic conformations in amyloid fibrils," *ACS Nano*, vol. 8, no. 11, pp. 11035–11041, 2014.
- [74] M. R. Sawaya, S. Sambashivan, R. Nelson et al., "Atomic structures of amyloid cross- β spines reveal varied steric zippers," *Nature*, vol. 447, no. 7143, pp. 453–457, 2007.
- [75] H. J. Chang, I. Baek, M. Lee, and S. Na, "Influence of aromatic residues on the material characteristics of A β amyloid protofibrils at the atomic scale," *ChemPhysChem*, vol. 16, no. 11, pp. 2403–2414, 2015.
- [76] K. Eom, "Mechanical characterization of protein materials," in *Simulations in Nanobiotechnology*, K. Eom, Ed., chapter 7, pp. 221–270, CRC Press, Boca Raton, Fla, USA, 2013.

- [77] M. Lee, H. J. Chang, D. Kim et al., "Relationship between structural composition and material properties of polymorphic hIAPP fibrils," *Biophysical Chemistry*, vol. 199, pp. 1–8, 2015.
- [78] B. Choi, S. W. Lee, and K. Eom, "Nanomechanical behaviors and properties of amyloid fibrils," *Multiscale and Multiphysics Mechanics*, vol. 1, no. 1, pp. 53–64, 2016.
- [79] J. I. Kim, M. Lee, I. Baek, G. Yoon, and S. Na, "The mechanical response of hIAPP nanowires based on different bending direction simulations," *Physical Chemistry Chemical Physics*, vol. 16, no. 34, pp. 18493–18500, 2014.
- [80] G. Lee, W. Lee, H. Lee et al., "Mapping the surface charge distribution of amyloid fibril," *Applied Physics Letters*, vol. 101, no. 4, Article ID 043703, 2012.
- [81] N. Mizuno, U. Baxa, and A. C. Steven, "Structural dependence of HET-s amyloid fibril infectivity assessed by cryoelectron microscopy," *Proceedings of the National Academy of Sciences of the United States of America*, vol. 108, no. 8, pp. 3252–3257, 2011.
- [82] M. Kawahara, M. Kato, and Y. Kuroda, "Effects of aluminum on the neurotoxicity of primary cultured neurons and on the aggregation of β -amyloid protein," *Brain Research Bulletin*, vol. 55, no. 2, pp. 211–217, 2001.
- [83] D. Drago, M. Folin, S. Baiguera, G. Tognon, F. Ricchelli, and P. Zatta, "Comparative effects of A β (1–42)-Al complex from rat and human amyloid on rat endothelial cell cultures," *Journal of Alzheimer's Disease*, vol. 11, no. 1, pp. 33–44, 2007.
- [84] P. Zatta, *Metal Ions and Neurodegenerative Disorders*, World Scientific, Singapore, 2003.
- [85] S. Parthasarathy, F. Long, Y. Miller et al., "Molecular-level examination of Cu²⁺ binding structure for amyloid fibrils of 40-residue Alzheimer's β by solid-state NMR spectroscopy," *Journal of the American Chemical Society*, vol. 133, no. 10, pp. 3390–3400, 2011.
- [86] A. Abelein, A. Gräslund, and J. Danielsson, "Zinc as chaperone-mimicking agent for retardation of amyloid β peptide fibril formation," *Proceedings of the National Academy of Sciences of the United States of America*, vol. 112, no. 17, pp. 5407–5412, 2015.

Research Article

Lipid Reconstitution-Enabled Formation of Gold Nanoparticle Clusters for Mimetic Cellular Membrane

Jiyoung Nam,¹ Yong-Tae Kim,¹ Aeyeon Kang,² Kook-Han Kim,¹ KyoRee Lee,³
Wan Soo Yun,² and Yong Ho Kim^{1,2}

¹SKKU Advanced Institute of Nanotechnology, Sungkyunkwan University, Suwon 16419, Republic of Korea

²Department of Chemistry, Sungkyunkwan University, Suwon 16419, Republic of Korea

³Interdisciplinary Course of Physics and Chemistry, Sungkyunkwan University, Suwon 16419, Republic of Korea

Correspondence should be addressed to Wan Soo Yun; wsyun87@skku.edu and Yong Ho Kim; yhkim94@skku.edu

Received 2 March 2016; Accepted 28 April 2016

Academic Editor: Yaling Liu

Copyright © 2016 Jiyoung Nam et al. This is an open access article distributed under the Creative Commons Attribution License, which permits unrestricted use, distribution, and reproduction in any medium, provided the original work is properly cited.

Gold nanoparticles (AuNPs) encapsulated within reconstituted phospholipid bilayers have been utilized in various bioapplications due to their improved cellular uptake without compromising their advantages. Studies have proved that clustering AuNPs can enhance the efficacy of theranostic effects, but controllable aggregation or oligomerization of AuNPs within lipid membranes is still challenging. Here, we successfully demonstrate the formation of gold nanoparticle clusters (AuCLs), supported by reconstituted phospholipid bilayers with appropriate sizes for facilitating cellular uptake. Modulation of the lipid membrane curvatures influences not only the stability of the oligomeric state of the AuCLs, but also the rate of cellular uptake. Dynamic light scattering (DLS) data showed that 1-palmitoyl-2-oleoyl-sn-glycero-3-phosphoethanolamine (POPE), with its relatively small head group, is crucial for establishing an effective membrane curvature to encapsulate the AuCLs. The construction of phospholipid bilayers surrounding AuCLs was confirmed by analyzing the secondary structure of M2 proteins incorporated in the lipid membrane surrounding the AuCLs. When AuCLs were incubated with cells, accumulated clusters were found inside the cells without the lipids being removed or exchanged with the cellular membrane. We expect that our approach of clustering gold nanoparticles within lipid membranes can be further developed to design a versatile nanoplatform.

1. Introduction

Gold nanoparticles (AuNPs) have been widely studied in the field of biomedicine for a number of years because of their advantages in biocompatibility and distinguished photothermal properties [1–5]. Recent progress in the synthesis of AuNPs has allowed for precise control of their optical properties, which has motivated the development of multifunctional theranostic nanocomplexes [6–8]. Several studies have shown that the plasmonic effect of nanoparticles is intensified when the distance between particles is reduced, and thereby the surface-enhanced Raman scattering (SERS) signal is significantly amplified within the interparticle region [9–11]. However, the fine-tuning of surface association with functionality and aggregation control of gold nanoparticles toward developing the ultrasensitive biosensors or noninvasive bimodal detection of target diseases are still daunting

challenges [11, 12]. Inspired by biological membranes, solid-supported lipid assembly has been widely investigated to provide artificial lipid layers for studying membrane-associated biological phenomena [13, 14]. Unlike synthetic micelle or liposomes, lipids reconstituted on solids possess structural stability that enables prolonged experiments even for *in vivo* studies [15]. Liposomes prepared from phospholipids and phospholipid mimics have also been used to deposit various nanoparticles, to enhance biocompatibility and delivery efficiency [16, 17]. For instance, phospholipid-encapsulated quantum dots were used for *in vitro* and *in vivo* imaging with reduced toxicity [18], and mesoporous silica nanoparticles within phospholipid envelope were used as drug cargo for cancer treatment [19]. Phospholipid-encapsulated AuNPs have been highlighted as theranostic agents because their lipid coating can provide a platform to design the nanoparticle to target certain molecules within cells while retaining

the benefits of gold nanoparticles [20–22]. Several methods have been proposed to cluster lipid-coated AuNPs to enhance their therapeutic effect, but the addition of aggregation inducers or chemical modification of lipids was necessary to achieve this aggregation.

In this work, we demonstrate the construction of gold nanoparticle clusters (AuCLs) solely driven by the self-assembly of a synthetic phospholipid membrane, which can possibly be used for multifunctional drug cargo through cellular internalization. The synthesis of AuCLs was followed by two steps: (1) three different kinds of synthetic phospholipids, 1-palmitoyl-2-oleoyl-sn-glycero-3-phosphocholine (POPC), 1-palmitoyl-2-oleoyl-sn-glycero-3-phospho-L-serine (POPS), and 1-palmitoyl-2-oleoyl-sn-glycero-3-phosphoethanolamine (POPE), were mixed in a molar ratio of 7:1:2, respectively, to create uniformly sized small unilamellar vesicles (SUV); and (2) incubating SUV with 20 nm AuNPs allowed the reconstitution of phospholipids on the surface of the particles that drive the formation of AuCLs. The presence of lipid layers was confirmed with transmission electron microscopy (TEM), UV-vis spectrometer, and dynamic light scattering (DLS). We analyzed the secondary structure of the M2 protein, a membrane protein from the influenza A virus, to verify the presence of the lipid layer, and this result confirmed that the phospholipids are assembled in bilayers on the surfaces of AuCLs. Furthermore, when cells were treated with AuCLs, hundreds of particles found inside the cells proved the ability of cellular uptake. Overall, this work demonstrates a facile method to cluster nanoparticles without chemical modification and the possibility of developing nanocarriers of various sizes that can be used as nanobiomedicine.

2. Materials and Methods

2.1. Materials. 1-Palmitoyl-2-oleoyl-sn-glycero-3-phosphocholine (POPC), 1-palmitoyl-2-oleoyl-sn-glycero-3-phospho-L-serine (sodium salt) (POPS), 1-palmitoyl-2-oleoyl-sn-glycero-3-phosphoethanolamine (POPE), and L- α -phosphatidylethanolamine-N-(lissamine rhodamine B sulfonyl) were obtained from Avanti Polar Lipids, Inc. (Alabaster, AL, USA). A solution of 20 nm gold nanoparticles (6×10^{12} particles per milliliter, stabilized suspension in citrate buffer) was purchased from Sigma-Aldrich (Steinheim, Germany). All solutions were prepared using ultrapure water, obtained using a Millipore Milli-Q water purification system (Darmstadt, Germany).

2.2. Synthesis of Phospholipid-Coated Gold Nanoparticles. For the preparation of liposomes, lipids of POPC, POPS, and POPE with the molar ratio of 7:1:2 were prepared in chloroform and transferred into a small glass vial. Chloroform was slowly evaporated with a gentle stream of nitrogen gas in order to form a thin film of lipid multilayers on the bottom of the glass vial. After lyophilizing for 2 days, distilled water was slowly added until it reached the desired volume, and the solution was sonicated in order to produce homogeneous uniformly sized small unilamellar vesicles (SUV). The final concentration of lipids was 5 mM. The solution was centrifuged at 9300 rcf for 10 min, and the supernatant, kept in ice, was used for further experiments.

Phospholipid-coated gold nanoparticles were prepared by mixing a solution of gold nanoparticles and SUV in a volume ratio of 1:9 and incubating the mixture at 4°C for 12 hours. In order to thoroughly mix the two components, an inverting motion was applied with a rotating mixer. To isolate AuCLs from the mixture of single gold nanoparticles and SUV, the sample solution was centrifuged at 12,000 rpm for 10 min, and the supernatant was removed. The precipitant was resuspended in a 1x PBS solution. The concentration of gold nanoparticles in AuCLs was measured by UV-vis spectrometer at an absorbance at 525 nm (UV-1800, Shimadzu, Columbia, MD, USA).

2.3. Particle Characterization. Transmission electron microscopy (TEM) (JEM ATM 200E, JEOL, 200 kV) and UV-vis spectrometer was used to characterize the formation of AuCLs. The size distribution of AuCLs, according to time, was measured by dynamic light scattering (DLS) (ZEN3690, Nano-ZS90, Malvern, UK).

2.4. Synthesis of M2 Protein by Solid-Phase Synthesis. Wild-type M2 protein, spanning the transmembrane helical motif, was synthesized by solid-phase synthesis adopting Fmoc chemistry on the H-Rink amide ChemMatrix® resin (0.47 mmol/g loading, PCAS BioMatrix Inc., Quebec, Canada) [23]. The amino acid sequence was SSDPLVVAASI-IGILHLILWILDRL. The product was cleaved from the resin with a cleavage cocktail solution containing 95:2.5:2.5 of trifluoroacetic acid (TFA):triisopropylsilane (TIS):deionized water, in a volume ratio, for 2 hours. Resin was removed by filtration, and the remaining solution was vaporized under nitrogen gas. Purification by reverse phase high-performance liquid chromatography (HPLC, Quaternary Gradient Module 2545, Waters) using a Vydac C4 column employed a linear gradient of buffer A (99.9% H₂O and 0.1% TFA) and buffer B (90% acetonitrile, 9.9% H₂O, and 0.1% TFA). The molecular mass of M2 was confirmed by matrix-assisted laser desorption/ionization-time of flight (MALDI-TOF) mass spectroscopy (Ultraflex III, Bruker, Massachusetts, MA, USA).

2.5. Circular Dichroism (CD) Spectroscopy. To analyze the secondary structure of the M2 proton channel, the stock solution of M2 protein was prepared in a 10% (w/v) methanol solution. For lipid insertion, 200 μ M of M2 protein stock solution was added to 30 nM of AuCLs in 1x PBS and incubated for 15 min with an inverting motion. Excess M2 protein was removed by centrifugation, and the precipitant was resuspended in 1x PBS for analysis. The secondary structure of the M2 proton channel was speculated by CD spectrometer (J1500, Jasco Inc., Maryland, MD, USA). The CD spectra measurement was performed in quartz cells with 1 mm path-lengths, with the far UV light ranged from 190 nm to 260 nm.

2.6. Cellular Uptake of AuCLs (Fluorescence). Fluorescent-labeled AuCLs were prepared for optical microscopy. The lipid layer was tagged with 2 mol% of L- α -phosphatidylethanolamine-N-(lissamine rhodamine B sulfonyl), which

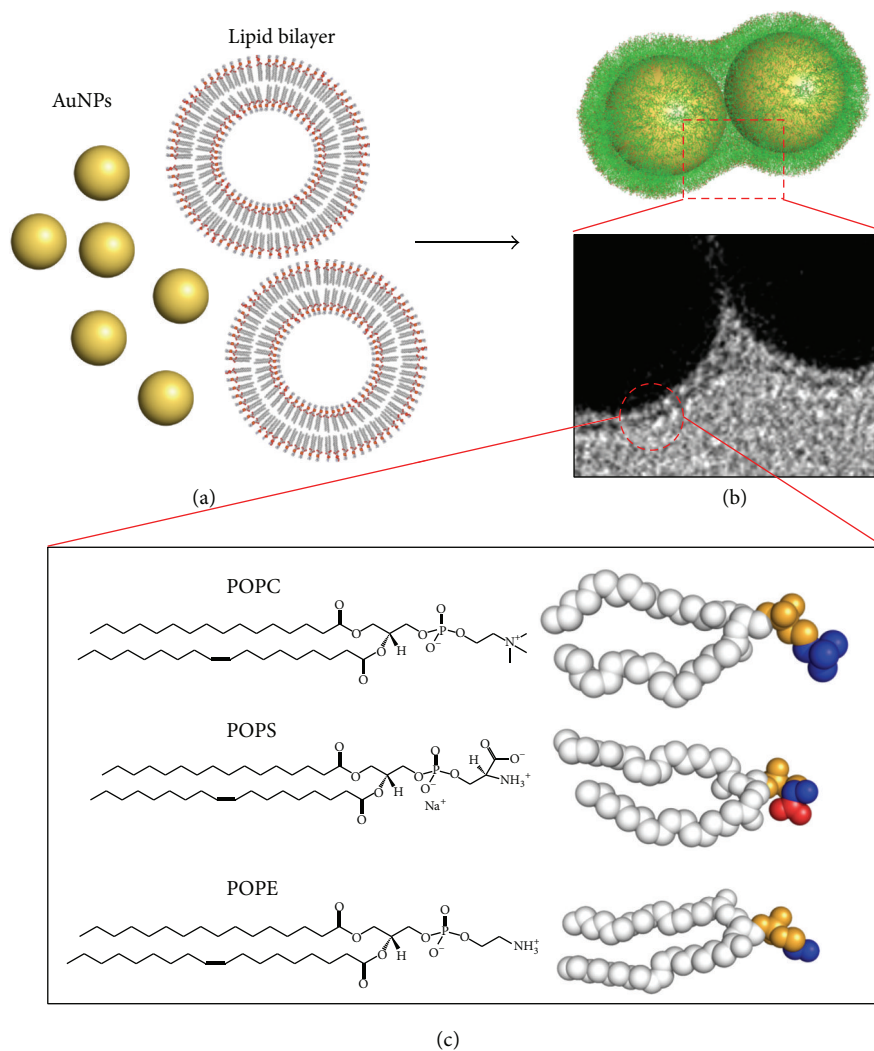


FIGURE 1: Self-assembling gold nanoparticles with synthetic phospholipid membranes driving gold nanoparticle clustering. (a) Schematic image of the formation of lipid-coated AuCLs. (b) Reconstituted lipid membrane enveloping the surface of AuCLs is visualized in a transmission electron microscopy (TEM) image, which shows surface coverage of a phospholipid membrane surrounding the AuCL dimer with a thickness of 4~6 nm. Incubation of AuNPs with SUV allows encapsulation of AuCLs. (c) Types of phospholipids used in this study: molecular structures of POPC, POPS, and POPE.

achieved excitation and emission at 560 nm and 579 nm, respectively.

SH-SY5Y neuroblastoma cells were cultured in Dulbecco's modified Eagle's medium (DMEM) with 10% fetal bovine serum and incubated at 37°C with 5% CO₂. For cellular uptake studies, 2×10^4 SH-SY5Y cells were seeded in 96-well plates, and 5 nM of fluorescence-tagged AuCLs were added in 100 μ L cell media. After 1 hour of incubation, cells were washed with fresh media and placed on the stand of the microscope (TCS SP8, Leica Microsystems, Germany) for imaging.

3. Results and Discussion

3.1. Preparation and Characterization of AuCLs. The AuCLs, illustrated in Figure 1, were prepared by reconstituting phospholipids on the surface of gold nanoparticles. Phospholipids

are the most abundant components in cellular membranes and consist of two parts: a hydrophilic head group and hydrophobic alkyl chains [24]. The amphiphilic property of phospholipids leads the molecules to self-assemble into organized structures and the size and shape of the vesicles are highly dependent on the size of head groups and length of side chains [25, 26]. We utilized three different phospholipid components, including POPC, POPS, and POPE, in a molar ratio of 7:1:2, for formulating uniformly sized SUV. Upon the incubation of citrate-capped AuNPs with SUV, citrates were exchanged with phospholipids and a thin layer of phospholipid membrane was reconstructed on AuNPs.

To confirm the formation of clusters, TEM images of AuCLs were taken (Figure 2(a)). The nanoparticles appeared to be clustered as dimers, trimers, and tetramers, and a few were aggregated in higher numbers. Some particles were found to exist as monomers, but we assume that

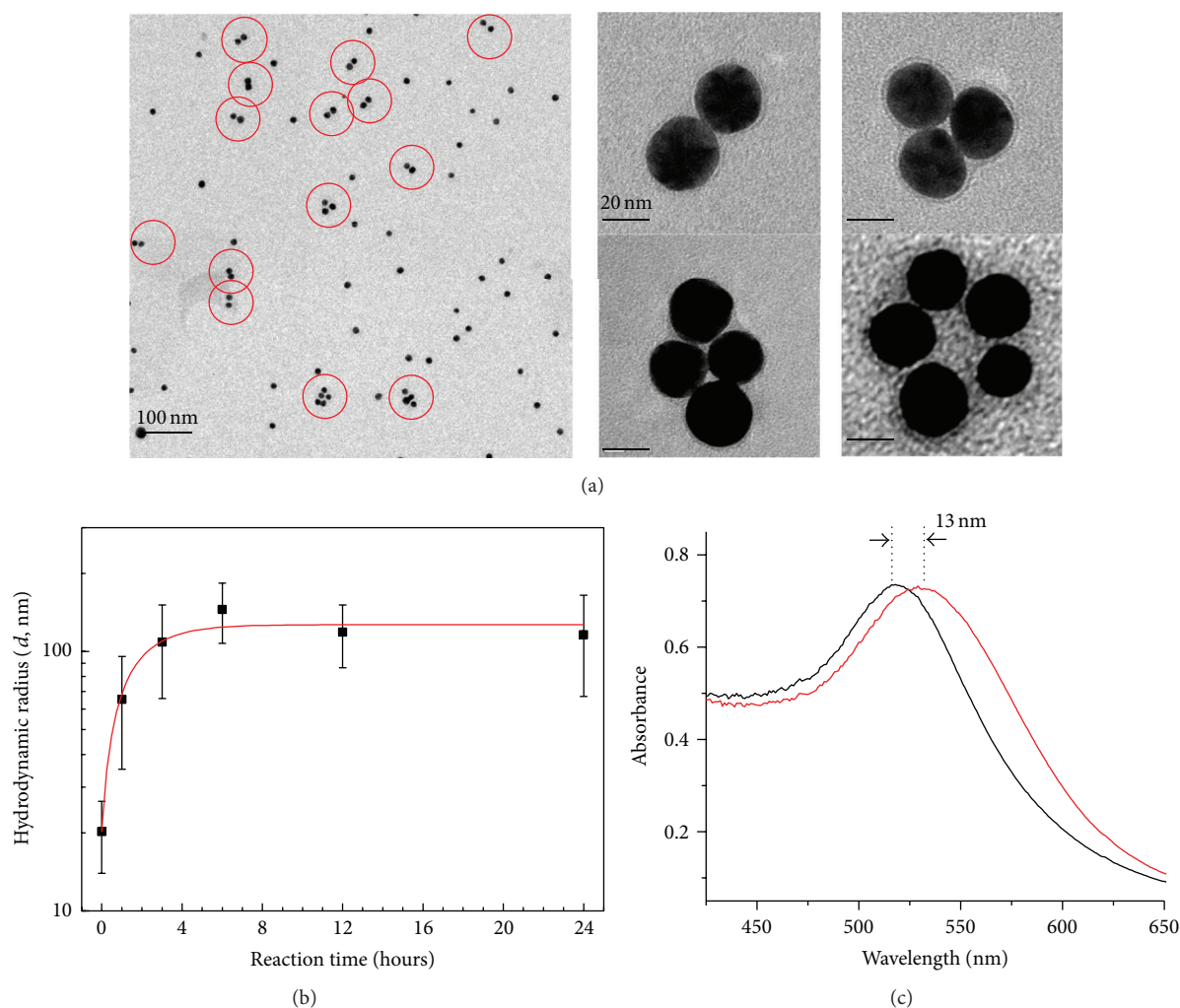


FIGURE 2: Characterization of synthesized AuCLs. (a) TEM image of AuCLs, in low resolution (left) and high resolution (right). Oligomeric states of AuCLs were indicated by red circles. High-resolution TEM images provide direct evidence for the presence of lipid layers enveloping nanoparticle clusters. (b) DLS data for AuCLs as a function of time. Hydrodynamic radius of AuCLs increases until the average size reaches 100 nm and is sustained for at least 24 hours. (c) UV-vis spectra of AuNPs (black) and AuCLs (red).

the individual particles would have clustered as well if more incubation time had been allowed. High-resolution TEM images at low accelerating voltage in an electron beam, to increase the contrast of lipid compartments, provided direct evidence of the presence of lipid layers surrounding nanoparticle clusters. DLS was used to observe kinetic phenomena of the clustering process and to examine the stability of AuCLs (Figure 2(b)). The hydrodynamic radius of AuCLs was significantly increased for 4 hours and saturated when the average size reached 100 nm. The average size of clusters was sustained for 24 hours, indicating that the lipid layer inhibits uncontrolled aggregation of AuNPs. UV-vis spectra revealed that phospholipid-supported AuCLs caused a slight red shift in a maximum absorbance peak, because of plasmonic coupling in the interparticular regions of AuCLs (Figure 2(c)) [27].

The stiffness and curvature of membranes are highly dependent on their lipid compositions, because lipids having different shapes or charges influence the interaction between

each component [26, 28]. To validate the effect of lipid composition on clustering nanoparticles, lipid vesicles comprising two types of phospholipids, POPC and POPS, were prepared and incubated with nanoparticles. As Figure 3 shows, liposomes made up of POPC, POPS, and POPE clustered nanoparticles well, while the liposomes prepared without POPE failed to generate oligomeric states of nanoparticles. It is assumed that the relatively small head group of POPE stabilizes the stiff lipid curvature on the surfaces of AuCLs and is thus likely to generate tighter membranes on the clusters.

3.2. Incorporation of M2 Proton Channel and Circular Dichroism (CD) Spectroscopy for Its Secondary Structure Analysis. To verify the formation of lipid bilayers, M2 proteins were incorporated into the AuCLs and the secondary structure of the protein was analyzed (Figure 4). M2 protein is one of the viral proton channels in the membrane of the influenza A virus [23]. It is known to have a tetrameric coiled-coil structure in

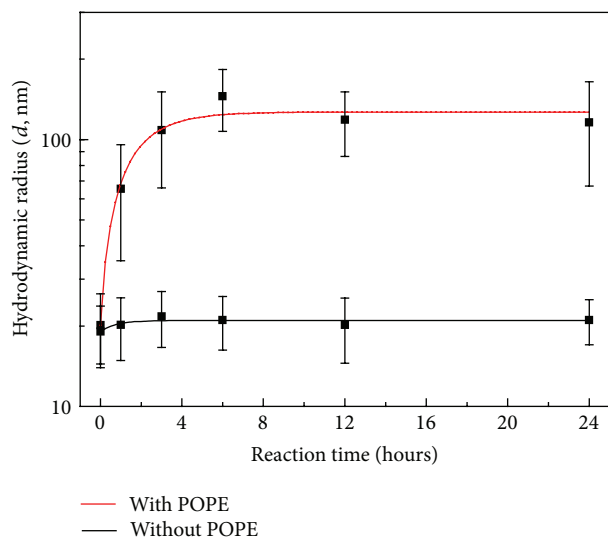
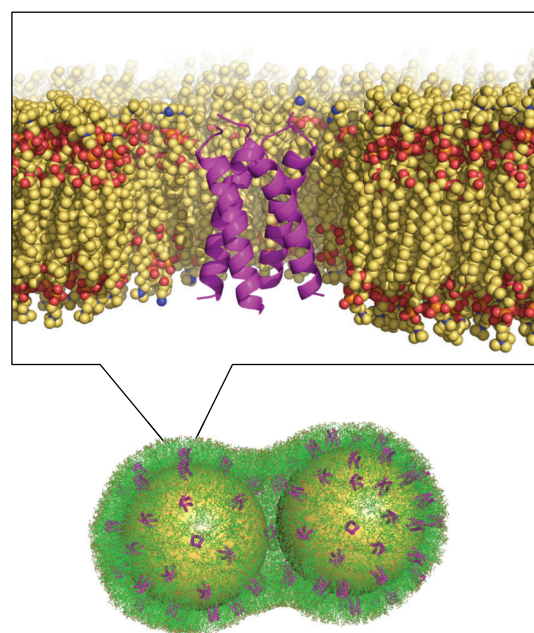


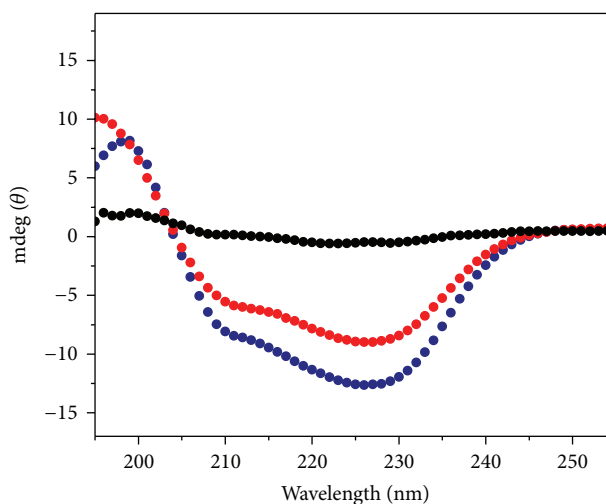
FIGURE 3: Hydrodynamic radius of AuCLs with POPC, POPS, and POPE in a molar ratio of 7 : 1 : 2 (red) or POPC and POPS in a molar ratio of 9 : 1, respectively (black). The result indicates that POPE is necessary to construct stable lipid curvature on nanoparticles.

natural lipid bilayer environments, while having random coiling in nonmembrane environments [29, 30]. We anticipated that M2 proteins would exhibit their inherent α -helical conformations when incorporated into the lipid layer of AuCLs and would ultimately prove that the phospholipids are assembled into a bilayer (Figure 4(a)). The CD spectra of M2 proteins incubated with AuCLs exhibited strong negative absorption at wavelengths of 208 nm and 222 nm, consistent with the spectrum of a typical α -helical conformation (Figure 4(b)). In order to eliminate the absorbance by the excess M2 protein in solution, unbound M2 proteins were separated from the AuCLs by centrifugation with a PBS solution. Although the intensity of the peaks decreased, the CD spectrum of the resuspended AuCLs clearly showed the same α -helical propensity of fully folded α -helices of M2 protein in the literature. The result confirmed that the reconstituted lipid membrane on AuCLs provides a folding environment for M2 proteins by acting as a mimetic of cellular membranes. For control experiments, M2 proteins were incubated with citrate-capped monodispersed AuNPs as a negative control. The mixture did not generate any appreciable absorbance peak in the wavelength range from 190 nm to 260 nm after same centrifugation process was applied. Overall, these results provide the possibility of expanding the use of AuCLs into therapeutic purposes by conjugating the lipid surface with functional molecules, or targeting cell membrane proteins.

3.3. Cellular Uptake of AuCLs. We next investigated cellular internalization of AuCLs. Fluorescence-tagged POPE was used to visualize AuCLs, and their average size was not changed by the fluorescence-tagging. When the fluorescence-tagged AuCLs were incubated with cells, large amount of nanoparticles was found to be internalized within a short period (Figure 5). In spite of crossing biological membrane environments, phospholipids surrounding AuCLs were not



(a)



(b)

FIGURE 4: Secondary structure analysis of incorporated M2 proton channels in the lipid layers of AuCLs. (a) Illustration of an M2 protein, having a folded structure, in a lipid bilayer environment. The M2 protein has an inherent α -helical conformation in cellular membrane environments. (b) Circular dichroism (CD) spectra of M2 proteins with citrate-capped AuNPs (black), incubated with AuCLs (blue), or after eliminating excess M2 protein in supernatant (red). Strong negative peaks appear at wavelengths of 208 nm and 222 nm, which represent an α -helix conformation.

removed nor exchanged with cellular lipids, which would result in fluorescence appearing on the peripheral cellular membrane. The mechanism of internalization is unknown

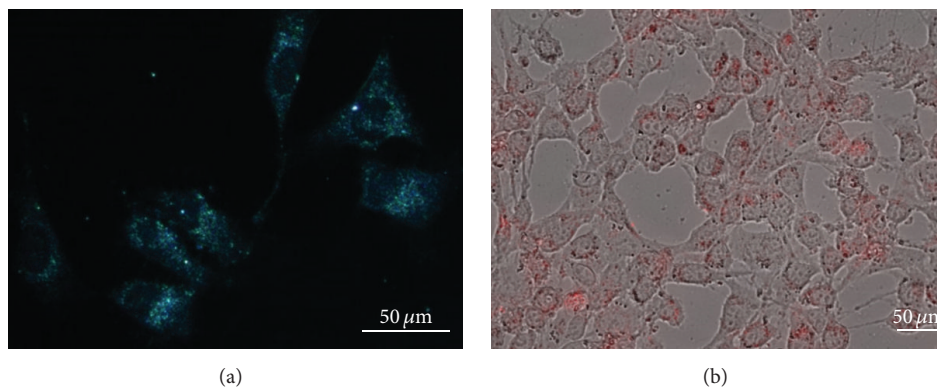


FIGURE 5: *In vitro* SH-SY5Y cellular uptake studies of AuCLs. (a) Dark field image and (b) confocal fluorescence image of SH-SY5Y neuroblastoma cells incubated with fluorescence-tagged AuCLs. 5 nM of AuCLs was directly added to cell media and incubated for 1 hour. Images were taken after washing cells with fresh cell media.

at this stage. AuCLs can enter cells either by direct internalization [31] or through the mechanism of endocytosis [32]. If AuCLs entered the cell membrane through endocytosis, it would have the sequential addition of a lipid layer [33]. Even though further study of the internalization process is necessary, the microscopic data confirms the stability of lipid assemblies on AuNPs and suggests the possibility of developing AuCLs as a drug cargo.

4. Conclusions

We have demonstrated controlled clustering of AuNPs using cellular membrane mimicking phospholipid bilayers. Three different kinds of phospholipids, POPC, POPS, and POPE, were used, and the modulation of their concentration ratio successfully encapsulated AuNPs with an average size of 100 nm that were capable of self-assembling into dimers, trimers, and tetramers. High-resolution TEM images also showed AuNPs are enveloped by lipid layers in the oligomeric state, and the stability of these states lasted at least for 24 hours. In addition, the helical folding of the M2 proton channel, when it was incubated with AuCLs, was examined by CD spectrometer, and the results showed that M2 proteins form their inherent α -helical structures in the presence of AuCLs. The results confirmed the formation of lipid bilayers on the nanoparticles and proved the possibility of functionalizing the surface of gold clusters with various, specific cell-targeting membrane proteins. Fluorescence-tagged AuCLs were also demonstrated to be capable of cellular entrance. In spite of the exposure to the cellular membrane, AuCLs retained their lipid layers while being internalized into cells. Our approach of clustering nanoparticles can be further developed to design nanoclusters with desired sizes. With the advantage of enhanced biocompatibility due to enveloping the surface of AuNPs with cell-like membranes, these AuCLs can also be used as imaging agents with enhanced spectroscopic sensitivity.

Competing Interests

The authors declare that there are no competing interests regarding the publication of this paper.

Acknowledgments

This work was supported by the National Research Foundation of Korea (NRF) under Grant NRF-2015R1A2A2A04002453 and the Basic Science Research Program through the National Research Foundation of Korea (NRF) funded by the Ministry of Education (NRF-2014R1A1A2055647 and NRF-2015M3C1A3002152).

References

- [1] P. Pericleous, M. Gazouli, A. Lyberopoulou, S. Rizos, N. Nikiteas, and E. P. Efstathopoulos, "Quantum dots hold promise for early cancer imaging and detection," *International Journal of Cancer*, vol. 131, no. 3, pp. 519–528, 2012.
- [2] P. K. Jain, X. Huang, I. H. El-Sayed, and M. A. El-Sayed, "Noble metals on the nanoscale: optical and photothermal properties and some applications in imaging, sensing, biology, and medicine," *Accounts of Chemical Research*, vol. 41, no. 12, pp. 1578–1586, 2008.
- [3] D. Pissuwan, S. M. Valenzuela, and M. B. Cortie, "Therapeutic possibilities of plasmonically heated gold nanoparticles," *Trends in Biotechnology*, vol. 24, no. 2, pp. 62–67, 2006.
- [4] K. Saha, S. S. Agasti, C. Kim, X. Li, and V. M. Rotello, "Gold nanoparticles in chemical and biological sensing," *Chemical Reviews*, vol. 112, no. 5, pp. 2739–2779, 2012.
- [5] C. J. Murphy, A. M. Gole, J. W. Stone et al., "Gold nanoparticles in biology: beyond toxicity to cellular imaging," *Accounts of Chemical Research*, vol. 41, no. 12, pp. 1721–1730, 2008.
- [6] S. Kang, S. H. Bhang, S. Hwang et al., "Mesenchymal stem cells aggregate and deliver gold nanoparticles to tumors for photothermal therapy," *ACS Nano*, vol. 9, no. 10, pp. 9678–9690, 2015.

- [7] L. R. Hirsch, R. J. Stafford, J. A. Bankson et al., "Nanoshell-mediated near-infrared thermal therapy of tumors under magnetic resonance guidance," *Proceedings of the National Academy of Sciences of the United States of America*, vol. 100, no. 23, pp. 13549–13554, 2003.
- [8] X. Qian, X.-H. Peng, D. O. Ansari et al., "In vivo tumor targeting and spectroscopic detection with surface-enhanced Raman nanoparticle tags," *Nature Biotechnology*, vol. 26, no. 1, pp. 83–90, 2008.
- [9] D. Paria, K. Roy, H. J. Singh et al., "Ultrahigh field enhancement and photoresponse in atomically separated arrays of plasmonic dimers," *Advanced Materials*, vol. 27, no. 10, pp. 1751–1758, 2015.
- [10] B. Khlebtsov, V. Zharov, A. Melnikov, V. Tuchin, and N. Khlebtsov, "Optical amplification of photothermal therapy with gold nanoparticles and nanoclusters," *Nanotechnology*, vol. 17, no. 20, p. 5167, 2006.
- [11] U. S. Dinish, G. Balasundaram, Y.-T. Chang, and M. Olivo, "Actively targeted in vivo multiplex detection of intrinsic cancer biomarkers using biocompatible SERS nanotags," *Scientific Reports*, vol. 4, article 4075, 2014.
- [12] L.-J. Xu, C. Zong, X.-S. Zheng, P. Hu, J.-M. Feng, and B. Ren, "Label-free detection of native proteins by surface-enhanced Raman spectroscopy using iodide-modified nanoparticles," *Analytical Chemistry*, vol. 86, no. 4, pp. 2238–2245, 2014.
- [13] E. Sackmann, "Supported membranes: scientific and practical applications," *Science*, vol. 271, no. 5245, pp. 43–48, 1996.
- [14] A. Kloboucek, A. Behrisch, J. Faix, and E. Sackmann, "Adhesion-induced receptor segregation and adhesion plaque formation: a model membrane study," *Biophysical Journal*, vol. 77, no. 4, pp. 2311–2328, 1999.
- [15] M. Tanaka and E. Sackmann, "Polymer-supported membranes as models of the cell surface," *Nature*, vol. 437, no. 7059, pp. 656–663, 2005.
- [16] S. P. Moura and A. M. Carmona-Ribeiro, "Biomimetic particles: optimization of phospholipid bilayer coverage on silica and colloid stabilization," *Langmuir*, vol. 21, no. 22, pp. 10160–10164, 2005.
- [17] E. E. Ross, S.-W. Mok, and S. R. Bugni, "Assembly of lipid bilayers on silica and modified silica colloids by reconstitution of dried lipid films," *Langmuir*, vol. 27, no. 14, pp. 8634–8644, 2011.
- [18] B. Dubertret, P. Skourides, D. J. Norris, V. Noireaux, A. H. Brivanlou, and A. Libchaber, "In vivo imaging of quantum dots encapsulated in phospholipid micelles," *Science*, vol. 298, no. 5599, pp. 1759–1762, 2002.
- [19] L.-S. Wang, L.-C. Wu, S.-Y. Lu et al., "Biofunctionalized phospholipid-capped mesoporous silica nanoshuttles for targeted drug delivery: improved water suspensibility and decreased nonspecific protein binding," *ACS Nano*, vol. 4, no. 8, pp. 4371–4379, 2010.
- [20] D. B. Chithrani, M. Dunne, J. Stewart, C. Allen, and D. A. Jaffray, "Cellular uptake and transport of gold nanoparticles incorporated in a liposomal carrier," *Nanomedicine: Nanotechnology, Biology, and Medicine*, vol. 6, no. 1, pp. e161–e169, 2010.
- [21] N. Zhang, H. Chen, A.-Y. Liu et al., "Gold conjugate-based liposomes with hybrid cluster bomb structure for liver cancer therapy," *Biomaterials*, vol. 74, pp. 280–291, 2016.
- [22] M. Wang, K. Alberti, S. Sun, C. L. Arellano, and Q. Xu, "Combinatorially designed lipid-like nanoparticles for intracellular delivery of cytotoxic protein for cancer therapy," *Angewandte Chemie—International Edition*, vol. 53, no. 11, pp. 2893–2898, 2014.
- [23] A. L. Stouffer, R. Acharya, D. Salom et al., "Structural basis for the function and inhibition of an influenza virus proton channel," *Nature*, vol. 451, no. 7178, pp. 596–599, 2008.
- [24] J. A. Yang and C. J. Murphy, "Evidence for patchy lipid layers on gold nanoparticle surfaces," *Langmuir*, vol. 28, no. 12, pp. 5404–5416, 2012.
- [25] M. Antonietti and S. Förster, "Vesicles and liposomes: a self-assembly principle beyond lipids," *Advanced Materials*, vol. 15, no. 16, pp. 1323–1333, 2003.
- [26] I. R. Cooke and M. Deserno, "Coupling between lipid shape and membrane curvature," *Biophysical Journal*, vol. 91, no. 2, pp. 487–495, 2006.
- [27] J. M. Romo-Herrera, R. A. Alvarez-Puebla, and L. M. Liz-Marzán, "Controlled assembly of plasmonic colloidal nanoparticle clusters," *Nanoscale*, vol. 3, no. 4, pp. 1304–1315, 2011.
- [28] H. T. McMahon and J. L. Gallop, "Membrane curvature and mechanisms of dynamic cell membrane remodelling," *Nature*, vol. 438, no. 7068, pp. 590–596, 2005.
- [29] K. C. Duff, S. M. Kelly, N. C. Price, and J. P. Bradshaw, "The secondary structure of influenza A M2 transmembrane domain: A circular dichroism study," *FEBS Letters*, vol. 311, no. 3, pp. 256–258, 1992.
- [30] F. A. Kovacs and T. A. Cross, "Transmembrane four-helix bundle of influenza A M2 protein channel: Structural implications from helix tilt and orientation," *Biophysical Journal*, vol. 73, no. 5, pp. 2511–2517, 1997.
- [31] P. Nativo, I. A. Prior, and M. Brust, "Uptake and intracellular fate of surface-modified gold nanoparticles," *ACS Nano*, vol. 2, no. 8, pp. 1639–1644, 2008.
- [32] B. D. Chithrani and W. C. W. Chan, "Elucidating the mechanism of cellular uptake and removal of protein-coated gold nanoparticles of different sizes and shapes," *Nano Letters*, vol. 7, no. 6, pp. 1542–1550, 2007.
- [33] J. Sun, L. Zhang, J. Wang et al., "Tunable rigidity of (polymeric core)-(lipid shell) nanoparticles for regulated cellular uptake," *Advanced Materials*, vol. 27, no. 8, pp. 1402–1407, 2015.

Research Article

Effects of End-Terminal Capping on Transthyretin (105–115) Amyloid Protofibrils Using Steered Molecular Dynamics

Myeongsang Lee, Hyunsung Choi, and Sungsoo Na

Department of Mechanical Engineering, Korea University, Seoul 136-701, Republic of Korea

Correspondence should be addressed to Sungsoo Na; nass@korea.ac.kr

Received 30 December 2015; Revised 31 March 2016; Accepted 10 April 2016

Academic Editor: Zhiping Xu

Copyright © 2016 Myeongsang Lee et al. This is an open access article distributed under the Creative Commons Attribution License, which permits unrestricted use, distribution, and reproduction in any medium, provided the original work is properly cited.

Numerous degenerative diseases are associated with amyloidosis, which can be caused by amyloid proteins. These amyloid proteins are generated from misfolded and denatured amyloid monomers under physiological conditions. Changes in protonation state, pH, ionic strength, and temperature, in addition to mutations, are related to the promotion of amyloidosis. Specifically, an understanding of the mechanical characteristics of amyloid protofibrils is important, since amyloid growth proceeds by a mechanism involving cycles of fragmentation and elongation. However, there remains a lack of knowledge of amyloid structural conformations and their mechanical characteristics, particularly considering end-terminal capping effects. In the present study, we investigated the mechanical characteristics of transthyretin amyloid protein (TTR), which have been implicated in cardiovascular disease, and specifically considered the contribution of end-terminal capping effects. Using steered molecular dynamics (SMD) simulations, we report different structural behaviors between uncapped and capped TTR amyloid protofibrils. We show that end-terminal capping strengthens the structural stability and improves the mechanical properties of amyloid protofibrils. This study provides useful information concerning the structural and mechanical characteristics of TTR amyloid protofibrils, with a particular emphasis on end-terminal capping effects.

1. Introduction

Many of the major types of degenerative disease are associated with denatured and misfolded amyloid proteins [1–3]. For example, type II diabetes has been associated with human islet amyloid polypeptide (hIAPP), since hIAPP triggers beta-cell death in pancreas [4]. As for dialysis-related degenerative diseases, beta-2-microglobulin amyloid proteins are found in the joints of patients due to long-term hemodialysis treatments [5, 6]. Moreover, transthyretin (TTR) amyloid proteins can contribute to cardiovascular disease by narrowing cardiac vasculature [7, 8]. The phenomenon shared by these degenerative diseases is the deposition of amyloid proteins to normal functional cells, where they are hard to degrade under physiological conditions [9, 10].

These amyloid proteins exist in several forms such as monomers, oligomers, fibrils, and plaques. A specific understanding of oligomeric amyloid fibrils is crucial, due to their toxic characteristics [11–14]. Such toxicity was established by several experimental studies, and it the results

of amyloid toxicity were the generation of ion channels across membranes, removal of lipid layers from membranes, permeation of oligomers to membranes, and additional growth of amyloid fibrils [11]. Specifically, investigations have highlighted that the size of oligomeric protofibrils is a critical parameter, since the fragmentation and elongation mechanism is related to fibrillar size. According to Collins et al., they experimentally investigated the amyloid growth mechanism using prion protein Sup 35 via three step models (i.e., nucleation, monomer addition, and fiber fragmentation) [15]. Based on this point, fundamental computational and experimental studies on fracture phenomena of amyloid fibrils may provide mechanical insights [10, 16].

Detailed computational studies have been conducted on amyloid protofibrils, examining the polymorphic characteristics [17–21], point-mutation effects [22–24], and amyloid fibrils of differing cross-sections under physiological conditions [25–27]. Paparcone et al. have provided mechanical characterization of $A\beta$ fibrils, which are associated with Alzheimer's disease [23]. They varied the salt bridge region

and examined effects on structural stability of mutating lysine and aspartate residues for each. In similar manner, Chang et al. found *via* molecular dynamics (MD) that the effect of mutating residues depends on their being located within hydrophobic core of $A\beta$ [22]. Ndlovu et al. [28, 29] and Yoon et al. investigated the effects of polymorphic characteristics and point mutations on hIAPP using equilibrated MD and steered molecular dynamics (SMD) [19, 30]. In their studies, they investigated the effects of altering the orientation of beta-strands and the effect of mutating leucine residues to phenylalanine residues on structural conformation and mechanical characteristics. In these computation studies, structural stabilities and mechanical properties of fibrillar amyloid proteins have been reported, in order to better understand the mechanisms of fragmentation under physiological conditions.

Recently, several groups considered whether end-terminal capping or altered protonation state have an effect on the structural characteristics of amyloid fibrils associated with degenerative and neurodegenerative diseases [31–34]. For example, the effects of capping hIAPP amyloid fibrils were studied experimentally and computationally. Andreasen et al., demonstrated that different conformations and structural characteristics of hIAPP fibrils are dependent on terminal capping (i.e., N-terminal acetylation and C-terminal amidation) by a combination of transmission electron microscopy (TEM), atomic force microscopy (AFM), and MD methods [32]. Specifically, they investigated the molecular characteristics of hIAPP amyloid proteins arising from terminal capping effects *via* twisting angle between each beta-strand and the number of hydrogen bonds. Porrini et al. used MD simulations to consider the effect of different protonation states on the oligomeric characteristics of amyloidogenic peptide derived from TTR 105–115 [31]. Different structural characteristics were observed depending on the protonation state, including different beta-strand content and altered twisting angles and the root mean square deviations (RMSDs). In similar manner, Lee and Na recently investigated the structural characteristics of TTR 105–115 amyloid protofibrils by end-terminal capping effects using equilibrated MD simulation methods [35]. However, the effect of capping on mechanical characteristics of TTR amyloid protofibrils remained unstudied using SMD methods.

In this study, we report the mechanical characteristics and material properties of end-terminal capped and uncapped TTR 105–115 amyloid protofibrils, using SMD methods. During the SMD simulation, we noticed a considerably stronger reaction force from the capped fibrils than from uncapped fibrils. We also report Young's modulus of the capped TTR amyloid protofibrils, and we found a larger number of hydrogen bonds in the capped fibrils. Using our SMD simulation, we also calculated the variation in electrostatic force due to end-terminal capping.

2. Material and Methods

2.1. Computational Model Construction for the SMD Simulation. In order to investigate the mechanical characteristics

of capping effect on TTR amyloid protofibrils, we used the computational results of capped and uncapped TTR amyloid protofibrils from our previous study [35]. Basically, the atomic coordinates of TTR amyloid protofibrils contained in the protein data bank (PDB-ID: 2M5N) were used as a building block for a protofibrils [36]. Geometrical conditions for protofibrils construction were also same as those in the previous experimental studies which were revealed by Dobson's group [36–38].

From our previous study [35], autopsf plugin of VMD 1.9.1 was used to give the capping effect on TTR amyloid protofibrils, by acetylating the N-terminus and amidating the C-terminus of the modeled fibrils [39]. Equilibrium simulation of each capped and uncapped protofibril was computed using NAMD package 2.8 [40] with CHARMM27 force field. Each protofibril model was minimized over 10,000 steps *via* the conjugate-gradient method. Subsequently, protofibrils were solvated in a TIP3P water box without counter ions because TTR amyloid protofibrils carried no net charges. Additionally, a minimum border-distance of 20 Å was applied from each side of the solvent box.

The MD simulations were performed for 50 ns after the simulated models to reach local minima on the potential energy surfaces. MD simulations were equilibrated at a constant-temperature (298 K) and constant-volume condition. Equilibrated results of both uncapped and capped TTR amyloid protofibrils are confirmed through the root mean square deviation and their twist angle between each beta-strands along the fibrils axis from previous study [35]. After that, the final coordinates of capped and uncapped protofibrils were obtained to use in a steered molecular dynamics (SMD) simulation in this study. Obtained capped and uncapped TTR fibrils after equilibrated MD simulations are shown in Figure 1.

2.2. Steered Molecular Dynamics (SMD) Simulation Protocol. To analyze the different mechanical behavior between uncapped and capped TTR amyloid protofibrils, SMD simulations were performed to measure tensile properties. The same NAMD package 2.8 and CHARMM27 force field was used in the SMD simulations [40]. The constant-temperature (298 K) and constant-volume ensemble was also adopted during the SMD simulations, until fracture of the fibrils occurred. The spring constant was $7.2 \text{ kcal/mol} \cdot \text{Å}^2$, where 1 kcal/mol equates to $69.489 \text{ pN} \cdot \text{Å}$, throughout the entirety of the simulations. As shown in Figure 2, the two bottom layers were fixed, and the two top layers were pulled at several constant velocities, such as 0.001 Å/ps and 0.005 Å/ps . Reaction forces were calculated using $F(t) = K_{\text{spring}}(vt - X)$, where v is a pulling speed, t is time, and X is a displacement variable. The resulting relationship between the reaction forces and displacements for pulling rate was obtained after the SMD simulations. Initial fibril lengths and cross-sectional areas, for both capped and uncapped fibrils, were calculated by computing stress-strain relationships.

2.3. Calculating the Mechanical Characteristics and Properties of TTR Protofibrils. For the analysis of the mechanical

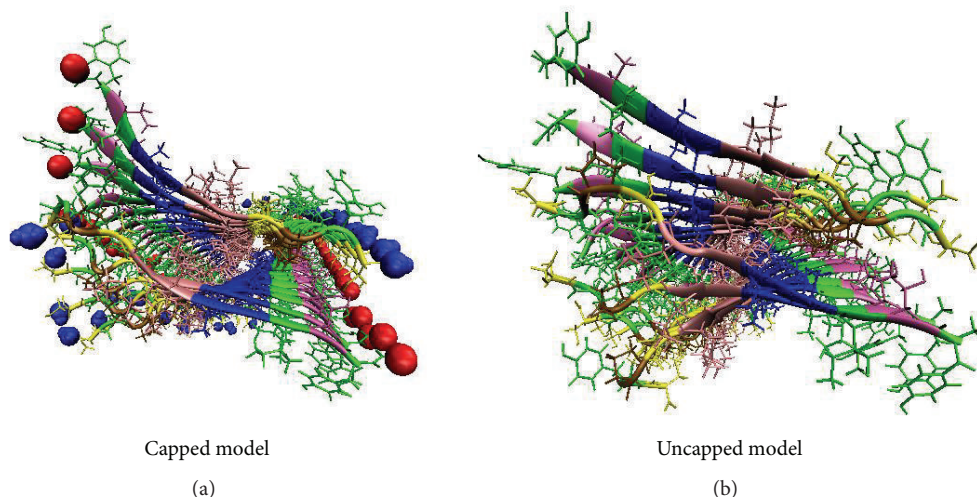


FIGURE 1: A schematic image of TTR amyloid protofibrils depends on end-terminal capping. (a) A model of a capped fibril. The capped region is represented with red and blue spheres. (b) A model of an uncapped fibril for the simulation.

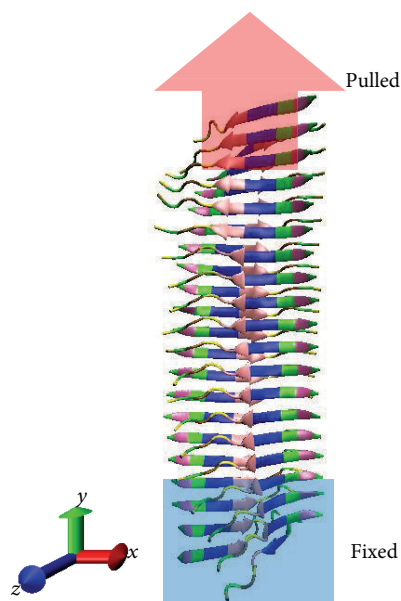


FIGURE 2: A constraint for the tensile simulations, computed by SMD simulation. The blue boxed region of TTR amyloid protofibril was fixed. The red boxed area, corresponding to the top two layers of the protofibril, was pulled along the fibril axis, which is parallel to y -axis.

characteristics of TTR amyloid protofibrils, classical beam theory was used to calculate Young's modulus for each case. The TTR protofibrils were regarded as beam models. The constitutive relation is given by Hooke's law, which represented as $\sigma_{yy} = E \cdot \varepsilon_{yy}$. Here, σ_{yy} is the stress along the fibril axis which is parallel to y -axis (Figure 1), E is Young's modulus, and ε_{yy} is the strain along to the fibril axis (i.e., z -axis). Stress could be expressed as $\sigma_{yy} = F/A$. Here, F is the calculated force during the SMD simulation, and A is

the measured cross-sectional areas, where we assumed the cross-section area of TTR amyloid protofibrils as rectangular shapes. Four alpha carbons located on the end-terminus of two beta-strands of bottom layer are regarded as edges of rectangular shape from cross-section of TTR amyloid protofibrils. Therefore, the cross-sectional area was calculated by measuring the width and height from rectangular shape. Stress was computed by calculating the tensile loading on the cross-sectional area of fibrils over time, and strain variation was obtained by dividing the change in length of a fibril during the same time by its initial length (~ 10 nm).

3. Results and Discussion

3.1. Different Fracture Behavior of TTR Amyloid Protofibrils Caused by End-Terminal Capping. Our previous study, using a 50 ns equilibrated MD simulation and principle component analysis (PCA), examined that N-terminal acetylation and C-terminal amidation of TTR amyloid protofibrils alter their structural conformations and mechanical characteristics [35]. Based on those results, we reported considerably improved structural stabilities and Young's moduli of capped TTR amyloid protofibrils. Differences in Young's modulus values were two times larger than the expected torsional modulus.

In this study, employing constant-velocity loading simulations, we showed that TTR 105–115 amyloid material strength is different, depending on end-terminal capping status. Further, in order to detect end-terminal capping effects in detail, we applied two different loading conditions (0.001 Å/ps and 0.005 Å/ps). As shown in Figures 3(a)–3(d), in both 0.001 Å/ps and 0.005 Å/ps constant-velocity loading conditions, we found higher peak forces for capped protofibrils. Under 0.001 Å/ps constant-velocity loading simulations (see Figures 3(a) and 3(b)), the first peak force events for both uncapped and capped TTR were observed around the 1 ns period. At the peak force value, however, both the rupture

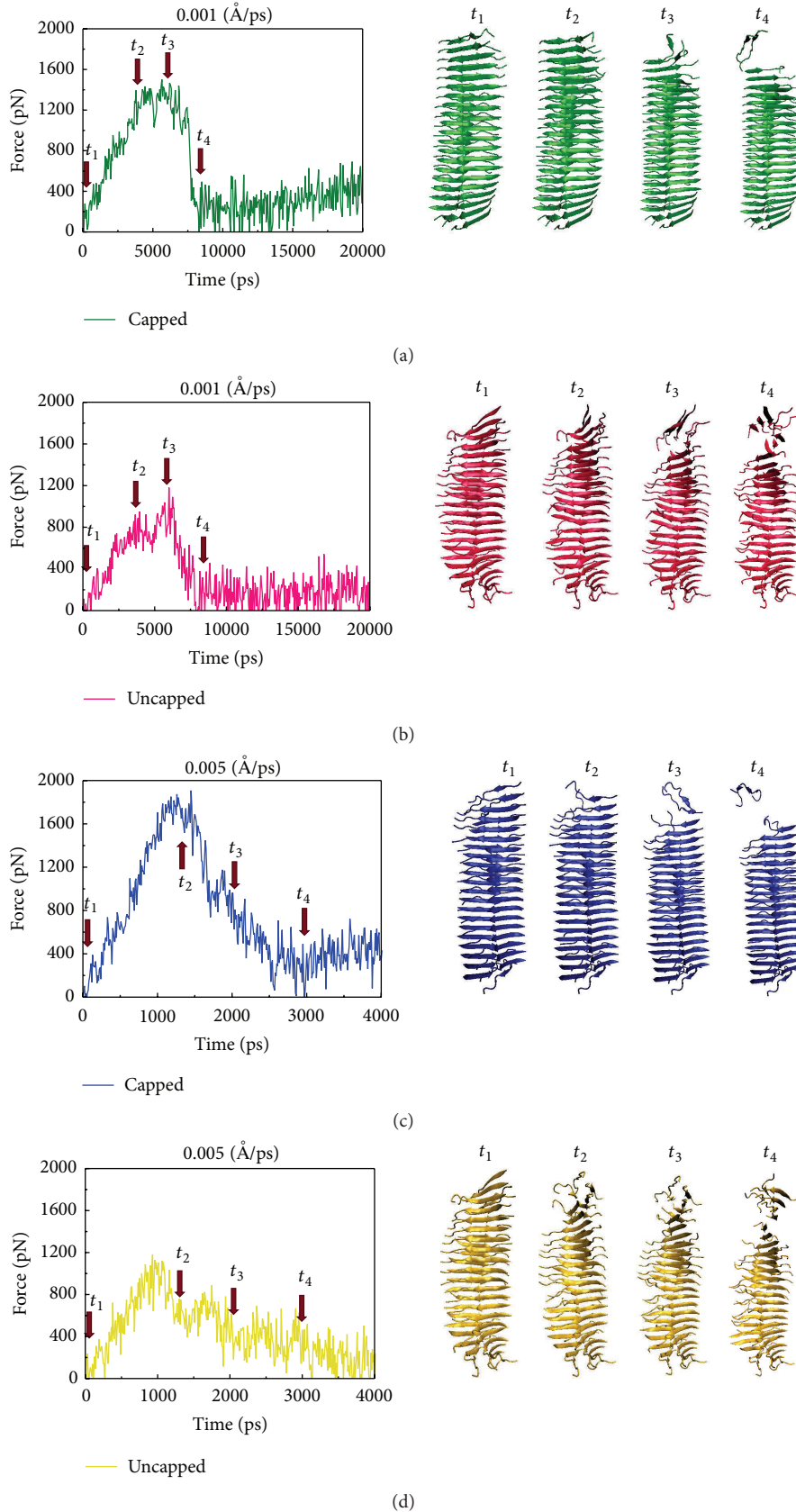


FIGURE 3: Time versus force graphs comparing different fracture features of capped and uncapped fibrils for time. Both (a) and (b) show the results of SMD simulation with a pulling rate of 0.001 \AA/ps for the capped model and the uncapped model, respectively. Panels (c) and (d) show the results for the capped model and the uncapped model, respectively, at a pulling rate of 0.005 \AA/ps . Fracture processes over time are indicated by the downward arrows, which are marked with t_1 , t_2 , t_3 , and t_4 .

force and the fracture behavior of capped and uncapped TTR protofibrils differ. During time-force analysis, the peak force for capped protofibrils was 1400 pN, while the peak force of uncapped protofibrils was 1000 pN. Different fracture behaviors were also observed in the time-force graphs and rupture trajectories. In the case of capped protofibrils, we see only one peak force value, while uncapped protofibrils display multiple peak forces during SMD simulations. These tendencies can be supported by the rupture process as shown on the right side in Figures 3(a) and 3(b). For the capped fibrils, we see that only the top layer fractured over the 5–10 ns period. However, uncapped fibrils undergo multiple fracture processes and fractured beta-strands contents during this same 5–10 ns period. Around the 3 ns period, one side of two beta-strands fractured (marked as t_2), with the other side fracturing around the 5.5 ns period (marked as t_3).

Similar findings resulted from the 0.005 Å/ps constant-loading simulations as shown in Figures 3(c) and 3(d), respectively. Due to the higher constant-loading condition (0.005 compared to 0.001 Å/ps), short fracture events were observed for both capped and uncapped protofibrils over the same time period. In addition, different fracture behavior and peak force were observed, relative to 0.001 Å/ps constant-loading simulation. Only a single peak force value was observed for capped protofibrils (marked as t_2), while multiple peak forces were observed for uncapped TTR protofibril (denoted t_2 , t_3 , and t_4). The peak force difference between the two protofibril types was 800 pN, which was similar to the value from the lower loading simulation (i.e., 0.001 Å/ps). Specifically, for the uncapped protofibrils, multiple fracture spots were revealed, while only the top layer was fractured in capped protofibrils. These different peak force results along with the different constant-velocity loading conditions could be compared to previous similar computational hIAPP fibril study by Choi et al. [41]. They found the different rupture force of hIAPP fibrils when different pulling speed was applied. These different rupture phenomena along with various pulling velocity also can be found in our study, where higher peak force was observed when faster pulling speed was applied [41].

Interestingly, end-terminal capping on TTR amyloid protofibrils did not affect the calculated peak force occurrence time, even under different loading and velocity conditions. Lee et al., who investigated the mechanical and material characteristics of polymorphic hIAPP protofibrils, reported that each polymorphic structure (i.e., APHO, AHPE, PHO, and PHE model) has a different peak force value with a different peak force occurrence time, based on their time-force analysis [17]. However, uncapped and capped TTR amyloid protofibrils only exhibited different peak force values, while sharing similar peak force occurrence times. Therefore, our simulations suggest that end-terminal capping only affects reaction force values, not peak force occurrence times.

Thus, from our analysis of the time-force profiles and fracture trajectories from 0.001 Å/ps and 0.005 Å/ps constant-loading simulations, we can see that the end-terminal capping is predicted to result in different fracture behavior, albeit over similar time periods.

3.2. Fracture Characteristics of TTR Amyloid Protofibril by the End-Terminal Capping. During constant-velocity loading simulations, we found that the different fracture behavior of TTR amyloid protofibrils with different end-terminal capping status exhibited different time-force graphs and fracture trajectory profiles. In this section, we analyzed the different material fracturing behaviors of protofibrils by investigating the number of hydrogen bonds formed and the electrostatic force as a function of time. Calculating and understanding the contributions of hydrogen bonds and “nonbonding” forces such as electrostatic and van der Waals (VdW) energies are all important for assessing the stability of amyloid fibrils. For example, a previous study addressed the role of the nonbonding forces and hydrogen bonds in altering the structural conformation and mechanical properties of A β amyloid protein by mutating the leucine residue on the 19th and 20th phenylalanine residue regions [22]. Specifically, the nonbonding forces and the number of hydrogen bonds are different in each model. Notably, replacing leucine residue on the 19th phenylalanine residue region results in a lower number of hydrogen bonds, increased VdW energies, and decreased mechanical properties. Furthermore, our previous equilibrated TTR 105–115 protofibrils handled the structural stability and their electrostatic energy effect by end terminal capping [35].

In our study (see Figure 4), a constant decrease in the number of hydrogen bonds was observed under 0.001 Å/ps and 0.005 Å/ps constant-velocity conditions. For the 0.001 Å/ps constant-velocity condition, reduction in the number of hydrogen bonds stopped around the 10 ns period, while the loss of hydrogen bonds under 0.005 Å/ps constant-velocity conditions halted around the 2 ns period. After the constant decrease in the number of hydrogen bonds reached a threshold, there were no additional decreases of hydrogen bonds, with the protofibrillar structures reaching a complete fracture. This tendency to decrease the number of hydrogen bonds is similar to that reported for several computational studies of amyloids using SMD simulations [17, 25, 35, 41–44]. When an external force is applied to amyloid proteins, the loss of hydrogen bonds or their renewal following fracture proceeds regardless of the amyloid protein species or size. For example, our previous loading simulation study on polymorphic hIAPP fibrils showed that loss of hydrogen bonds increases in step with strain [17]. In a similar manner, Solar and Buehler reported that the incremental rupture of hydrogen bonds depends on the cross-sectional area of different amyloids (i.e., A β and HET-s) [25]. Specifically, from our analysis of the number of hydrogen bonds over time in this study, we were unable to detect any difference in the material characteristics of capped or uncapped TTR protofibrils. According to Kim et al., hIAPP amyloid fibrils behave differently under constant bending simulations, depending on the structure of the polymorph tested [21]. Since polymorphism may alter material behavior, and TTR 105–115 does not have any polymorphs, end-terminal capping was only predicted to improve mechanical strength, not other material behaviors.

Further, we measured the variation in electrostatic force of uncapped and capped TTR protofibrils, from the initiation

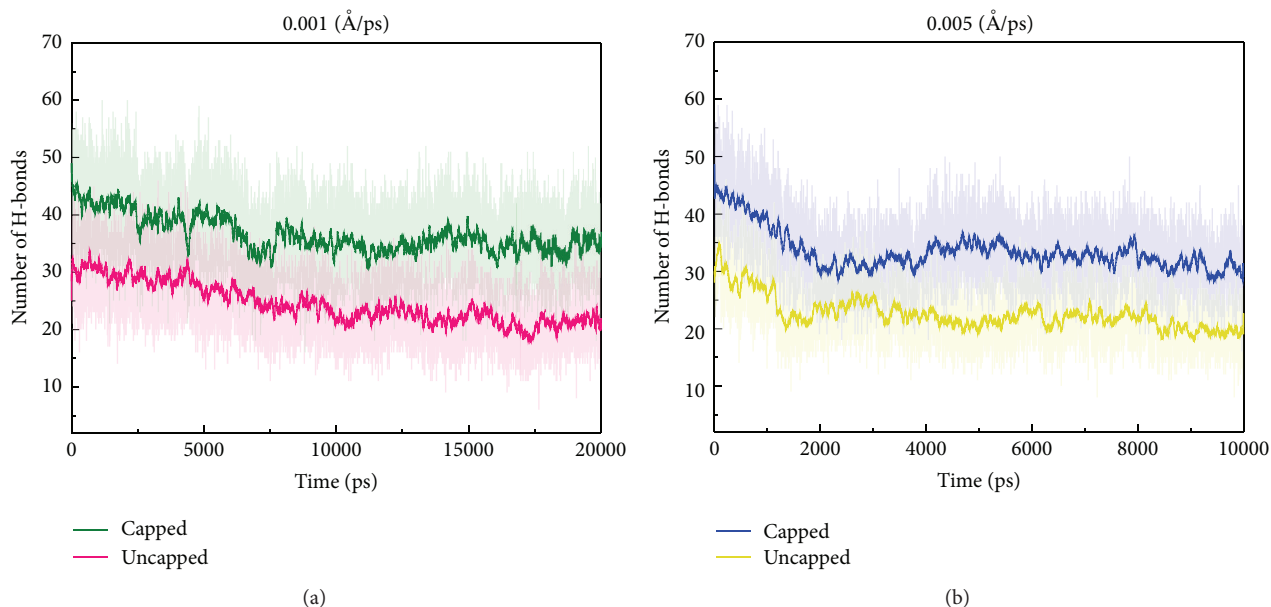


FIGURE 4: Time versus the number of hydrogen bond graphs: comparing mechanical strength differences between capped and uncapped models. (a) shows the comparison graph for the simulation performed using a velocity of 0.001 Å/ps, and (b) is the graph using a velocity of 0.005 Å/ps. To reduce the noise of hydrogen bonds per time graphs, we smoothed the data using a weighted moving average with over 100 ps.

of the loading simulation to the first peak force events. In contrast, the electrostatic forces were tracked throughout the entirety of the constant-velocity loading simulations. As shown in Figures 5(a) and 5(b), electrostatic energies increased between the initiation of loading and the occurrence of the first peak force events. These tendencies are similar to those calculated for loading simulation on A β amyloid fibrils in the study by Paparcone and Buehler. They reported that the energy density of A β amyloid fibrils increased in step with increasing strain [42]. We also calculated the stabilities of uncapped and capped TTR protofibrils *via* fluctuation of electrostatic forces. Our simulation shows that electrostatic energy fluctuations of uncapped fibrils were observed during both the 0.001 Å/ps and the 0.005 Å/ps loading conditions. In contrast, capped fibrils have fewer such fluctuations. These phenomena can be expressed as the released quantity of electrostatic energies, both uncapped and capped TTR protofibrils. Using the electrostatic energies over the whole time period, we measured the released electrostatic energy quantity of both capped and uncapped TTR protofibrils until observation of first peak force event as shown in Figure S1 in Supplementary Material available online at <http://dx.doi.org/10.1155/2016/1863065>. From the result of Figure S1, we found that the electrostatic energy release of capped TTR amyloid protofibrils was constant until first peak force event for two different loading velocity conditions, which means energy release is almost zero. However, for the uncapped TTR amyloid fibrils, energy release of electrostatic energies constantly increased and their amount was occupied up to 300 kcal/mol. Specifically, we calculated the fluctuation of electrostatic energies by measuring the standard deviation as shown in Figure 5(c), where the standard deviation of electrostatic forces is represented as error bars of average

electrostatic forces. From the figure, a large-value error bar of uncapped TTR protofibril was observed, while a small-value error bar of capped TTR protofibril was observed. Therefore, end-terminal capping on TTR protofibrils not only lowers the electrostatic forces but also strengthens and lowers the electrostatic energies fluctuations.

Our analysis of hydrogen bond prevalence, together with our analysis of electrostatic energies, supports our earlier results that end-terminal capping of TTR protofibrils effects an increase in disruptive forces, resulting in a lower fraction the beta-strands contents compared to uncapped protofibrils.

3.3. Material Properties of Capped and Uncapped TTR Amyloid Protofibrils. Based on time-force analysis, we assessed the mechanical properties of capped and uncapped TTR amyloid protofibrils by generating stress-strain curves. Stress-strain curves for our *in silico* protofibrils were produced by calculating the strain and using Hooke's law as described in Section 2.3. The stress-strain graphs are depicted in Figure 6. As can be seen in Figure 6(a), under 0.001 Å/ps constant-velocity loading simulation, capped protofibrils have higher stress values than uncapped protofibrils at around 0.5 strain regions. The calculated strain differs under the velocity loading condition of 0.005 Å/ps, as shown in Figure 6(b). Using this stress-strain relationship, we calculated Young's modulus, as shown in Figure 6(c). Under both loading simulation conditions (0.001 Å/ps and 0.005 Å/ps), we can see that Young's modulus of capped protofibrils (7–8 GPa) was larger than that of uncapped protofibrils (6–6.5 GPa). These results are consistent with our previous equilibrated MD and PCA analysis results, in which the axial elastic modulus of capped TTR protofibrils was higher than the uncapped TTR protofibrils. Furthermore, Young's modulus

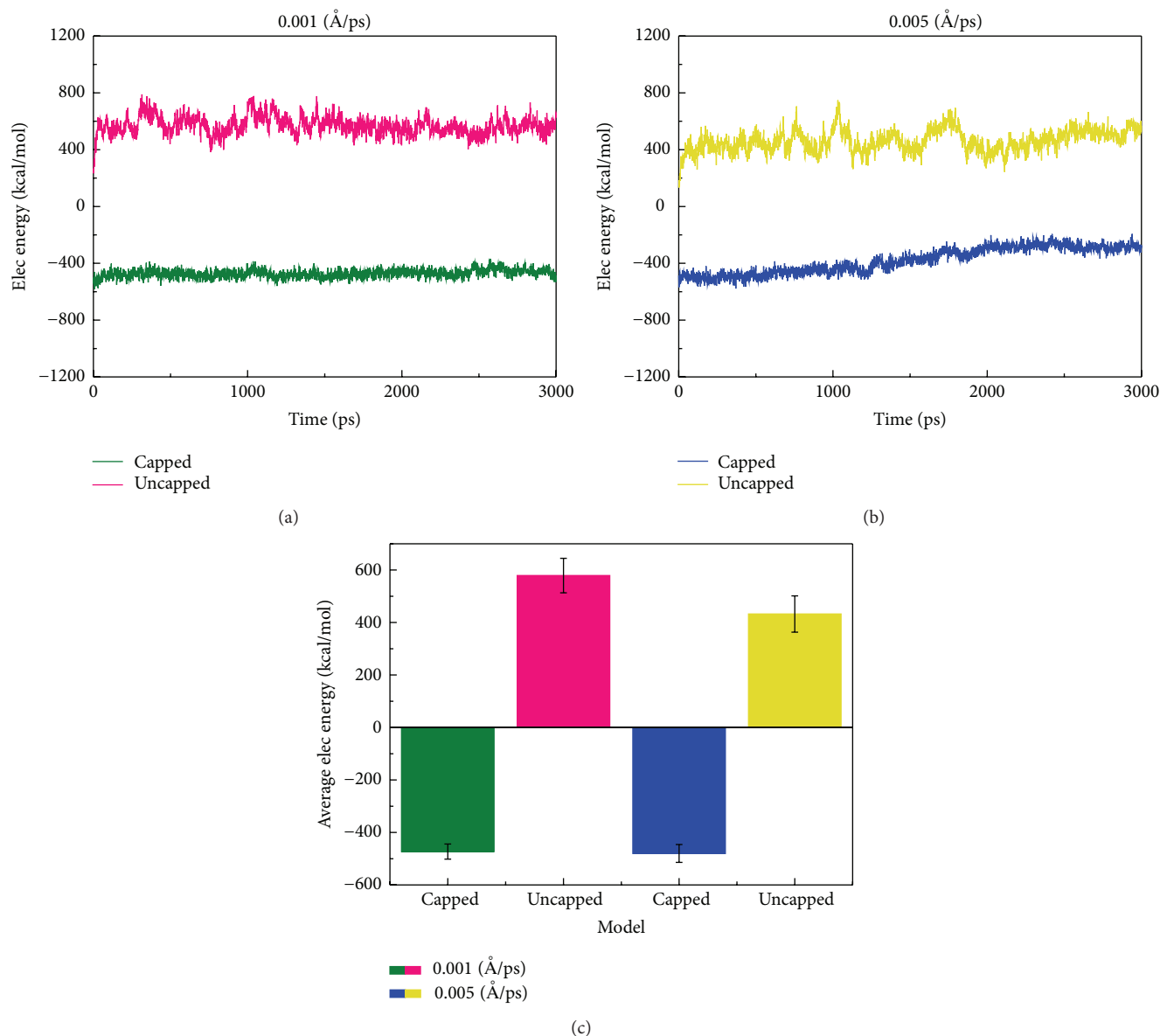


FIGURE 5: Time versus electrostatic energy graphs: comparing the structural characteristics effect of end-terminal capping on TTR (105–115) protofibrils. (a) shows the comparison graph for the simulation performed using a velocity of 0.001 \AA/ps , (b) shows the graph using a velocity of 0.005 \AA/ps , and (c) shows the average number of electrostatic energies. Error bars represent the standard deviations.

difference of capped and uncapped TTR amyloid protofibrils with respect to various pulling speed also can be compared to bending simulation on hIAPP fibrils along with various length size [41]. From their result of bending and shear stress, both stresses were increased when pulling speed also increased. Considering the similar elastic modulus results obtained in this study, our Young's modulus of TTR amyloid protofibrils is higher when applied 0.005 \AA/ps than those of 0.001 \AA/ps . That means that higher mechanical response of amyloid fibril comes from the faster pulling speed.

Young's modulus values we obtained using SMD simulations can be compared to previous experimental studies on TTR 105–115 fibrils. Meersman et al. reported that the bulk

modulus of TTR 105–115 fibril is 2.6 GPa [45]. Considering that our capped and uncapped fibrils are nanoscale structures, our calculated material properties are reliable results in terms of having a similar degree of order. Our Young's modulus results can also be compared to the results obtained for different amyloid proteins, using both experimental and computational methods. As shown in Table 1, our results have a similar Young's modulus degree of order compared to previously studied amyloid, despite differences in the underlying amyloid proteins. When compared to the "parallel/homo" polymorph structure of hIAPP fibrils, our structure is predicted to have a higher Young's modulus [17, 18, 21]. In addition, our simulations suggest that both

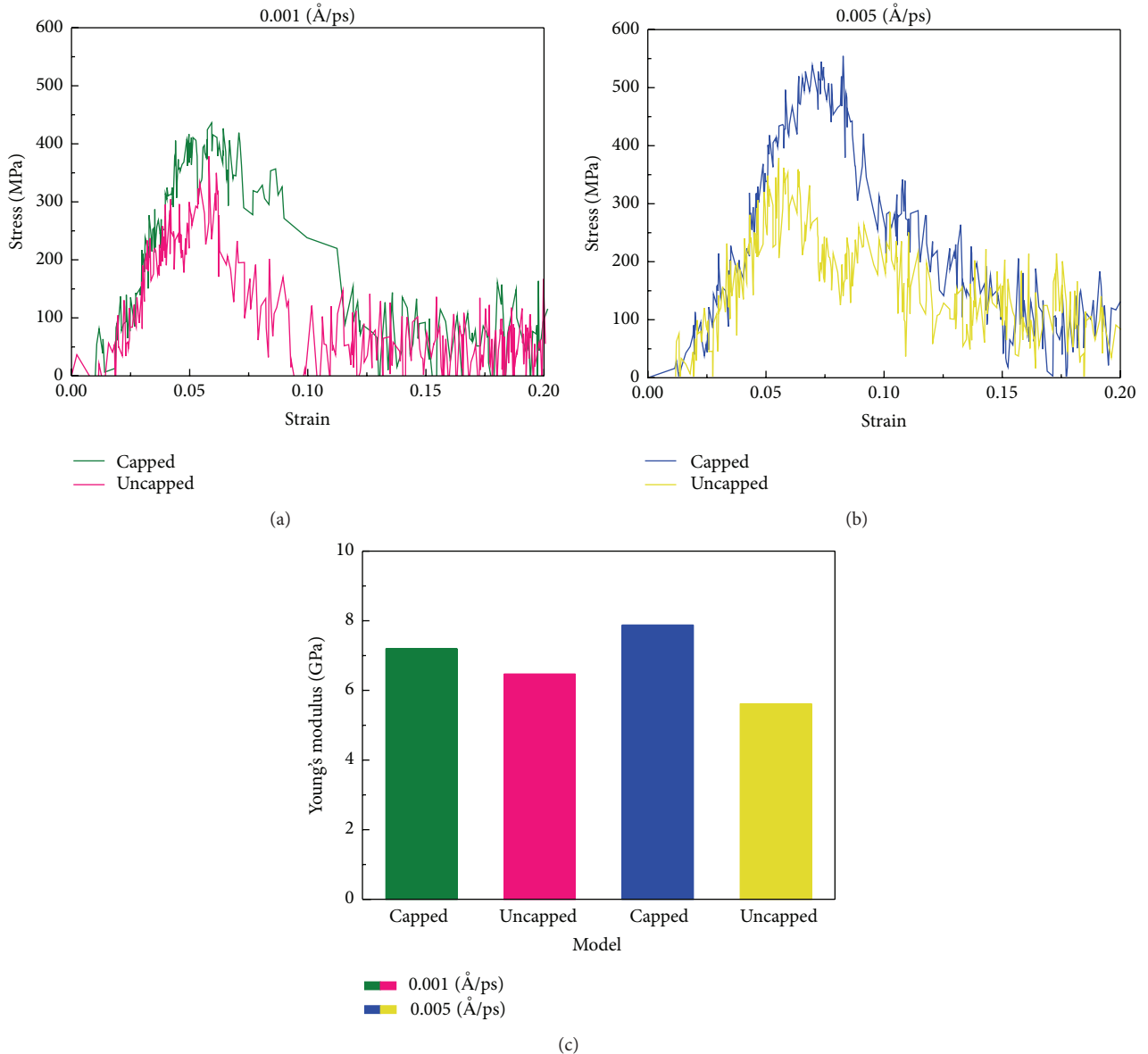


FIGURE 6: Stress versus strain graphs and Young's modulus graphs. Stress-strain curves for each pulling rate (0.001 Å/ps and 0.005 Å/ps) to compute Young's modulus for both capped and uncapped fibrils. (a) Strain-stress curve calculated from pulling rate of 0.001 Å/ps, (b) strain-stress curve obtained from pulling rate of 0.005 Å/ps, and (c) Young's modulus of uncapped and capped TTR 105–115 protofibrils from stress-strain curves.

TABLE 1: The tensile Young's modulus of several amyloid fibrils for the comparison.

Structures	Elastic modulus (GPa)
hIAPP (SMD) [17, 18]	2.4–12
hIAPP (ENM) [19]	12–14
A β (SMD) [42–44]	12.4–17.2
TTR (experiment) [45]	2.6
TTR (our study)	6–8

uncapped and capped TTR 105–115 protofibrils have a higher Young's modulus than insulin amyloid fibrils.

From our computational stress-strain and Young's modulus analyses, we predict that end-terminal capping of TTR

105–115 protofibril results in material with a higher Young's modulus than uncapped protofibrils. Our results including time-force graphs, fracture trajectory analysis, the number of hydrogen bonds, and electrostatic force analysis due to the end-terminal capping effects are consistent with previous similar amyloid studies. Further, our results show the reliable data compared to previous experimental and computational TTR 105–115 amyloid fibril studies.

4. Conclusions

In this study, we calculated material properties of capped and uncapped TTR (105–115) protofibrils by investigating

their structural and mechanical response to different loadings at constant-velocity, using steered molecular dynamics. Analysis of the time-force and rupture trajectory profiles showed that capped protofibrils have a greater rupture force but lower ruptured beta-strand contents than uncapped protofibrils. These profiles were consistent with an analysis of electrostatic energy fluctuations and the number of the hydrogen bonds. During the fracture process, we found larger electrostatic force fluctuations in uncapped protofibrils than capped protofibrils. Further, we computationally derived and predicted the material properties of the protofibrils from our SMD simulations. Stress-strain curves indicated that capped protofibrils are likely to have a larger Young's modulus (7–8 GPa) than uncapped protofibrils (6–6.5 GPa). Understanding the mechanical characteristics of amyloid protofibrils is important, since their growth mechanism relies on fragmentation and elongation. Our study provides a useful model of the effect of end-terminal capping on TTR 105–115 amyloid protofibrils. In particular, since amyloid fibrils are increasingly being used as basic templates for functional material [46], our study suggests an additional material design methodology for templating biofunctional materials.

Competing Interests

The authors declare that there is no conflict of interests regarding the publication of this paper.

Authors' Contributions

Myeongsang Lee and Hyunsung Choi made equal contribution.

Acknowledgments

Sungsoo Na gratefully acknowledges the Basic Science Research Program, through the National Research Foundation of Korea (NRF), and is funded by the Ministry of Science, ICT & Future Planning (MSIP) (Grant no. 2014RIA2A1A11052389).

References

- [1] G. Merlini and V. Bellotti, "Molecular mechanisms of amyloidosis," *The New England Journal of Medicine*, vol. 349, no. 6, pp. 583–596, 2003.
- [2] C. Soto, "Unfolding the role of protein misfolding in neurodegenerative diseases," *Nature Reviews Neuroscience*, vol. 4, no. 1, pp. 49–60, 2003.
- [3] F. Chiti and C. M. Dobson, "Protein misfolding, functional amyloid, and human disease," *Annual Review of Biochemistry*, vol. 75, pp. 333–366, 2006.
- [4] J. W. M. Höppener, B. Ahrén, and C. J. M. Lips, "Islet amyloid and type 2 diabetes mellitus," *The New England Journal of Medicine*, vol. 343, no. 6, pp. 411–419, 2000.
- [5] N. M. Kad, S. L. Myers, D. P. Smith, D. A. Smith, S. E. Radford, and N. H. Thomson, "Hierarchical assembly of β 2-microglobulin amyloid in vitro revealed by atomic force microscopy," *Journal of molecular biology*, vol. 330, no. 4, pp. 785–797, 2003.
- [6] N. M. Kad, N. H. Thomson, D. P. Smith, D. A. Smith, and S. E. Radford, " β 2-microglobulin and its deamidated variant, N17D form amyloid fibrils with a range of morphologies in vitro," *Journal of Molecular Biology*, vol. 313, no. 3, pp. 559–571, 2001.
- [7] C. Rapezzi, C. C. Quarta, L. Riva et al., "Transthyretin-related amyloidoses and the heart: a clinical overview," *Nature Reviews Cardiology*, vol. 7, no. 7, pp. 398–408, 2010.
- [8] J. N. Dungu, L. J. Anderson, C. J. Whelan, and P. N. Hawkins, "Cardiac transthyretin amyloidosis," *Heart*, vol. 98, no. 21, pp. 1546–1554, 2012.
- [9] T. P. J. Knowles and M. J. Buehler, "Nanomechanics of functional and pathological amyloid materials," *Nature Nanotechnology*, vol. 6, no. 8, pp. 469–479, 2011.
- [10] M. J. Buehler and Y. C. Yung, "Deformation and failure of protein materials in physiologically extreme conditions and disease," *Nature Materials*, vol. 8, no. 3, pp. 175–188, 2009.
- [11] C. Haass and D. J. Selkoe, "Soluble protein oligomers in neurodegeneration: lessons from the Alzheimer's amyloid β -peptide," *Nature Reviews Molecular Cell Biology*, vol. 8, no. 2, pp. 101–112, 2007.
- [12] S. A. Kotler, P. Walsh, J. R. Brender, and A. Ramamoorthy, "Differences between amyloid- β aggregation in solution and on the membrane: insights into elucidation of the mechanistic details of Alzheimer's disease," *Chemical Society Reviews*, vol. 43, no. 19, pp. 6692–6700, 2014.
- [13] J. R. Brender, D. L. Heyl, S. Samiseti et al., "Membrane disordering is not sufficient for membrane permeabilization by islet amyloid polypeptide: studies of IAPP(20–29) fragments," *Physical Chemistry Chemical Physics*, vol. 15, no. 23, pp. 8908–8915, 2013.
- [14] J. R. Brender, S. Salamekh, and A. Ramamoorthy, "Membrane disruption and early events in the aggregation of the diabetes related peptide IAPP from a molecular perspective," *Accounts of Chemical Research*, vol. 45, no. 3, pp. 454–462, 2012.
- [15] S. R. Collins, A. Douglass, R. D. Vale, and J. S. Weissman, "Mechanism of prion propagation: amyloid growth occurs by monomer addition," *PLoS Biology*, vol. 2, article e321, 2004.
- [16] J. F. Smith, T. P. J. Knowles, C. M. Dobson, C. E. MacPhee, and M. E. Welland, "Characterization of the nanoscale properties of individual amyloid fibrils," *Proceedings of the National Academy of Sciences of the United States of America*, vol. 103, no. 43, pp. 15806–15811, 2006.
- [17] M. Lee, H. J. Chang, D. Kim et al., "Relationship between structural composition and material properties of polymorphic hIAPP fibrils," *Biophysical Chemistry*, vol. 199, pp. 1–8, 2015.
- [18] M. Lee, I. Baek, H. J. Chang, G. Yoon, and S. Na, "The bond survival time variation of polymorphic amyloid fibrils in the mechanical insight," *Chemical Physics Letters*, vol. 600, pp. 68–72, 2014.
- [19] G. Yoon, J. Kwak, J. I. Kim, S. Na, and K. Eom, "Mechanical characterization of amyloid fibrils using coarse-grained normal mode analysis," *Advanced Functional Materials*, vol. 21, no. 18, pp. 3454–3463, 2011.
- [20] G. Yoon, Y. K. Kim, K. Eom, and S. Na, "Relationship between disease-specific structures of amyloid fibrils and their mechanical properties," *Applied Physics Letters*, vol. 102, Article ID 011914, 2013.
- [21] J. I. Kim, M. Lee, I. Baek, G. Yoon, and S. Na, "The mechanical response of hIAPP nanowires based on different bending

- direction simulations,” *Physical Chemistry Chemical Physics*, vol. 16, no. 34, pp. 18493–18500, 2014.
- [22] H. J. Chang, I. Baek, M. Lee, and S. Na, “Influence of aromatic residues on the material characteristics of A β amyloid protofibrils at the atomic scale,” *ChemPhysChem*, vol. 16, no. 11, pp. 2403–2414, 2015.
- [23] R. Paparcone, M. A. Pires, and M. J. Buehler, “Mutations alter the geometry and mechanical properties of Alzheimer’s A β (1–40) amyloid fibrils,” *Biochemistry*, vol. 49, no. 41, pp. 8967–8977, 2010.
- [24] M. Lee, I. Baek, H. Choi, J. I. Kim, and S. Na, “Effects of lysine residues on structural characteristics and stability of tau proteins,” *Biochemical and Biophysical Research Communications*, vol. 466, no. 3, pp. 486–492, 2015.
- [25] M. Solar and M. J. Buehler, “Tensile deformation and failure of amyloid and amyloid-like protein fibrils,” *Nanotechnology*, vol. 25, no. 10, Article ID 105703, 2014.
- [26] Z. Xu, R. Paparcone, and M. J. Buehler, “Alzheimer’s A β (1–40) amyloid fibrils feature size-dependent mechanical properties,” *Biophysical Journal*, vol. 98, no. 10, pp. 2053–2062, 2010.
- [27] H. Choi, H. J. Chang, Y. Shin et al., “The molecular mechanism of conformational changes of the triplet prion fibrils for pH,” *RSC Advances*, vol. 5, no. 61, pp. 49263–49269, 2015.
- [28] H. Ndlovu, A. E. Ashcroft, S. E. Radford, and S. A. Harris, “Molecular dynamics simulations of mechanical failure in polymorphic arrangements of amyloid fibrils containing structural defects,” *Beilstein Journal of Nanotechnology*, vol. 4, no. 1, pp. 429–440, 2013.
- [29] H. Ndlovu, A. E. Ashcroft, S. E. Radford, and S. A. Harris, “Effect of sequence variation on the mechanical response of amyloid fibrils probed by steered molecular dynamics simulation,” *Biophysical Journal*, vol. 102, no. 3, pp. 587–596, 2012.
- [30] G. Yoon, M. Lee, J. I. Kim, S. Na, and K. Eom, “Role of sequence and structural polymorphism on the mechanical properties of amyloid fibrils,” *PLoS ONE*, vol. 9, no. 2, Article ID e88502, 2014.
- [31] M. Porrini, U. Zachariae, P. E. Barran, and C. E. MacPhee, “Effect of protonation state on the stability of amyloid oligomers assembled from TTR(105–115),” *The Journal of Physical Chemistry Letters*, vol. 4, no. 8, pp. 1233–1238, 2013.
- [32] M. Andreassen, K. K. Skeby, S. Zhang et al., “The importance of being capped: terminal capping of an amyloidogenic peptide affects fibrillation propensity and fibril morphology,” *Biochemistry*, vol. 53, no. 44, pp. 6968–6980, 2014.
- [33] K. Tao, J. Wang, P. Zhou et al., “Self-assembly of short A β (16–22) peptides: effect of terminal capping and the role of electrostatic interaction,” *Langmuir*, vol. 27, no. 6, pp. 2723–2730, 2011.
- [34] V. Castelletto, I. W. Hamley, Ç. Cenker et al., “Influence of end-capping on the self-assembly of model amyloid peptide fragments,” *Journal of Physical Chemistry B*, vol. 115, no. 9, pp. 2107–2116, 2011.
- [35] M. Lee and S. Na, “End capping alters the structural characteristics and mechanical properties of transthyretin (105–115) amyloid protofibrils,” *ChemPhysChem*, vol. 17, no. 3, pp. 425–432, 2016.
- [36] A. W. P. Fitzpatrick, G. T. Debelouchina, M. J. Bayro et al., “Atomic structure and hierarchical assembly of a cross- β amyloid fibril,” *Proceedings of the National Academy of Sciences of the United States of America*, vol. 110, no. 14, pp. 5468–5473, 2013.
- [37] C. P. Jaroniec, C. E. MacPhee, V. S. Bajaj, M. T. McMahon, C. M. Dobson, and R. G. Griffin, “High-resolution molecular structure of a peptide in an amyloid fibril determined by magic angle spinning NMR spectroscopy,” *Proceedings of the National Academy of Sciences of the United States of America*, vol. 101, no. 3, pp. 711–716, 2004.
- [38] C. P. Jaroniec, C. E. MacPhee, N. S. Astrof, C. M. Dobson, and R. G. Griffin, “Molecular conformation of a peptide fragment of transthyretin in an amyloid fibril,” *Proceedings of the National Academy of Sciences of the United States of America*, vol. 99, no. 26, pp. 16748–16753, 2002.
- [39] W. Humphrey, A. Dalke, and K. Schulten, “VMD: visual molecular dynamics,” *Journal of Molecular Graphics*, vol. 14, no. 1, pp. 33–38, 1996.
- [40] J. C. Phillips, R. Braun, W. Wang et al., “Scalable molecular dynamics with NAMD,” *Journal of Computational Chemistry*, vol. 26, no. 16, pp. 1781–1802, 2005.
- [41] B. Choi, G. Yoon, S. W. Lee, and K. Eom, “Mechanical deformation mechanisms and properties of amyloid fibrils,” *Physical Chemistry Chemical Physics*, vol. 17, no. 2, pp. 1379–1389, 2015.
- [42] R. Paparcone and M. J. Buehler, “Failure of A β (1–40) amyloid fibrils under tensile loading,” *Biomaterials*, vol. 32, no. 13, pp. 3367–3374, 2011.
- [43] R. Paparcone, S. Keten, and M. J. Buehler, “Atomistic simulation of nanomechanical properties of Alzheimer’s AB(1–40) amyloid fibrils under compressive and tensile loading,” *Journal of Biomechanics*, vol. 43, no. 6, pp. 1196–1201, 2010.
- [44] R. Paparcone, S. Keten, and M. Buehler, “Amyloid nanofibrils under compressive loading,” *Journal of Biomechanics*, vol. 43, pp. 1196–1201, 2009.
- [45] F. Meersman, R. Q. Cabrera, P. F. McMillan, and V. Dmitriev, “Structural and mechanical properties of TTR105–115 amyloid fibrils from compression experiments,” *Biophysical Journal*, vol. 100, no. 1, pp. 193–197, 2011.
- [46] I. Cherny and E. Gazit, “Amyloids: not only pathological agents but also ordered nanomaterials,” *Angewandte Chemie—International Edition*, vol. 47, no. 22, pp. 4062–4069, 2008.

Research Article

Sensitivity Analysis for the Mechanical Properties of DNA Bundles

Young-Joo Kim¹ and Do-Nyun Kim^{1,2}

¹Department of Mechanical and Aerospace Engineering, Seoul National University, Building 301, Room 1516, Gwanak-ro 1, Gwanak-gu, Seoul 08826, Republic of Korea

²Institute of Advanced Machines and Design, Seoul National University, Gwanak-ro 1, Gwanak-gu, Seoul 08826, Republic of Korea

Correspondence should be addressed to Do-Nyun Kim; dnkim@snu.ac.kr

Received 31 December 2015; Accepted 19 April 2016

Academic Editor: Serdal Kirmizialtin

Copyright © 2016 Y.-J. Kim and D.-N. Kim. This is an open access article distributed under the Creative Commons Attribution License, which permits unrestricted use, distribution, and reproduction in any medium, provided the original work is properly cited.

In structural DNA nanotechnology, programming a three-dimensional shape into DNA bundles has been a primary design objective. However, the mechanical properties of these DNA bundle structures are another important factor to be considered in the design process. While the mechanics of the individual DNA double helix has been explored extensively and hence its properties are well known, the mechanical properties of structural motifs such as DNA junctions and strand breaks important to bundle mechanics have not been well characterized due to experimental limitations, rendering it difficult to predict the mechanical properties of DNA bundles. Here, we investigate the effect of these structural motifs on the global bundle rigidities by performing sensitivity analysis on a six-helix DNA bundle structure using the finite element modeling approach. Results reveal the primary structural features and their parametric values required to reproduce the experimental bundle rigidities.

1. Introduction

Structural DNA nanotechnology has enabled us to build various molecular structures with desired patterns and shapes at the nanometer scale [1, 2]. By designing a connectivity map between DNA double helices at discrete crossover positions, one can fold DNA strands into the two- to three-dimensional structures [2–8] with target curvatures or twists [9, 10]. These structures have been widely used in many applications including the nanometer-precision arrangement of nanoparticles, proteins or fluorescence molecules [11–13], the controlled growth of gold nanoparticles into a three-dimensional shape by using DNA nanostructures as a mold [14, 15], and the measurement of single-molecule properties [16].

While the solution shape has been a primary design objective for constructing a target DNA nanostructure, the mechanical properties should be also taken into consideration in the design process as they not only govern the stability, flexibility, and deformability of the structure but also affect the derived functional properties facilitated by interacting

with molecules or particles attached to it. Although studies on the mechanical properties of the B-form DNA double helix are abundant, those for DNA bundles [17–19] are scarce because of the lack of information on the mechanical properties of structural motifs such as DNA junctions and strand breaks important to bundle mechanics due to experimental limitation. Therefore, it is difficult to predict the mechanical properties of DNA bundles in the design process.

Here, we investigate the effect of the mechanical properties of structural motifs, which have been ill-characterized and largely unknown, on the DNA bundle rigidities by analyzing a six-helix DNA bundle structure whose bending and torsional rigidities were known experimentally [17]. We employ the finite element (FE) method to calculate the bundle rigidities for systematically varied model parameters including the distance between the adjacent helices and the rigidities of crossovers and nicks. Results reveal plausible roles of these parameters on the global bundle rigidities and provide their values reproducing the experimental bundle properties.

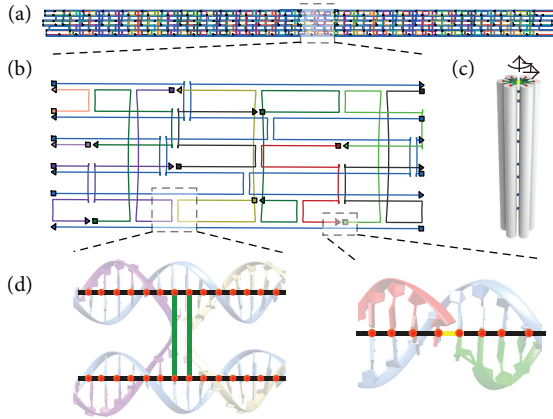


FIGURE 1: Six-helix DNA bundle structure. (a-b) Two-dimensional blueprint, (c) three-dimensional rendering of the structure, and (d) finite element models of a crossover (left) and a nick (right). In (d), black, green, and yellow lines represent beam elements used to model normal DNA double helices, crossovers, and nicks, respectively. Red dots are FE nodes.

2. Materials and Methods

2.1. Six-Helix Bundle. The six-helix DNA bundle [17] is a straight, 371 nm long structure designed in the honeycomb lattice and consisting of a 6552-base-long scaffold strand and 156 short staple strands most of which have 42 bases (Figure 1). Originally, it has two supporting parts at both ends of the structure for experiments, but we excluded them in this study as they are not necessary in our computational analysis. The helices are connected discretely at 595 crossover positions that are almost evenly distributed along the helical axis. 156 strand breaks or nicks exist almost every 42 base pairs in the bundle as it is folded by the short staple strands. More details on the six-helix DNA bundle are available in [17] including sequence information of comprising DNA strands, connectivity maps between helices, and experimental methods to synthesize and characterize the bundle.

2.2. Finite Element Model. The three-dimensional FE model of the six-helix DNA bundle structure is constructed from its two-dimensional blueprint [20] that provides the location of each helix on a lattice and the crossover positions where the helices are connected to one another. Each helix is modeled as a straight, homogeneous, isotropic, and elastic rod using a set of two-node Hermitian beam elements with the stretching ($S_{B-DNA} = 1,100$ pN), bending ($B_{B-DNA} = 230$ pNm²), and torsional ($C_{B-DNA} = 460$ pNm²) rigidities measured experimentally for the B-form DNA [21] neglecting any sequence dependency. FE nodes are placed at the center of base pairs where six degrees of freedom (DOFs) are assigned to each node to describe the displacement of the center position and the rotation of the beam cross section. They exist every 0.34 nm along the helical axis in the undeformed configuration with the right-handed twist rate of 34.29° per base pair determining the orientation of the beam cross section. At the nick positions where one of the phosphate backbones

is broken, beams with reduced bending and torsional rigidities are used instead while the same stretching rigidity as the B-form DNA is used. Six helices form a bundle structure on the honeycomb lattice with the interhelical distance between the neighboring helices. Two FE nodes between the adjacent helices at a crossover position are connected to each other using a beam element whose rigidities determine the flexibilities between the helices at the junction position.

2.3. Sensitivity Analysis. We investigate the sensitivity of the bundle rigidities on the principal structural parameters, which are difficult to measure experimentally, governing the geometry and the mechanical properties of the six-helix DNA bundle structure. We calculate the stretching (S), bending (B), and torsional (C) rigidities of the bundle for exhaustively varied parametric values including the interhelical distance (D), the reduced bending (B_{nick}) and torsional (C_{nick}) rigidities of the beam element at nicks, and the stretching (S_{cross}), bending (B_{cross}), and torsional (C_{cross}) rigidities of the beam element at crossover positions. At the ends of the bundle, two fictitious FE nodes are generated on the mean position of the helix centers and connected rigidly to the nodes on the same cross-sectional plane where boundary conditions and loading conditions are applied. S , B , and C of the bundle for each parameter set are obtained by performing linear static analysis where we impose a unit tensile displacement, a unit shear displacement for bending, or a unit torsional angle on one end of the bundle while fixing the other end and measure the axial reaction force, the shear reaction force, or the torsional reaction moment, respectively. The default values used for these parameters when not varied are $D = 2.25$ nm, $S_{cross}/S_{B-DNA} = B_{cross}/B_{B-DNA} = C_{cross}/C_{B-DNA} = 10^5$, and $B_{nick}/B_{B-DNA} = C_{nick}/C_{B-DNA} = 10^{-2}$.

3. Results and Discussion

3.1. Isotropic Bending Rigidity. Due to the helicity of the B-form DNA (two full turns per 21 base pairs), crossover positions are rotating 240 degrees every seven base pairs along the helical axis on the honeycomb lattice, resulting in an asymmetric crosslinking arrangement. Therefore, the bending rigidity of the bundle naturally varies with the direction of curvature. The bundle exhibits the highest bending rigidity for bending along the vertical axis while it shows the lowest rigidity for bending along the horizontal axis. Nevertheless, the difference between the maximum and minimum bending rigidities is negligibly small (less than 0.2% of the mean value) and hence we can assume that the bending rigidity of the bundle is almost isotropic (Figure 2). This is because the bundle uses the highest crossover density available for honeycomb-latticed structures. More specifically, a DNA double helix in the six-helix bundle is connected to one of its three neighboring helices every seven base pairs forming a 21-base-pair-long repeating unit. Approximately 50 units exist along the helical axis that are large enough to attenuate the effect of crossover asymmetry on the overall bending rigidity of the bundle.

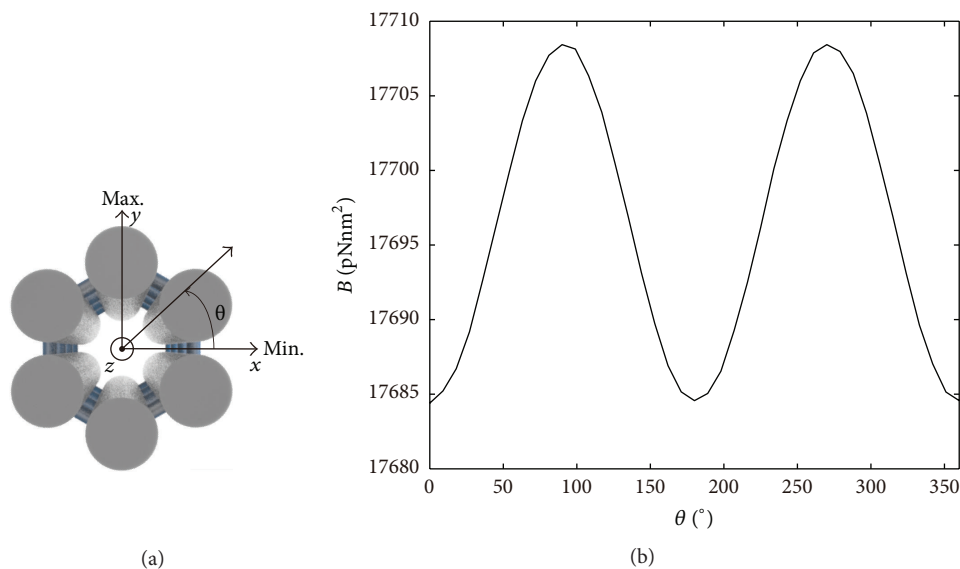


FIGURE 2: Bending rigidity. (a) Definition of the axis along which the bundle bends and (b) the bending rigidity of the bundle.

3.2. Effect of the Interhelical Distance. Here, we investigate the effect of the distance between the helices on the overall bundle rigidities. It is well known that the diameter of the B-form DNA is about 2 nm, which might be a natural choice for the interhelical distance if we assume that the helices are in contact with one another almost all the way along the helical axis. However, as the DNA double helix is highly negatively charged, the repulsive forces whose strength is dependent on the ionic condition exist between the helices. On the other hand, it is shown experimentally that the interhelical distance at crossover positions is smaller than the helix diameter amounting to 1.85 nm. As a result, the helices undulate in the bundle rather than taking a straight, parallel configuration because they expel one another while constrained at crossover positions. Nonetheless, we often model the structure as a bundle of straight DNA helices separated at an effective interhelical distance corresponding to the mean distance between the undulating helices without including electrostatics explicitly into the model, which has been successful to predict the three-dimensional shape of DNA origami nanostructures [1, 22].

Here, we adopt this modeling approach and study how the effective interhelical distance affects the bundle rigidities by varying it from 1.8 nm to 2.5 nm. Results clearly demonstrate that the stretching rigidity of the bundle is invariant to the interhelical distance (Figure 3(a)). This is because the axial force is divided and applied equally to each helix resulting in a uniform axial deformation of the helices regardless of their relative locations. Bending and torsional rigidities of the bundle, in contrast, are dependent on the interhelical distance (Figures 3(b) and 3(c)) resulting primarily from the fact that area moments of inertia increase with the interhelical distance as the helices become located farther from the bundle's central axis.

3.3. Effect of the Mechanical Properties of Crossovers. The mechanical properties of crossovers are the most crucial factors affecting the global bundle rigidities as DNA double helices are interconnected only at these discrete positions. These crossovers are four-way Holliday junctions that are structurally polymorphic when free in solution and can undergo the transition between an unstable, open conformer and more stable, stacked conformers [23]. These junction structures take a right-handed stacked conformation in a bundle under usual ionic conditions and provide the crosslinking stiffness between the adjacent helices. While it has been shown both experimentally and computationally that crossovers are quite flexible in scissor-like motion of junction arms [5, 24], their exact mechanical properties have not been characterized well. Here we explore how the mechanical properties of crossovers affect the bending and torsional rigidities of the six-helix bundle by varying the stretching, bending, and torsional rigidities of crossovers. The stretching rigidity of the bundle does not change with the crossover rigidities as all six helices are stretched or compressed uniformly.

Results indicate that both bending and torsional rigidities of the bundle are almost independent of the stretching rigidity of crossovers (Figure 4). This is because the global bending or twisting of the bundle requires the bending or twisting of individual helices relative to one another without the change in the interhelical distance. On the contrary, the bending rigidity of crossovers exerts a strong influence on the bundle rigidity in both bending and torsion. As crossovers become flexible in bending, beam elements across the neighboring helices at crossover positions can bend under externally applied bending or torsional moments, resulting in the decrease of the interhelical distance and the consequent reduction of the bundle rigidities (Figure 3). The torsional rigidity of crossovers controlling the scissor-like rotation

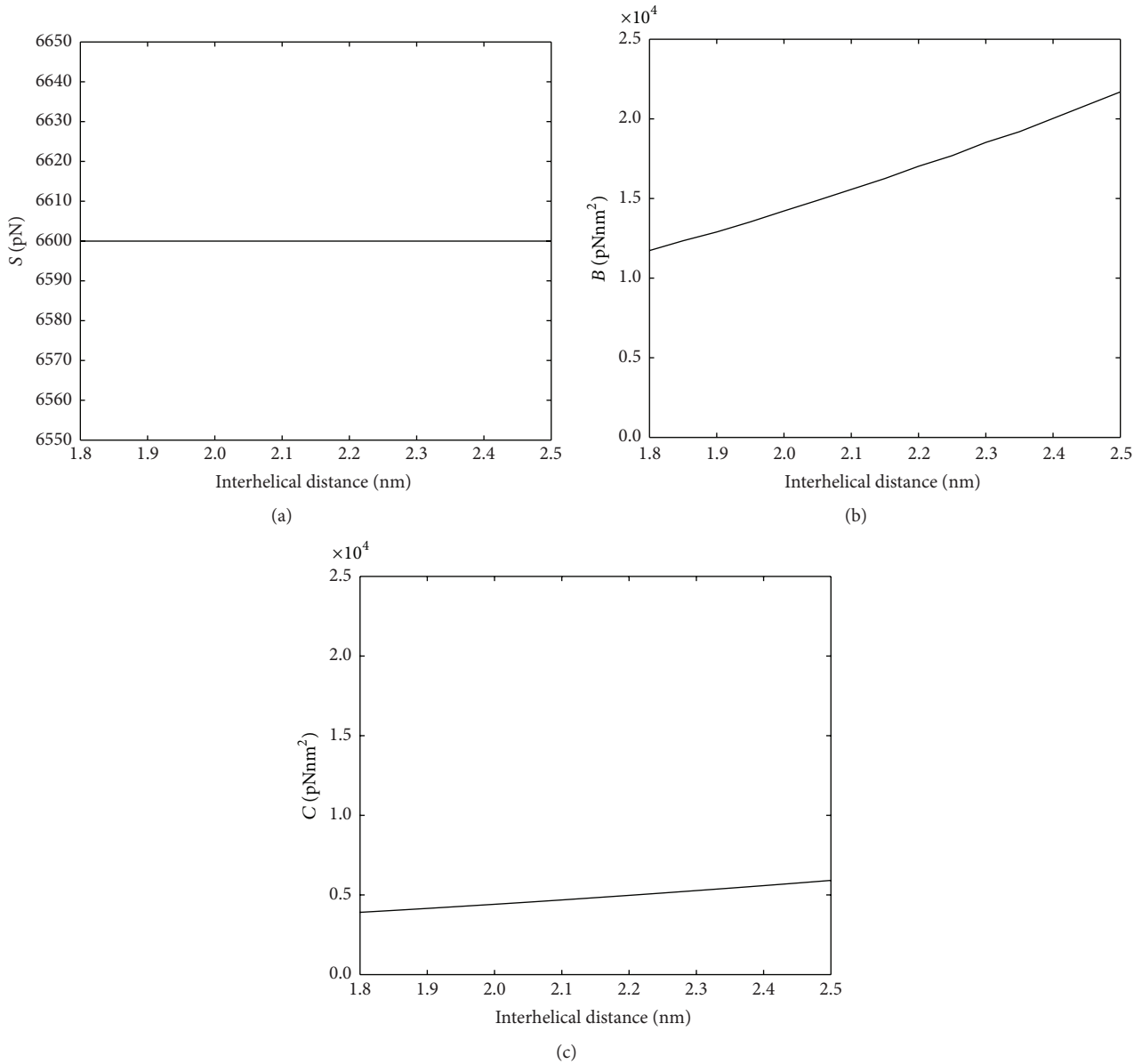


FIGURE 3: Effect of the interhelical distance. (a) Stretching, (b) bending, and (c) torsional rigidities of the bundle at various interhelical distances.

of the interconnected helices affects the torsional bundle rigidity only since the scissor-like rotation does not occur in bending of the bundle. It is noteworthy that both bending and torsional rigidities of crossovers should be smaller than those of the B-form DNA double helix in order to reproduce the experimental bundle rigidities.

3.4. Effect of the Mechanical Properties of Nicks. As DNA bundles are formed by the aid of many short single stranded DNA segments, nicks (or strand breaks) always exist in a DNA bundle and hence it is important to understand their mechanical roles on the bundle rigidities. However, the mechanical properties of nicks have not been well quantified yet while there is a general consensus that they act like a hinge

or swivel with smaller rigidities than those of nonnicked DNA. Hence, we explore the effect of the mechanical properties of nicks on the bundle rigidities by varying the bending and torsional rigidities of nicks while fixing their stretching rigidity to that of the B-form DNA.

It turns out that nicks affect the torsional rigidity of the bundle but have a negligible influence on the bending rigidity (Figure 5). In torsion, the bundle is more sensitive to the torsional rigidity of nicks than the bending rigidity as individual helices can be twisted locally at nick positions in addition to global twist of the bundle. But, if the bending rigidity of nicks is sufficiently small, then it can reduce the torsional rigidity of the bundle significantly as individual helices now can be bent or kinked locally at nick positions under torsion. Therefore, we need to take the location, the density, and the mechanical

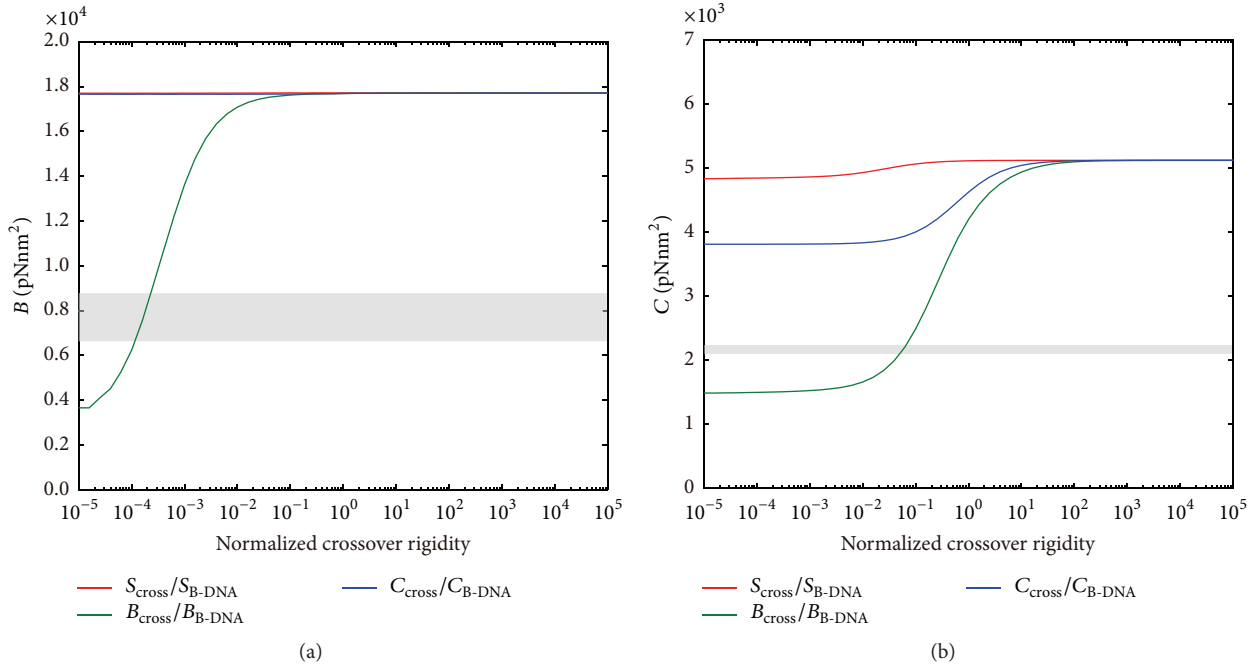


FIGURE 4: Effect of the mechanical properties of crossovers. (a) Bending and (b) torsional rigidities of the bundle computed using various crossover rigidities. Shaded areas represent the experimentally measured rigidities.

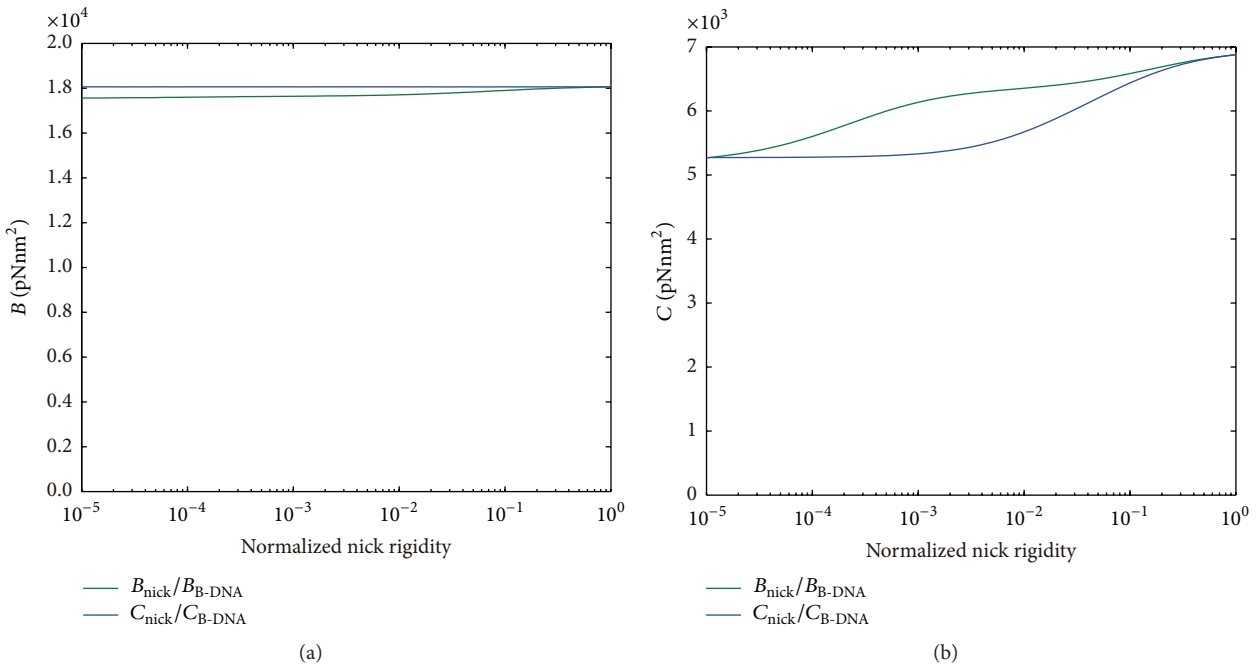


FIGURE 5: Effect of the mechanical properties of nicks. (a) Bending and (b) torsional rigidities of the bundle computed using various nick rigidities.

properties of nicks into consideration when we design a DNA bundle structure exposed to torsional loadings.

3.5. Comparison with Other Models. Based on the results of sensitivity analysis, we can estimate the parametric values of the model reproducing the bending and torsional rigidities of the six-helix bundle measured experimentally. If we use the

interhelical distance of 2.25 nm representing an effective helical diameter at usual ionic concentrations used for DNA bundles, the model predicts the bending and torsional rigidities of 7,247 pNnm² and 2,198 pNnm², respectively, for the bundle. These values lie in the range of experimental rigidities, 6,624~8,846 pNnm² for bending and 2,098~2,263 pNnm² for torsion corresponding to one standard deviation from the mean

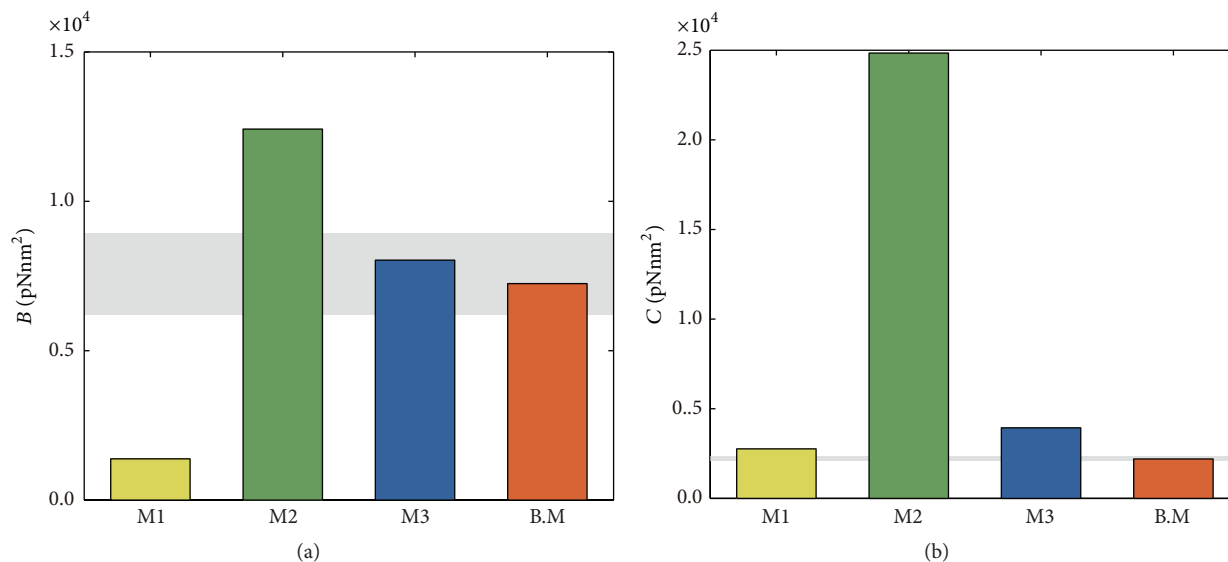


FIGURE 6: Bundle rigidities computed using several DNA models. (a) Bending and (b) torsional rigidities of the bundle. M1, M2, and M3 are continuum models where each DNA double helix is modeled as an isotropic cylinder. The helices are not connected in M1, continuously connected over the helices in M2, and discretely connected only at crossover positions in M3. B.M represents the beam model of the bundle (Figure 1). Shaded areas represent the experimentally measured rigidities.

rigidities [17]. Parametric values used to obtain these bundle rigidities are $B_{\text{cross}}/B_{\text{B-DNA}} = 0.000125$, $C_{\text{cross}}/C_{\text{B-DNA}} = 0.1$, and $B_{\text{nick}}/B_{\text{B-DNA}} = C_{\text{nick}}/C_{\text{B-DNA}} = 0.065$ indicating that both crossovers and nicks are much softer than the B-form DNA. The torsional rigidity of crossovers inferred from our sensitivity analysis is similar to the one obtained using the molecular dynamics simulation [24]. It would be valuable to investigate the other mechanical properties of crossovers and nicks using atomistic simulations as well in order to further validate our analysis and obtain molecular-level insights into their properties.

When compared with other models, the capabilities of the beam finite element model become more prominent (Figure 6). Three continuum bundle models [17] are considered where each DNA double helix is treated as an isotropic cylinder characterized by its Young's modulus and Poisson's ratio. These models are distinguished by the assumption in crosslinking the helices: no crosslink (M1), continuous crosslink over the entire helix (M2), and discrete crosslink at crossover positions (M3). M2 predicts excessively high rigidities of the bundle particularly in bending while M1 predicts too low rigidities particularly in torsion while M3 predicts the bundle rigidities close to experimental ones, but it is noteworthy that two different Young's moduli had to be used for bending and torsion because M3 is unable to reproduce the bending and torsional rigidities of the bundle simultaneously using single Young's modulus.

4. Conclusions

In this paper, we investigate the mechanical properties of DNA bundles by performing sensitivity analysis for the six-helix DNA bundle structure using the finite element modeling approach. The bending and torsional rigidities of the bundle that are measured experimentally are calculated

using our computational model with systematically varied parametric values including the interhelical distance, the crossover rigidities, and the nick rigidities. Results reveal that (1) the bending rigidity of the bundle is almost isotropic as a sufficiently large number of crossovers are used, (2) the interhelical distance affects the bending and torsional rigidities but has no influence on the stretching rigidity of the bundle, (3) the bending rigidity of crossovers has a dominant effect on the bundle rigidities, and (4) nicks are important for the torsional rigidity of the bundle. In addition, it is shown that the beam model can reproduce the experimental bundle rigidities while the previous continuum models cannot. Our findings are expected to be useful to design more complex DNA-based nanostructures with target shapes, mechanical properties, and derived functional properties.

Competing Interests

The authors declare that they have no competing interests.

Acknowledgments

This research was supported by the Basic Science Research Program (Grant no. 2013R1A1A1010626) through the National Research Foundation of Korea (NRF) and by the Center for Advanced Meta-Materials (CAMM) as Global Frontier Project (CAMM-2014M3A6B3063711) funded by the Ministry of Science, ICT and Future Planning.

References

- [1] C. E. Castro, F. Kilchherr, D.-N. Kim et al., "A primer to scaffolded DNA origami," *Nature Methods*, vol. 8, no. 3, pp. 221–229, 2011.

- [2] P. W. K. Rothemund, "Folding DNA to create nanoscale shapes and patterns," *Nature*, vol. 440, no. 7082, pp. 297–302, 2006.
- [3] B. Wei, M. Dai, and P. Yin, "Complex shapes self-assembled from single-stranded DNA tiles," *Nature*, vol. 485, no. 7400, pp. 623–626, 2012.
- [4] S. M. Douglas, H. Dietz, T. Liedl, B. Högberg, F. Graf, and W. M. Shih, "Self-assembly of DNA into nanoscale three-dimensional shapes," *Nature*, vol. 459, pp. 414–418, 2009.
- [5] D. Han, S. Pal, Y. Yang et al., "DNA gridiron nanostructures based on four-arm junctions," *Science*, vol. 339, no. 6126, pp. 1412–1415, 2013.
- [6] R. Iinuma, Y. Ke, R. Jungmann, T. Schlichthaerle, J. B. Woehrstein, and P. Yin, "Polyhedra self-assembled from DNA tripods and characterized with 3D DNA-PAINT," *Science*, vol. 344, no. 6179, pp. 65–69, 2014.
- [7] Y. Ke, L. L. Ong, W. M. Shih, and P. Yin, "Three-dimensional structures self-assembled from DNA bricks," *Science*, vol. 338, no. 6111, pp. 1177–1183, 2012.
- [8] E. Benson, A. Mohammed, J. Gardell et al., "DNA rendering of polyhedral meshes at the nanoscale," *Nature*, vol. 523, no. 7561, pp. 441–444, 2015.
- [9] H. Dietz, S. M. Douglas, and W. M. Shih, "Folding DNA into twisted and curved nanoscale shapes," *Science*, vol. 325, no. 5941, pp. 725–730, 2009.
- [10] D. Han, S. Pal, J. Nangreave, Z. Deng, Y. Liu, and H. Yan, "DNA origami with complex curvatures in three-dimensional space," *Science*, vol. 332, no. 6027, pp. 342–346, 2011.
- [11] R. Schreiber, N. Luong, Z. Fan et al., "Chiral plasmonic DNA nanostructures with switchable circular dichroism," *Nature Communications*, vol. 4, article 2948, 2013.
- [12] S. Rinker, Y. Ke, Y. Liu, R. Chhabra, and H. Yan, "Self-assembled DNA nanostructures for distance-dependent multivalent ligand-protein binding," *Nature Nanotechnology*, vol. 3, no. 7, pp. 418–422, 2008.
- [13] K. Pan, E. Boulais, L. Yang, and M. Bathe, "Structure-based model for light-harvesting properties of nucleic acid nanostructures," *Nucleic Acids Research*, vol. 42, no. 4, pp. 2159–2170, 2014.
- [14] W. Sun, E. Boulais, Y. Hakobyan et al., "Casting inorganic structures with DNA molds," *Science*, vol. 346, no. 6210, Article ID 1258361, 2014.
- [15] S. Helmi, C. Ziegler, D. J. Kauert, and R. Seidel, "Shape-controlled synthesis of gold nanostructures using DNA origami molds," *Nano Letters*, vol. 14, no. 11, pp. 6693–6698, 2014.
- [16] E. Pfitzner, C. Wachauf, F. Kilchherr et al., "Rigid DNA beams for high-resolution single-molecule mechanics," *Angewandte Chemie*, vol. 125, no. 30, pp. 7920–7925, 2013.
- [17] D. J. Kauert, T. Kurth, T. Liedl, and R. Seidel, "Direct mechanical measurements reveal the material properties of three-dimensional DNA origami," *Nano Letters*, vol. 11, no. 12, pp. 5558–5563, 2011.
- [18] D. Schiffels, T. Liedl, and D. K. Fygenson, "Nanoscale structure and microscale stiffness of DNA nanotubes," *ACS Nano*, vol. 7, no. 8, pp. 6700–6710, 2013.
- [19] C. E. Castro, H.-J. Su, A. E. Marras, L. Zhou, and J. Johnson, "Mechanical design of DNA nanostructures," *Nanoscale*, vol. 7, no. 14, pp. 5913–5921, 2015.
- [20] S. M. Douglas, A. H. Marblestone, S. Teerapittayanon, A. Vazquez, G. M. Church, and W. M. Shih, "Rapid prototyping of 3D DNA-origami shapes with caDNAno," *Nucleic Acids Research*, vol. 37, no. 15, pp. 5001–5006, 2009.
- [21] J. Gore, Z. Bryant, M. Nöllmann, M. U. Le, N. R. Cozzarelli, and C. Bustamante, "DNA overwinds when stretched," *Nature*, vol. 442, no. 7104, pp. 836–839, 2006.
- [22] D.-N. Kim, F. Kilchherr, H. Dietz, and M. Bathe, "Quantitative prediction of 3D solution shape and flexibility of nucleic acid nanostructures," *Nucleic Acids Research*, vol. 40, no. 7, pp. 2862–2868, 2012.
- [23] S. A. McKinney, A.-C. Déclais, D. M. J. Lilley, and T. Ha, "Structural dynamics of individual Holliday junctions," *Nature Structural Biology*, vol. 10, no. 2, pp. 93–97, 2003.
- [24] K. Pan, D.-N. Kim, F. Zhang, M. R. Adendorff, H. Yan, and M. Bathe, "Lattice-free prediction of three-dimensional structure of programmed DNA assemblies," *Nature Communications*, vol. 5, article 5578, 2014.

Review Article

Emerging Utilization of Chrysin Using Nanoscale Modification

Joohee Jung^{1,2}

¹College of Pharmacy, Duksung Women's University, Seoul 01369, Republic of Korea

²Innovative Drug Center, Duksung Women's University, Seoul 01369, Republic of Korea

Correspondence should be addressed to Joohee Jung; joohee@duksung.ac.kr

Received 14 December 2015; Revised 2 March 2016; Accepted 18 April 2016

Academic Editor: Serdal Kirmizialtin

Copyright © 2016 Joohee Jung. This is an open access article distributed under the Creative Commons Attribution License, which permits unrestricted use, distribution, and reproduction in any medium, provided the original work is properly cited.

Chrysin is a flavone found in several plants, mushroom, and honeycomb. This constituent is broadly used in herbal medicine in Asia. Since its biological activities were identified in various studies, the focus has shifted to the development of chrysin as a complementary medicine for health promotion. Chrysin is known to have chemopreventive and therapeutic effects in skin aging, atherosclerosis, inflammation, diabetes, AIDS, and cancer. However, its poor bioavailability is a bottleneck for pharmaceutical applications. To overcome the limitations and enhance the bioactive effects, methods like nanoencapsulation or conjugation have been attempted. In this review, current trends of chrysin use in the biomedical field are summarized.

1. Introduction

Flavonoids including flavones, flavanols, and flavans possess various biological activities. Their effects are utilized in herbal medicines. Chrysin (5, 7-dihydroxyflavone, Figure 1) is a flavone contained in several plants (*Passiflora caerulea* [1], *Passiflora incarnate* [2], *Oroxylum indicum* [3, 4], *Matricaria chamomilla* [5], etc.) and natural products (*Pleurotus ostreatus* [6], propolis [7, 8], honey [9], etc.).

Recently, chrysin was reported as a bioactive ingredient. In this review, the effects of chrysin are briefly summarized (Figure 2) and its complementary application is discussed. Finally, emerging nanoscale modification of chrysin is introduced.

2. Biological Activities of Chrysin

2.1. Effect on Inflammation. Inflammation is a protective reaction of the body to infection, physiological stress, drugs, and so on and activates the immune system. Acute inflammation is induced by mediators including arachidonic acid, platelet-activating factor, prostanoids, leukotrienes, lipoxins, interleukins, histamine, serotonin, and lysosomal hydrolases. Chrysin alleviates inflammation through inhibition of COX-2 [10], prostaglandin-E2 [11], histamine [12], NF- γ B

pathway [13–15], tumor necrosis factor- (TNF-) alpha [16, 17], iNOS [16], and cytokines (interleukin-1 β , interleukin-2, interleukin-6, and interleukin-12) [18] and activation of peroxisome proliferator-activated factor γ (PPAR γ) [19]. These reports suggest that chrysin could be a good agent in inflammatory diseases. When acute inflammation does not clear up, inflammatory cells persist and chronic inflammation promotes organ dysfunction [16, 20, 21]. Disabling inflammatory diseases include Parkinson disease [22], cancer [13], cerebral ischemia [23], allergy [12], and autoimmune neuritis [18]. The anti-inflammatory mechanism of chrysin could prevent inflammation-related diseases.

2.2. Effect on Atherosclerosis. Atherosclerosis and hypercholesterolemia are risk factors for coronary heart disease, which is a major cause of mortality. In atherosclerosis, a fibroinflammatory lipid plaque consisting of inflammatory cells, smooth muscle cells, lipid, and connective tissue accumulates in arteries. The major factor in atherosclerosis is oxidative metabolism of plasma lipoproteins. Oxidation of low-density lipoproteins by oxygen free radicals generates reactive oxygen species (ROS). Thus, ROS play a central role in the incidence of atherosclerosis. Overproduction of ROS also injures endothelial cells. Originally, ROS are intermediate products in oxidative phosphorylation and

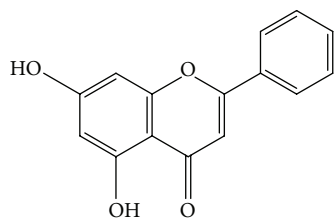


FIGURE 1: Structure of chrysin.

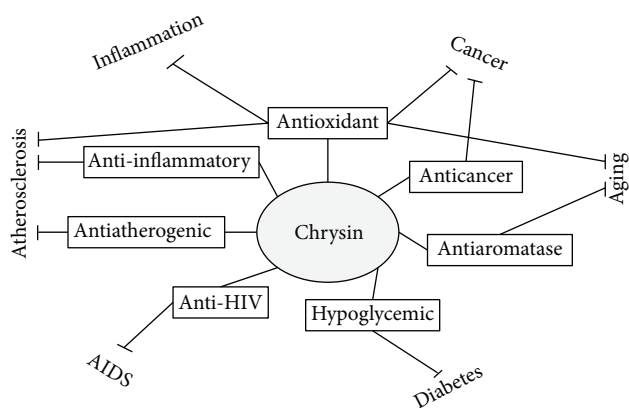


FIGURE 2: Biological activities of chrysin as a complementary medicine.

are eliminated by sufficient levels of superoxide dismutase (SOD), glutathione peroxidase (GPx), and catalase (CAT). However, oxidative stress-induced ROS accumulate and impair cells when these enzymes are depleted. Chrysin can scavenge ROS as chrysin increases SOD, GPx, and CAT [11, 24, 25]. Furthermore, chrysin controls cholesterol efflux [26] and suppresses TNF- α -induced adhesion molecule expression [27]. These activities of chrysin could prevent atherosclerosis.

2.3. Effect on Diabetes. Diabetes, one of the lifestyle diseases, is described as a high glucose level in blood. Diabetes-induced complications depreciate the quality of the patient's life and often become the cause of death. The ethanolic extract of *Oroxylum indicum* Kurz, which includes chrysin, inhibits the activities of α -glucosidase, thus decreasing glucose absorption in blood. It also induces GLUT-4 translocation in 3T3-L1 adipocyte cells, suggesting an increase of glucose uptake into those cells [28]. Several studies showed that chrysin has hypoglycemic effects on diabetic mice [29, 30]. Pancreatic beta cells, the function of which is important to prevent diabetes mellitus, are protected by the antioxidant activity of chrysin [31]. The antioxidant effect of chrysin can assuage the complications of diabetes. Chrysin decreases malondialdehyde and increases CAT, SOD, and glutathione. Its effect ameliorates cognitive deficits [32] and renal dysfunction [33] in diabetic animal models. Chrysin decreases total cholesterol, triglyceride, and low-density lipoprotein in streptozotocin-nicotinamide induced diabetic rats [34]. Nitric oxide-releasing chrysin attenuates diabetes-induced

complications [35–38]. Because of these activities, chrysin derivatives have been synthesized for development as anti-diabetes agents [38].

2.4. Effect on AIDS. Chrysin is known to inhibit casein kinase II involved HIV-1 transcription [39] and to suppress HIV replication in H9 cells [40]. Chrysin inhibits HIV expression in OM-10.1 cells or ACH-2 cells treated with TNF- α or phorbol myristate acetate (PMA) and 8E5 cultures [41]. Thus, chrysin has anti-HIV activity [41, 42].

2.5. Effect on Aging. Physiological functions degrade with advancing years. Among these functions, synthesis of sex hormones is important in the development of reproductive organs and maintenance of sexual function. With age, sex hormones decline and sexual function is enervated. Chrysin stimulates cyclic AMP-induced steroidogenesis in Leydig tumor cells and increases the expression of steroidogenic acute regulatory protein [43]. Moreover, chrysin ameliorates sexual functions in 2-year-old male rats, suggesting that chrysin can inhibit aromatase activities [44]. On the other hand, oral administration of chrysin to immature rats did not change sex hormone-induced uterine growth [45]. Urinary testosterone level was also measured in sportsmen drinking propolis including chrysin because aromatase inhibition can trigger the conversion of testosterone into estrogen. However, oral supplementation of propolis did not alter urinary testosterone levels [46]. These results may be due to poor absorption or bioavailability of chrysin *in vivo*. Nevertheless, chrysin was recently utilized as a testosterone booster supplement for bodybuilders and athletes [47].

Aged mouse brain shows memory declines, but chrysin prevents age-related cognitive decline by mitigating the decrease of brain-derived neurotrophic factor and ROS in the prefrontal cortex and hippocampus of aged mice [48].

Skin aging is also a matter of great interest. Ultraviolet (UV) exposure is a risk factor for skin aging. In particular, ROS promote photoaging by UV and induce cell damage. So ROS accumulation is observed in the aging process. Matrix metalloproteinase level is also increased by ROS. The antioxidant effect of chrysin inhibits the expression of matrix metalloproteinase and prevents UV-induced skin aging [49–51].

2.6. Effect on Cancer. Chrysin, a component of natural products, shows anticancer activities in various cancer cell lines [52, 53]. Several studies on chrysin have sought to explain the mechanisms of its anticancer effects, which include inhibition of the PI3K/Akt pathway, activation of caspase-3 and caspase-8 [54], and depletion of cellular glutathione [55]. Chrysin also increases mitochondrial membrane depolarization, Bax, and cleaved-PARP levels in cervical cancer cell lines [56]. Chrysin activates the transcription pathway mediated by TNF- α and TNF- β *via* aryl hydrocarbon receptor in colorectal cancer cells [57]. Chrysin, as an HDAC inhibitor, arrests the cell cycle through induction of p21 [58, 59] and then suppresses cellular proliferation. Also, chrysin as an aromatase inhibitor potentially reduces tumor growth in

estrogen receptor-positive breast cancer MCF-7 cells [60]. Chrysin derivatives have been synthesized and evaluated in the development of anticancer drugs [61].

In chemotherapy, metastasis is a problem that needs to be solved. Matrix metalloproteinase-9 (MMP-9) plays a key role in the metastatic cell invasion. Chrysin inhibits MMP-9 expression via suppression of ERK and JNK pathways in gastric cancer cells [62]. These activities of chrysin are of interest for its application in the pharmaceutical field. Furthermore, up to 3 g/day of chrysin showed no toxicity [47]. Although its advantages are attractive, chrysin has weaker therapeutic efficacy than commercial anticancer drugs. Generally, chrysin is ingested as a dietary food and utilized as a complementary medicine. Recently, the combination of chrysin and anticancer drug was shown to enhance cytotoxicity in various cancer cell lines and to be devoid of toxicity to normal cells. In human lung cancer H460 cell lines, chrysin improved the anticancer efficacy of doxorubicin and cisplatin by depletion of glutathione [63, 64]. In Hep G2 cells, the combination of chrysin and cisplatin enhanced p53 levels and induced apoptosis [65]. Also, chrysin increased the responsiveness in adriamycin-resistant cancer cells, indicating that chrysin could be developed as a chemosensitizer [66]. Moreover, the combination of chrysin and 1, 2, 3, 4, 6-penta-O-galloyl- β -D-glucose suppressed tumor growth through the reduction of S-phase kinase-associated protein 2 and low-density lipoprotein receptor-related protein 6 in triple-negative breast cancer [67].

3. Improvement Strategies for Chrysin

Although the bioactive effects of chrysin are diverse, its medicinal application is limited. One of the reasons is that chrysin has poor solubility as well as rapid metabolism and excretion [68]; the bioavailability of chrysin therefore needs to be enhanced. Nanoscale natural products are emerging as a good strategy. The nanoscale modification increases the ratio of surface area to volume and thus may improve solubility.

Bottom-up manufacturing method involves assembly of a nanoscale structure from small molecules (e.g., organic synthesis and self-assembly on protein) [69]. To improve the activities of chrysin, chemical conjugation with other chemicals was performed. Conjugation of chrysin with indole and barbituric acid increased the anti-inflammatory activity above that of chrysin itself [70]. Organogermanium had antioxidative activity like chrysin [71, 72]. And conjugation of chrysin-organogermanium had synergistic antioxidant effects and enhanced anticancer effects through apoptosis-associated mitochondrial function and antiangiogenesis [73]. Selenium containing chrysin showed significant cytotoxicity with 18-fold lower IC_{50} than that of chrysin. Moreover, the cytotoxic activity of selenium containing chrysin was superior to that of cisplatin, a commercial anticancer drug [74]. These results suggest that chrysin and other chemicals that have similar biological activity elicit increasing therapeutic efficacy with conjugation.

The other method for overcoming the disadvantages of chrysin is the utilization of a drug delivery system (DDS).

DDS have been used to solubilize a drug or modify the properties of a drug. Furthermore, DDS could be used to accumulate encapsulated drug at a target site (e.g., tumor). Nanoscale carriers include a drug reach and accumulate in tumor tissue much more than in normal tissues through the enhanced permeability and retention (EPR) effect [75]. Generally, this is called passive targeting. Recently, researchers have been concerned about manipulating nanoscale carriers in order to control drug release at the desired target site. Tumor specific antibodies or ligands are utilized in addition to the tumor microenvironment in order to achieve the active targeted delivery of drug. Eventually, DDS enhance the final concentration of drug at targeted site and improve the drug bioavailability. The technology of nanoscale modification as DDS is applied to infectious diseases as well as cancer therapy [76]. Use of natural products including chrysin as encapsulated materials has increased. Plant- or microorganism-derived materials are known to have biological activities and low toxicity compared to commercial drugs [77]. So natural products have been utilized as complementary medicine or preventive medicine. Recently, it was reported that nanoscale natural products are prospects for homeopathic medicine [69, 78–80]. Chrysin is also a good candidate for homeopathic medicine.

A successful strategy includes the selection of suitable carriers that could encapsulate the respective drugs. Based on the literature analysis, DDS for chrysin have utilized liposome [13], micelles [81], and nanoparticles [82–84] as carriers. Until now, chrysin-incorporated polymer as a nanoscale medicine was made from poly(ϵ -caprolactone) (PCL), polylactide-glycolic acid (PLGA), and polyethylene glycol (PEG). By improving the drug-loading contents, chrysin modified polymer increased chemotherapeutic efficacy. Chrysin interacted with PEG-PCL and formed polymer micelles composed of a single layer. With solubilization of chrysin, the micelle enhanced doxorubicin-induced cytotoxicity [81]. Moreover, chrysin was bound to the terminal group of methoxy PEG (mPEG) and doxorubicin was incorporated into mPEG-chrysin conjugate [82]. In micelles modified with chrysin, the chain lengths of their components were important. So mPEG (2 k)-PCL (5 k)-chrysin micelles were optimized to maximize the anticancer effect *in vitro* [85]. Chrysin has been used in attempts to enhance chemotherapeutic efficacy in various cancer cell lines.

To reduce the toxicity, carriers should be degradable in the body. One such carrier is PLGA-PEG, an FDA-approved polymer. Chrysin encapsulated into PLGA-PEG exhibited increased solubility and cytotoxicity in breast cancer T47D cells [83, 84]. The IC_{50} s of PLGA-PEG with chrysin and pure chrysin were 44.8 and 46.7 μ M, respectively, in T47D cells [66]. Moreover, PLGA-PEG with chrysin decreased cyclin D1, a protooncogene, more than pure chrysin [66]. In Zarghami et al.'s study [83, 86], chrysin-curcumin in PLGA-PEG also inhibited the proliferation of breast cancer cells by decreasing cyclin D1 expression. This result with this technology suggests that bioavailability of chrysin is improved by PLGA-PEG [86].

Until now, chrysin has been modified for anticancer therapy in most studies, but various nanoparticles including

TABLE 1: Summary of modified chrysin for improvement strategies.

Methods	Structure	Pharmaceutical application	Ref. number
Conjugation	Chrysin-indole-barbituric acid	Anti-inflammatory activity	[70]
	Chrysin-organogermanium	Antioxidant activity Anticancer effect	[71–73]
	Chrysin-selenium	Anticancer effect	[74]
Encapsulation	Liposome	Anticancer effect	[22]
	Micelle (PEG-PCL)	Enhancement of chemotherapeutic efficacy	[81]
	Nanoparticles (PLGA-PEG)	Anticancer effect	[82–84]
	Nanoparticles (PLGA)	Prevention of <i>S. Typhimurium</i> infection	[87]

chrysin, have the potential to be used for other applications. For example, PLGA-honeybee, a complex of chrysin and other components, was utilized for prevention of *S. Typhimurium* infection [87].

4. Conclusions

The technology of nanoscale modification could overcome obstacles in the development of functional dietary supplements and medicines. Nanoscale material changes the original material's physicochemical properties, (especially, solubility). In this review, chrysin is described as a good example of nanoscale modification. Chrysin, a natural flavonoid, possesses various biological activities and shows promise as a complementary medicine. However, the limitations of chrysin (poor solubility in water and low stability in the body) are a hurdle in terms of application. To enhance the bioavailability, chemical conjugation using bottom-up manufacturing and encapsulation using nanoparticles were designed and applied (Table 1). These trials could be developed for the commercial exploitation of chrysin. Hereafter nanoscale modification could be increased in the pharmaceutical field, although scale-up processing and quality control remain to be solved.

Abbreviations

TNF:	Tumor necrosis factor
ROS:	Reactive oxygen species
SOD:	Superoxide dismutase
GPx:	Glutathione peroxidase
CAT:	Catalase
PPAR:	Peroxisome proliferator-activated receptor
PMA:	Phorbol myristate acetate
UV:	Ultraviolet
HIV:	Human immunodeficiency virus
HDAC:	Histone deacetylase
MMP-9:	Matrix metalloproteinase-9
PEG:	Polyethylene glycol
PLGA:	Poly(lactic-glycolic acid)
PCL:	Poly- ϵ -caprolactone
DDS:	Drug delivery system.

Competing Interests

The author declares that there are no competing interests.

Acknowledgments

This work was supported by the Duksung Women's University Research Grants of 2014 (300000211).

References

- [1] C. Wolfman, H. Viola, A. Paladini, F. Dajas, and J. H. Medina, "Possible anxiolytic effects of chrysin, a central benzodiazepine receptor ligand isolated from *Passiflora coerulea*," *Pharmacology, Biochemistry and Behavior*, vol. 47, no. 1, pp. 1–4, 1994.
- [2] E. Brown, N. S. Hurd, S. McCall, and T. E. Ceremuga, "Evaluation of the anxiolytic effects of chrysin, a *Passiflora incarnata* extract, in the laboratory rat," *AANA Journal*, vol. 75, no. 5, pp. 333–337, 2007.
- [3] L.-J. Chen, D. E. Games, and J. Jones, "Isolation and identification of four flavonoid constituents from the seeds of *Oroxylum indicum* by high-speed counter-current chromatography," *Journal of Chromatography A*, vol. 988, no. 1, pp. 95–105, 2003.
- [4] Harminder, V. Singh, and A. K. Chaudhary, "A review on the taxonomy, ethnobotany, chemistry and pharmacology of *Oroxylum indicum* vent," *Indian Journal of Pharmaceutical Sciences*, vol. 73, no. 5, pp. 483–490, 2011.
- [5] P. Zanolì, R. Avallone, and M. Baraldi, "Behavioral characterization of the flavonoids apigenin and chrysin," *Fitoterapia*, vol. 71, no. 1, pp. S117–S123, 2000.
- [6] R. Anandhi, T. Annadurai, T. S. Anitha et al., "Antihypercholesterolemic and antioxidative effects of an extract of the oyster mushroom, *Pleurotus ostreatus*, and its major constituent, chrysin, in Triton WR-1339-induced hypercholesterolemic rats," *Journal of Physiology and Biochemistry*, vol. 69, no. 2, pp. 313–323, 2013.
- [7] M. Debiaggi, F. Tateo, L. Pagani, M. Luini, and E. Romero, "Effects of propolis flavonoids on virus infectivity and replication," *Microbiologica*, vol. 13, no. 3, pp. 207–213, 1990.
- [8] Z. Qiao and R. Chen, "Isolation and identification of antibiotic constituents of propolis from Henan," *Zhongguo Zhong Yao Za Zhi*, vol. 16, no. 8, pp. 481–512, 1991.
- [9] I. Martos, F. Ferreres, and F. A. Tomás-Barberán, "Identification of flavonoid markers for the botanical origin of *Eucalyptus*

- honey," *Journal of Agricultural and Food Chemistry*, vol. 48, no. 5, pp. 1498–1502, 2000.
- [10] A. Rauf, R. Khan, M. Raza et al., "Suppression of inflammatory response by chrysin, a flavone isolated from *Potentilla evestita* Th. Wolf. in silico predictive study on its mechanistic effect," *Fitoterapia*, vol. 103, pp. 129–135, 2015.
- [11] G. K. Harris, Y. Qian, S. S. Leonard, D. C. Sbarra, and X. Shi, "Luteolin and chrysin differentially inhibit cyclooxygenase-2 expression and scavenge reactive oxygen species but similarly inhibit prostaglandin-E₂ formation in RAW 264.7 cells," *Journal of Nutrition*, vol. 136, no. 6, pp. 1517–1521, 2006.
- [12] Y. Bae, S. Lee, and S.-H. Kim, "Chrysin suppresses mast cell-mediated allergic inflammation: involvement of calcium, caspase-1 and nuclear factor- κ B," *Toxicology and Applied Pharmacology*, vol. 254, no. 1, pp. 56–64, 2011.
- [13] E. R. Kasala, L. N. Bodduluru, R. M. Madana, K. V. Athira, R. Gogoi, and C. C. Barua, "Chemopreventive and therapeutic potential of chrysin in cancer: mechanistic perspectives," *Toxicology Letters*, vol. 233, no. 2, pp. 214–225, 2015.
- [14] W. Dou, J. Zhang, E. Zhang et al., "Chrysin ameliorates chemically induced colitis in the mouse through modulation of a PXR/NF- κ B signaling pathway," *Journal of Pharmacology and Experimental Therapeutics*, vol. 345, no. 3, pp. 473–482, 2013.
- [15] M. U. Rehman, M. Tahir, A. Q. Khan et al., "Chrysin suppresses renal carcinogenesis via amelioration of hyperproliferation, oxidative stress and inflammation: plausible role of NF- κ B," *Toxicology Letters*, vol. 216, no. 2-3, pp. 146–158, 2013.
- [16] M. U. Rehman, N. Ali, S. Rashid et al., "Alleviation of hepatic injury by chrysin in cisplatin administered rats: probable role of oxidative and inflammatory markers," *Pharmacological Reports*, vol. 66, no. 6, pp. 1050–1059, 2014.
- [17] S. Lee, Y.-J. Kim, S. Kwon et al., "Inhibitory effects of flavonoids on TNF- α -induced IL-8 gene expression in HEK 293 cells," *BMB Reports*, vol. 42, no. 5, pp. 265–270, 2009.
- [18] J. Xiao, H. Zhai, Y. Yao et al., "Chrysin attenuates experimental autoimmune neuritis by suppressing immuno-inflammatory responses," *Neuroscience*, vol. 262, pp. 156–164, 2014.
- [19] X. Feng, H. Qin, Q. Shi et al., "Chrysin attenuates inflammation by regulating M1/M2 status via activating PPAR γ ," *Biochemical Pharmacology*, vol. 89, no. 4, pp. 503–514, 2014.
- [20] B. H. Ali, S. A. Adham, M. Al Za'abi et al., "Ameliorative effect of chrysin on adenine-induced chronic kidney disease in rats," *PLoS ONE*, vol. 10, no. 4, Article ID e0125285, 2015.
- [21] T. Kilic, O. Ciftci, A. Cetin, and H. Kahraman, "Preventive effect of chrysin on bleomycin-induced lung fibrosis in rats," *Inflammation*, vol. 37, no. 6, pp. 2116–2124, 2014.
- [22] Z. Zhang, G. Li, S. S. W. Szeto et al., "Examining the neuroprotective effects of protocatechuic acid and chrysin on in vitro and in vivo models of Parkinson disease," *Free Radical Biology and Medicine*, vol. 84, pp. 331–343, 2015.
- [23] Y. Yao, L. Chen, J. Xiao et al., "Chrysin protects against focal cerebral ischemia/reperfusion injury in mice through attenuation of oxidative stress and inflammation," *International Journal of Molecular Sciences*, vol. 15, no. 11, pp. 20913–20926, 2014.
- [24] R. Anandhi, P. A. Thomas, and P. Geraldine, "Evaluation of the anti-atherogenic potential of chrysin in Wistar rats," *Molecular and Cellular Biochemistry*, vol. 385, no. 1-2, pp. 103–113, 2014.
- [25] B. Bekdeşer, N. Durusoy, M. Özyürek, K. Güçlü, and R. Apak, "Optimization of microwave-assisted extraction of polyphenols from herbal teas and evaluation of their in vitro hypochlorous acid scavenging activity," *Journal of Agricultural and Food Chemistry*, vol. 62, no. 46, pp. 11109–11115, 2014.
- [26] S. Wang, X. Zhang, M. Liu et al., "Chrysin inhibits foam cell formation through promoting cholesterol efflux from RAW264.7 macrophages," *Pharmaceutical Biology*, vol. 53, no. 10, pp. 1481–1487, 2015.
- [27] S. B. Lotito and B. Frei, "Dietary flavonoids attenuate tumor necrosis factor α -induced adhesion molecule expression in human aortic endothelial cells. Structure-function relationships and activity after first pass metabolism," *The Journal of Biological Chemistry*, vol. 281, no. 48, pp. 37102–37110, 2006.
- [28] B. Dinda, I. Silsarma, M. Dinda, and P. Rudrapaul, "*Oroxylum indicum* (L.) Kurz, an important Asian traditional medicine: from traditional uses to scientific data for its commercial exploitation," *Journal of Ethnopharmacology*, vol. 161, pp. 255–278, 2015.
- [29] J.-S. Shin, K.-S. Kim, M.-B. Kim, J.-H. Jeong, and B.-K. Kim, "Synthesis and hypoglycemic effect of chrysin derivatives," *Bioorganic and Medicinal Chemistry Letters*, vol. 9, no. 6, pp. 869–874, 1999.
- [30] K. Batumalaie, R. Qvist, K. M. O. Yusof, I. S. H. Ismail, and S. D. E. Sekaran, "The antioxidant effect of the Malaysian Gelam honey on pancreatic hamster cells cultured under hyperglycemic conditions," *Clinical and Experimental Medicine*, vol. 14, no. 2, pp. 185–195, 2014.
- [31] T. Lapidot, M. D. Walker, and J. Kanner, "Antioxidant and prooxidant effects of phenolics on pancreatic β -cells in vitro," *Journal of Agricultural and Food Chemistry*, vol. 50, no. 25, pp. 7220–7225, 2002.
- [32] R. Li, A. Zang, L. Zhang et al., "Chrysin ameliorates diabetes-associated cognitive deficits in Wistar rats," *Neurological Sciences*, vol. 35, no. 10, pp. 1527–1532, 2014.
- [33] A. Ahad, A. A. Ganai, M. Mujeeb, and W. A. Siddiqui, "Chrysin, an anti-inflammatory molecule, abrogates renal dysfunction in type 2 diabetic rats," *Toxicology and Applied Pharmacology*, vol. 279, no. 1-7, 2014.
- [34] M. Torres-Piedra, R. Ortiz-Andrade, R. Villalobos-Molina et al., "A comparative study of flavonoid analogues on streptozotocin-nicotinamide induced diabetic rats: quercetin as a potential antidiabetic agent acting via 11β -Hydroxysteroid dehydrogenase type 1 inhibition," *European Journal of Medicinal Chemistry*, vol. 45, no. 6, pp. 2606–2612, 2010.
- [35] H. M. El-Bassossy, S. M. Abo-Warda, and A. Fahmy, "Chrysin and luteolin attenuate diabetes-induced impairment in endothelial-dependent relaxation: effect on lipid profile, AGEs and NO generation," *Phytotherapy Research*, vol. 27, no. 11, pp. 1678–1684, 2013.
- [36] X.-Q. Zou, S.-M. Peng, C.-P. Hu, L.-F. Tan, H.-W. Deng, and Y.-J. Li, "Furoxan nitric oxide donor coupled chrysin derivatives: synthesis and vasculoprotection," *Bioorganic and Medicinal Chemistry Letters*, vol. 21, no. 4, pp. 1222–1226, 2011.
- [37] X.-Q. Zou, S.-M. Peng, C.-P. Hu et al., "Synthesis, characterization and vasculoprotective effects of nitric oxide-donating derivatives of chrysin," *Bioorganic and Medicinal Chemistry*, vol. 18, no. 9, pp. 3020–3025, 2010.
- [38] Q.-Q. Wang, N. Cheng, W.-B. Yi, S.-M. Peng, and X.-Q. Zou, "Synthesis, nitric oxide release, and α -glucosidase inhibition of nitric oxide donating apigenin and chrysin derivatives," *Bioorganic and Medicinal Chemistry*, vol. 22, no. 5, pp. 1515–1521, 2014.

- [39] E. De Clercq, "Current lead natural products for the chemotherapy of human immunodeficiency virus (HIV) infection," *Medicinal Research Reviews*, vol. 20, no. 5, pp. 323–349, 2000.
- [40] C.-Q. Hu, K. E. Chen, Q. Shi, R. E. Kilkuskie, Y.-C. Cheng, and K.-H. Lee, "Anti-aids agents, 10. Acacetin-7-O- β -D-galactopyranoside, an anti-HIV principle from *Chrysanthemum morifolium* and a structure-activity correlation with some related flavonoids," *Journal of Natural Products*, vol. 57, no. 1, pp. 42–51, 1994.
- [41] J. W. Critchfield, S. T. Butera, and T. M. Folks, "Inhibition of HIV activation in latently infected cells by flavonoid compounds," *AIDS Research and Human Retroviruses*, vol. 12, no. 1, pp. 39–46, 1996.
- [42] H.-K. Wang, Y. Xia, Z.-Y. Yang, S. L. Morris Natschke, and K.-H. Lee, "Recent advances in the discovery and development of flavonoids and their analogues as antitumor and anti-HIV agents," *Advances in Experimental Medicine and Biology*, vol. 439, pp. 191–225, 1998.
- [43] K. Jana, X. Yin, R. B. Schiffer et al., "Chrysin, a natural flavonoid enhances steroidogenesis and steroidogenic acute regulatory protein gene expression in mouse Leydig cells," *Journal of Endocrinology*, vol. 197, no. 2, pp. 315–323, 2008.
- [44] K. Dhawan, S. Kumar, and A. Sharma, "Beneficial effects of chrysin and benzoflavone on virility in 2-year-old male rats," *Journal of Medicinal Food*, vol. 5, no. 1, pp. 43–48, 2002.
- [45] N. Saarinen, S. C. Joshi, M. Ahotupa et al., "No evidence for the in vivo activity of aromatase-inhibiting flavonoids," *Journal of Steroid Biochemistry and Molecular Biology*, vol. 78, no. 3, pp. 231–239, 2001.
- [46] C. Gambelunghe, R. Rossi, M. Sommavilla et al., "Effects of chrysin on urinary testosterone levels in human males," *Journal of Medicinal Food*, vol. 6, no. 4, pp. 387–390, 2003.
- [47] P. J. Tobin, P. Beale, L. Noney, S. Liddell, L. P. Rivory, and S. Clarke, "A pilot study on the safety of combining chrysin, a non-absorbable inducer of UGT1A1, and irinotecan (CPT-11) to treat metastatic colorectal cancer," *Cancer Chemotherapy and Pharmacology*, vol. 57, no. 3, pp. 309–316, 2006.
- [48] L. C. Souza, M. S. Antunes, C. B. Filho et al., "Flavonoid Chrysin prevents age-related cognitive decline via attenuation of oxidative stress and modulation of BDNF levels in aged mouse brain," *Pharmacology Biochemistry and Behavior*, vol. 134, pp. 22–30, 2015.
- [49] G.-S. Sim, B.-C. Lee, S. C. Ho et al., "Structure activity relationship of antioxidative property of flavonoids and inhibitory effect on matrix metalloproteinase activity in UVA-irradiated human dermal fibroblast," *Archives of Pharmacal Research*, vol. 30, no. 3, pp. 290–298, 2007.
- [50] K. V. Anand, M. S. Mohamed Jaabir, P. A. Thomas, and P. Geraldine, "Protective role of chrysin against oxidative stress in d-galactose-induced aging in an experimental rat model," *Geriatrics and Gerontology International*, vol. 12, no. 4, pp. 741–750, 2012.
- [51] N.-L. Wu, J.-Y. Fang, M. Chen, C.-J. Wu, C.-C. Huang, and C.-F. Hung, "Chrysin protects epidermal keratinocytes from UVA- and UVB-induced damage," *Journal of Agricultural and Food Chemistry*, vol. 59, no. 15, pp. 8391–8400, 2011.
- [52] B. Y. Khoo, S. L. Chua, and P. Balaram, "Apoptotic effects of chrysin in human cancer cell lines," *International Journal of Molecular Sciences*, vol. 11, no. 5, pp. 2188–2199, 2010.
- [53] M. Mandal and S. K. Jaganathan, "Antiproliferative effects of honey and of its polyphenols: a review," *Journal of Biomedicine and Biotechnology*, vol. 2009, Article ID 830616, 13 pages, 2009.
- [54] D. Sawicka, H. Car, M. H. Borawska, and J. Nikliński, "The anti-cancer activity of propolis," *Folia Histochemica et Cytobiologica*, vol. 50, no. 1, pp. 25–37, 2012.
- [55] R. Kachadourian and B. J. Day, "Flavonoid-induced glutathione depletion: potential implications for cancer treatment," *Free Radical Biology and Medicine*, vol. 41, no. 1, pp. 65–76, 2006.
- [56] S. Laishram, D. S. Moirangthem, J. C. Borah et al., "Chrysin rich *Scutellaria discolor* Colebr. induces cervical cancer cell death via the induction of cell cycle arrest and caspase-dependent apoptosis," *Life Sciences*, vol. 143, pp. 105–113, 2015.
- [57] S. M. Ronnekleiv-Kelly, M. Nukaya, C. J. Díaz-Díaz et al., "Aryl hydrocarbon receptor-dependent apoptotic cell death induced by the flavonoid chrysin in human colorectal cancer cells," *Cancer Letters*, vol. 370, no. 1, pp. 91–99, 2016.
- [58] J. R. Araújo, P. Gonçalves, and F. Martel, "Chemopreventive effect of dietary polyphenols in colorectal cancer cell lines," *Nutrition Research*, vol. 31, no. 2, pp. 77–87, 2011.
- [59] M. Pal-Bhadra, M. J. Ramaiah, T. L. Reddy et al., "Plant HDAC inhibitor chrysin arrest cell growth and induce p21WAF1 by altering chromatin of STAT response element in A375 cells," *BMC Cancer*, vol. 12, article 180, 2012.
- [60] J. A. van Meeuwen, N. Korthagen, P. C. de Jong, A. H. Piersma, and M. van den Berg, "(Anti)estrogenic effects of phytochemicals on human primary mammary fibroblasts, MCF-7 cells and their co-culture," *Toxicology and Applied Pharmacology*, vol. 221, no. 3, pp. 372–383, 2007.
- [61] H. A. Mohammed, L. A. Ba, T. Burkholz et al., "Facile synthesis of chrysin-derivatives with promising activities as aromatase inhibitors," *Natural Product Communications*, vol. 6, no. 1, pp. 31–34, 2011.
- [62] Y. Xia, S. Lian, P. N. Khoi et al., "Chrysin inhibits tumor promoter-induced MMP-9 expression by blocking AP-1 via suppression of ERK and JNK pathways in gastric cancer cells," *PLoS ONE*, vol. 10, no. 4, Article ID e0124007, 2015.
- [63] H. M. Brechbuhl, R. Kachadourian, E. Min, D. Chan, and B. J. Day, "Chrysin enhances doxorubicin-induced cytotoxicity in human lung epithelial cancer cell lines: the role of glutathione," *Toxicology and Applied Pharmacology*, vol. 258, no. 1, pp. 1–9, 2012.
- [64] R. Kachadourian, H. M. Leitner, and B. J. Day, "Selected flavonoids potentiate the toxicity of cisplatin in human lung adenocarcinoma cells: a role for glutathione depletion," *International Journal of Oncology*, vol. 31, no. 1, pp. 161–168, 2007.
- [65] X. Li, J.-M. Huang, J.-N. Wang, X.-K. Xiong, X.-F. Yang, and F. Zou, "Combination of chrysin and cisplatin promotes the apoptosis of Hep G2 cells by up-regulating p53," *Chemico-Biological Interactions*, vol. 232, pp. 12–20, 2015.
- [66] E. R. Kasala, L. N. Bodduluru, C. C. Barua, and R. Gogoi, "Chrysin and its emerging role in cancer drug resistance," *Chemico-Biological Interactions*, vol. 236, pp. 7–8, 2015.
- [67] C. Huang, Y. J. Chen, W.-J. Chen, C.-L. Lin, Y. X. Wei, and H. C. Huang, "Combined treatment with chrysin and 1,2,3,4,6-penta-O-galloyl- β -D-glucose synergistically inhibits LRP6 and Skp2 activation in triple-negative breast cancer and xenografts," *Molecular Carcinogenesis*, vol. 54, no. 12, pp. 1613–1625, 2015.
- [68] T. Walle, Y. Otake, J. A. Brubaker, U. K. Walle, and P. V. Halushka, "Disposition and metabolism of the flavonoid chrysin in normal volunteers," *British Journal of Clinical Pharmacology*, vol. 51, no. 2, pp. 143–146, 2001.
- [69] I. R. Bell, B. Sarter, M. Koithan et al., "Integrative nanomedicine: treating cancer with nanoscale natural products," *Global Advances in Health and Medicine*, vol. 3, no. 1, pp. 36–53, 2014.

- [70] P. Singh, J. Kaur, G. Singh, and R. Bhatti, "Triblock conjugates: identification of a highly potent antiinflammatory agent," *Journal of Medicinal Chemistry*, vol. 58, no. 15, pp. 5989–6001, 2015.
- [71] J. Jiang, S. Yao, H.-H. Cai, P.-H. Yang, and J. Cai, "Synthesis and synergetic effects of chrysin-organogermanium (IV) complex as potential anti-oxidant," *Bioorganic and Medicinal Chemistry Letters*, vol. 23, no. 20, pp. 5727–5732, 2013.
- [72] F. Yang, H. Jin, J. Pi et al., "Anti-tumor activity evaluation of novel chrysin-organogermanium(IV) complex in MCF-7 cells," *Bioorganic and Medicinal Chemistry Letters*, vol. 23, no. 20, pp. 5544–5551, 2013.
- [73] F. Yang, L. Gong, H. Jin et al., "Chrysin-organogermanium (IV) complex induced Colo205 cell apoptosis-associated mitochondrial function and anti-angiogenesis," *Scanning*, vol. 37, no. 4, pp. 246–257, 2015.
- [74] I. L. Martins, C. Charneira, V. Gandin et al., "Selenium-containing chrysin and quercetin derivatives: attractive scaffolds for cancer therapy," *Journal of Medicinal Chemistry*, vol. 58, no. 10, pp. 4250–4265, 2015.
- [75] Y. Matsumura and H. Maeda, "A new concept for macromolecular therapeutics in cancer chemotherapy: mechanism of tumorotropic accumulation of proteins and the antitumor agent smancs," *Cancer Research*, vol. 46, no. 12, part 1, pp. 6387–6392, 1986.
- [76] I. R. Bell, G. E. Schwartz, N. N. Boyer, M. Koithan, and A. J. Brooks, "Advances in integrative nanomedicine for improving infectious disease treatment in public health," *European Journal of Integrative Medicine*, vol. 5, no. 2, pp. 126–140, 2013.
- [77] R. Watkins, L. Wu, C. Zhang, R. M. Davis, and B. Xu, "Natural product-based nanomedicine: recent advances and issues," *International Journal of Nanomedicine*, vol. 10, pp. 6055–6074, 2015.
- [78] I. R. Bell, J. A. Ives, and W. B. Jonas, "Nonlinear effects of nanoparticles: biological variability from hormetic doses, small particle sizes, and dynamic adaptive interactions," *Dose-Response*, vol. 12, no. 2, pp. 202–232, 2014.
- [79] I. R. Bell and G. E. Schwartz, "Adaptive network nanomedicine: an integrated model for homeopathic medicine," *Frontiers in Bioscience*, vol. 5, no. 2, pp. 685–708, 2013.
- [80] I. R. Bell, B. Sarter, L. J. Standish, P. Banerji, and P. Banerji, "Low doses of traditional nanophytomedicines for clinical treatment: manufacturing processes and nonlinear response patterns," *Journal of Nanoscience and Nanotechnology*, vol. 15, no. 6, pp. 4021–4038, 2015.
- [81] Y. Liang, X. Deng, L. Zhang et al., "Terminal modification of polymeric micelles with π -conjugated moieties for efficient anticancer drug delivery," *Biomaterials*, vol. 71, pp. 1–10, 2015.
- [82] H. Zheng, S. Li, Y. Pu, Y. Lai, B. He, and Z. Gu, "Nanoparticles generated by PEG-Chrysin conjugates for efficient anticancer drug delivery," *European Journal of Pharmaceutics and Biopharmaceutics*, vol. 87, no. 3, pp. 454–460, 2014.
- [83] E. Anari, A. Akbarzadeh, and N. Zarghami, "Chrysin-loaded PLGA-PEG nanoparticles designed for enhanced effect on the breast cancer cell line," *Artificial Cells, Nanomedicine, and Biotechnology*, 2015.
- [84] S. Mohammadinejad, A. Akbarzadeh, M. Rahmati-Yamchi et al., "Preparation and evaluation of chrysin encapsulated in PLGA-PEG nanoparticles in the T47-D breast cancer cell line," *Asian Pacific Journal of Cancer Prevention*, vol. 16, no. 9, pp. 3753–3758, 2015.
- [85] X. P. Yan Liang, Y. Chen, X. Deng et al., "Chain length effect on drug delivery of chrysin modified mPEG-PCL micelles," *RSC Advances*, vol. 73, no. 5, pp. 59014–59021, 2015.
- [86] N. Zarghami, M. Mohammadinejad, A. Akbarzadeh, Y. Pilehvar-Soltanahmadi, and F. Zarghami, "Synergistic effects of chrysin-curcumin loaded in PLGA-PEG nanoparticles on inhibiting breast cancer cell line growth," *International Science Index, Chemical and Molecular Engineering*, vol. 2, no. 12, 2015.
- [87] J.-A. Lee, B.-G. Jung, T.-H. Kim et al., "Poly d,l-lactide-co-glycolide (PLGA) nanoparticle-encapsulated honeybee (*Apis mellifera*) venom promotes clearance of *Salmonella enterica* serovar Typhimurium infection in experimentally challenged pigs through the up-regulation of T helper type 1 specific immune responses," *Veterinary Immunology and Immunopathology*, vol. 161, no. 3-4, pp. 193–204, 2014.

Research Article

Development of a Time-Dependent Friction Model for Frictional Aging at the Nanoscale

Seung Yub Baek¹ and Kyungmok Kim²

¹*Department of Mechanical Design, Induk University, 2 Wolgye-dong, Nowon-gu, Seoul 139-749, Republic of Korea*

²*School of Aerospace and Mechanical Engineering, Korea Aerospace University,
76 Hanggongdaehang-ro, Deogyang-gu, Goyang-si, Gyeonggi-do 412-791, Republic of Korea*

Correspondence should be addressed to Kyungmok Kim; kkim@kau.ac.kr

Received 11 November 2015; Accepted 15 February 2016

Academic Editor: Serdal Kirmizialtin

Copyright © 2016 S. Y. Baek and K. Kim. This is an open access article distributed under the Creative Commons Attribution License, which permits unrestricted use, distribution, and reproduction in any medium, provided the original work is properly cited.

A model for describing frictional aging of silica is developed at the nanoscale. A cohesive zone is applied to the contact surface between self-mated silica materials. Strengthening of interfacial bonding during frictional aging is reproduced by increasing fracture energy of a cohesive zone. Fracture energy is expressed as a function of hold time between self-mated silica materials. Implicit finite element simulation is employed, and simulation results are compared with experimental ones found in the literature. Calculated friction evolutions with various hold times are found to be in good agreement with experimental ones. Dependence of mesh size and cohesive thickness is identified for obtaining accurate simulation result.

1. Introduction

Frictional aging is the contact phenomenon that interfacial bonding between two bodies is strengthened with increasing hold time. The strengthening of interfacial bonding is attributed to increase in the maximum frictional force. The maximum frictional force was found to increase logarithmically with hold time [1]. Frictional aging is widely observed in macroscale and nanoscale contacts [2–5]. Strength of the contact between rocks was found to increase with the age of the contact [2]. Rate-dependent friction behaviour of granular materials was studied [3]. It was observed that friction behaviour of granular materials was dependent upon humidity; the transition from velocity strengthening to velocity-weakening frictional behaviour was found under certain humid condition. The aging behaviour of a single nanoscale contact was investigated by conducting slide-hold-slide experiments with silica [4]. In a slide-hold-slide friction experiment, one body was held for certain time after the initial slip between two bodies. Slip was then induced at contact, and both frictional force and relative displacement

were measured. It was identified that measured frictional force increased with respect to hold time. Effect of oscillation on friction in nanoscale contact was studied with atomic force microscopy (AFM) measurement [5]. Small-amplitude in-plane oscillation of a tip in AFM was found to affect the kinetics of frictional aging. Despite some studies on frictional aging, little is found on simulation of frictional aging at the nanoscale due to lack of adequate description of interfacial bonding.

Cohesive zone law is a useful method for describing interfacial failure between two physical parts. Various cohesive zone models were developed and used for simulating damage such as creep, fatigue, fretting fatigue, and interfacial cracking at the macroscale and microscale [6–9]. Creep-rupture of aluminium alloys was modelled with a time-dependent bilinear cohesive zone law [6]. Fretting fatigue cracking was reproduced with a cohesive zone law using cycle-jump strategy [7]. Stress amplitude versus cycles-to-failure curves were determined with aluminium alloys. At the microscale, interfacial cracking between alumina particles was simulated with a bilinear cohesive zone law [8]. Shear

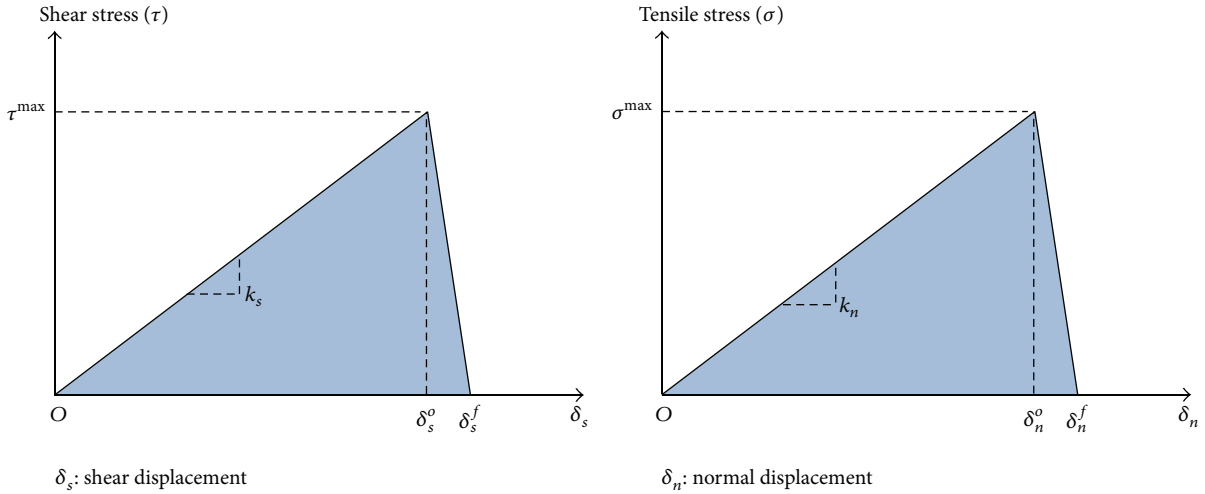


FIGURE 1: Bilinear cohesive zone law.

and normal loads representing kinetic friction between a head and a cup in a hip prosthesis were induced to an alumina microstructure. Crack initiation and propagation were simulated with a two-dimensional finite element model. Softening behaviour of aluminium alloy under pure-tension loading was modelled with a nonlinear cohesive zone law [9]. Nonlinear softening behaviour of heat-treated and non-heat-treated specimens was described with the properties of a cohesive zone.

In this study, a bilinear cohesive zone law was proposed for describing static friction and frictional aging at the nanoscale. The strengthening of interfacial bonding resulting from frictional aging was achieved with the increase in cohesive energy. A three-dimensional finite element model was generated with a thin cohesive layer. The maximum frictional force and the relative displacement between two parts were determined after calculation. Direct comparison between simulation and experimental results was then employed.

2. Time-Dependent Friction Model Using a Cohesive Zone Law

When one body is pressed by the other, interfacial bonding is formed at the contact between two bodies. Once a tangential force is induced to the body, the bonding becomes weakened. If the tangential force is sufficient to break the bonding, slip initiates at the contact. Interfacial bonding is strengthened as hold time is increased (known as frictional aging). In other words, the maximum frictional force increases with increased hold time due to strengthening of interfacial bonding.

In this study, strengthening of interfacial bonding was described with the properties of a cohesive zone (i.e., cohesive energy). A bilinear cohesive zone law was used to describe interfacial bonding between two bodies. In a bilinear cohesive zone law, cohesive strength, cohesive stiffness, and displacement at failure determine fracture behaviour of a cohesive zone. In this study, cohesive strength was assumed as frictional strength.

Figure 1 shows the proposed bilinear cohesive zone law. Once the maximum stress of a cohesive element meets (1), partial slip at contact or separation is assumed to initiate:

$$\left(\frac{\sigma}{\sigma^{\max}}\right)^2 + \left(\frac{\tau}{\tau^{\max}}\right)^2 = 1, \quad (1)$$

where σ^{\max} is the maximum tensile stress associated with pull-off adhesion strength and τ^{\max} is the maximum shear stress related to static friction.

If a displacement continues to increase after satisfying (1), stress is then reduced according to a softening curve. A softening curve is described with the damage variable (D) defined as

$$D = \frac{\delta^f (\delta^{\max} - \delta^o)}{\delta^{\max} (\delta^f - \delta^o)}, \quad (2)$$

where δ^{\max} is total displacement determined with the normal displacement (δ_n) and the shear displacement (δ_s). δ^f is the final displacement to complete failure, and δ^o is the displacement that (1) satisfied.

When D remains zero, no slip occurs at the contact without separation in the normal direction. If D is equal to unity, either full slip or complete separation occurs at the entire contact. The area within the stress-displacement curve corresponds to cohesive energy per unit area for friction and pull-off adhesion. In order to focus on friction, pull-off adhesion was excluded in this study.

It was identified from the literature that static friction between two solids increases with hold time, and time-dependent frictional force (Q^{\max}) is expressed with a simple log function [1]. The logarithmic increase of a frictional force is attributed to the deformation creep in plastic contacts:

$$Q^{\max}(t) = Q_0^{\max} + \beta \cdot P \cdot \ln(t), \quad (3)$$

where t is hold time. Q_0^{\max} is initial frictional force, P is normal force, and β is the constant.

By dividing (3) with an actual contact area (A), the maximum shear stress is given as

$$\tau^{\max}(t) = \tau_0^{\max} + \beta \cdot \sigma_c \cdot \ln(t), \quad (4)$$

where σ_c is compressive stress.

Time-dependent cohesive energy, $G(t)$, can then be derived from a bilinear cohesive law (i.e., $G(t) = 0.5 \cdot \tau^{\max}(t) \cdot \delta_s^f(t)$). Consider

$$G(t) = \frac{(\tau_0^{\max} + \beta \cdot \sigma_c \cdot \ln(t)) \cdot \delta_s^f(t)}{2}, \quad (5)$$

where $\delta_s^f(t)$ is total shear displacement leading to complete failure.

Meanwhile, the total shear displacement can be expressed with cohesive shear stiffness (k_s) and the effective relative shear displacement to failure ($\Delta\delta_s^f$):

$$\delta_s^f(t) = \frac{\tau^{\max}(t)}{k_s} + \Delta\delta_s^f. \quad (6)$$

Measured results for silica (SiO_2) showed that cohesive stiffness and the effective relative shear displacement to failure ($\Delta\delta_s^f$) were maintained as constant without regard to hold time.

Equation (5) can be rewritten as

$$G(t) = \frac{(\tau_0^{\max} + \beta \cdot \sigma_c \cdot \ln(t))^2}{2k_s} + \frac{(\tau_0^{\max} + \beta \cdot \sigma_c \cdot \ln(t))}{2} \Delta\delta_s^f. \quad (7)$$

Figure 2 shows the frictional strength with respect to hold time. It is possible to express measured frictional strength with a simple log function as presented in the literature [4]. Figure 3 shows cohesive energy of SiO_2 with respect to hold time. Markers show measured data of self-mated SiO_2 specimens, and a smooth curve denotes a calculated one with (5). Good agreement was obtained between two values of cohesive energy data.

3. Finite Element Simulation

A three-dimensional model was generated by commercial finite element software (ABAQUS®). The model consisted of a rounded tip (a radius of 15 nm), a plate, and a cohesive layer between a tip and a plate. A cohesive layer was thin and circular. The diameter ($2a$) of a cohesive zone was determined by Hertz contact theory [11]:

$$a = \left(\frac{3PR}{4E^*} \right)^{1/3}, \quad (8)$$

where $1/E^* = (1 - \nu_1^2)/E_1 + (1 - \nu_2^2)/E_2$. P is normal force, R is the radius of a rounded tip, E_1 and ν_1 are elastic modulus and Poisson's ratio of a rounded tip, and E_2 and ν_2 are elastic modulus and Poisson's ratio of a plate, respectively. Table 1

TABLE 1: Mechanical properties of silica (SiO_2) [10].

Elastic modulus (GPa)	Poisson's ratio
68.9	0.17

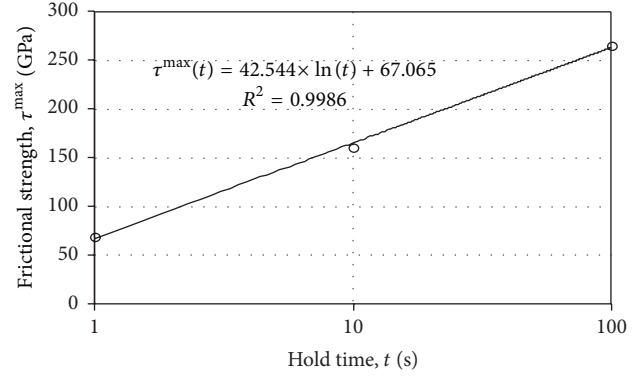


FIGURE 2: Frictional strength with respect to hold time on the semilog scale. Markers show measured data of self-mated SiO_2 specimens at a normal force of 1 nN and 60% RH [4]. A smooth line denotes a fitted curve.

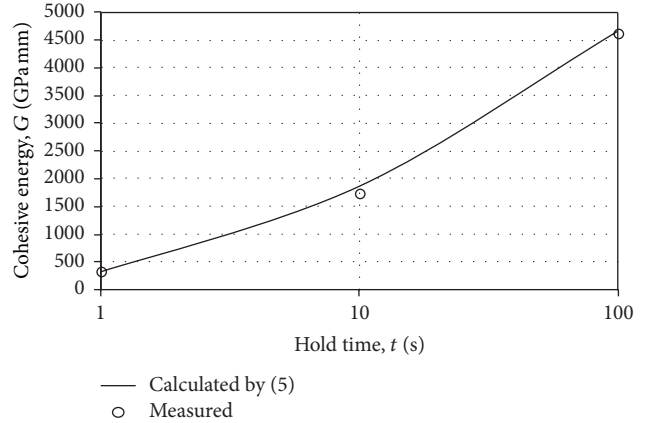


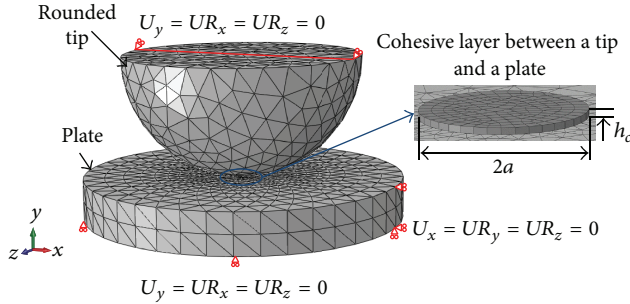
FIGURE 3: Cohesive energy of SiO_2 for describing frictional aging. Markers show measured data of self-mated silica, and a smooth curve denotes a calculated one with (5).

shows elastic modulus and Poisson's ratio of silica used in this study.

An upper surface of a cohesive part was fixed to the contact surface of a tip in all directions, while the lower one of a cohesive part was fixed to a plate. A tetragonal element type was applied to the tip and the plate; the element size was 1 nm. Parts of the tip and the plate contacted to a cohesive layer were meshed with an element of 0.1 nm. All of the cohesive layer was meshed with a hexagonal element 0.05 nm long. The thickness of a cohesive layer (h_c) was defined as 0.05 nm. Table 2 shows the mechanical properties of a cohesive layer used in this study. The cohesive stiffness, the maximum nominal stress, and the effective displacement at failure were determined on the basis of experimental data [4]. The cohesive stiffness and the effective displacement at failure were assumed to be constant regardless of hold time.

TABLE 2: Mechanical properties of a cohesive layer.

Properties	Value
Shear stiffness, k_s , (GPa·nm)	7.7
Normal stiffness, k_n , (GPa·nm)	7.7
Max. nominal shear stress after a hold time of 1 sec. (GPa)	67.1
Max. nominal tensile stress after a hold time of 1 sec. (GPa)	67.1
The effective displacement at failure, $\Delta\delta^f$, (nm)	1.2

FIGURE 4: A finite element model with boundary conditions. U and UR denote displacement and rotation, respectively.

Initial sliding in a slide-hold-slide experiment was excluded in this simulation, since the initial sliding did not greatly affect frictional strength. Pressure of 1.41 MPa (a normal force of 1 nN) was imposed to the upper surface of a tip. Then, the whole part of a tip was horizontally moved at a prescribed displacement, while the plate was fixed as shown in Figure 4.

4. Results and Verification

Implicit finite element modelling was employed to simulate frictional aging of self-mated silica. Cohesive energy presented in Figure 3 was used for describing the strengthening of bonding resulting from frictional aging. The maximum shear and normal stresses for a bilinear cohesive law were determined with time-dependent cohesive energy. After simulation, the maximum shear stress at the contact surface of a plate was recorded, along with the relative displacement between a tip and a plate. Frictional force was then calculated from the maximum shear stress.

Figure 5 shows the direct comparison between calculated and experimental frictional forces for the hold time of 1 second. Markers were measured data found in the literature [4] and a smooth curve was a calculated one. Excellent agreement was obtained between calculated and experimental contact stiffness values. In the plot, the maximum value was used for determining the coefficient of static friction. There was the difference of 11 percent between experimental and calculated values in the maximum frictional force. In addition, the decrease rate after the maximum frictional force was different.

Simulation for different hold time was employed. The effect of increased hold time in an experiment was reproduced with increase of cohesive energy presented in Figure 3.

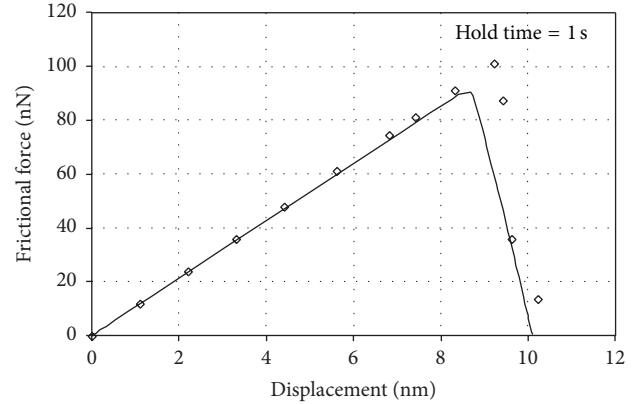


FIGURE 5: Direct comparison between measured and calculated frictional forces. Markers are measured data found in the literature [4] and a smooth curve is a calculated one.

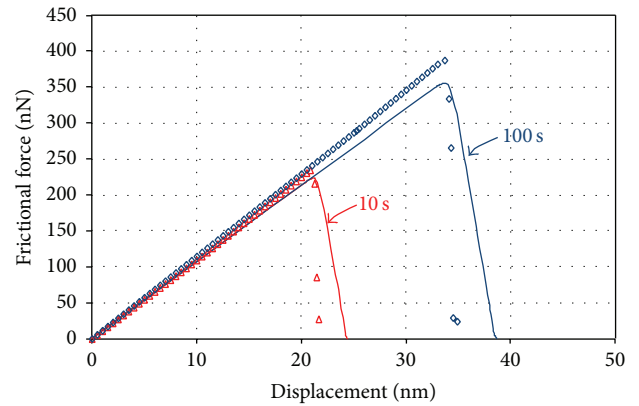


FIGURE 6: Comparison between calculated and experimental frictional forces after 10 and 100 seconds. Markers are measured data [4] and smooth curves are calculated ones.

Simulation was terminated when a cohesive zone was completely broken. Figure 6 shows calculated frictional forces after 10 and 100 seconds. A calculated frictional force for the hold time of 10 seconds was in excellent agreement with the experimental one (markers in Figure 6). However, the drop rate of the calculated force was different than that found in the experiment. The calculated maximum force for hold time of 100 seconds was 9 percent as low as the experimental one. Variance of chosen cohesive energy might be attributed to the difference in the maximum force. In this simulation, the effective displacement at failure for cohesive zone was constant without regard to hold time. This might be attributed to the difference between the drop rates of the force.

Figure 7 shows the dependence of cohesive element size in the maximum frictional force. In case the cohesive element size was 0.05 nm, the difference between measured and calculated forces remained lower than 11 percent in the maximum frictional force. If the cohesive element size was greater than 0.1 nm, the difference between measurement and calculation increased greatly (more than 17 percent). Figure 8 shows the dependence of cohesive thickness in the maximum

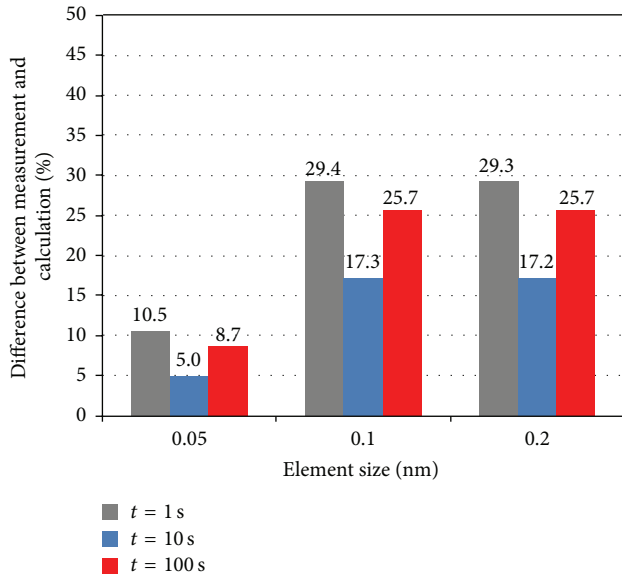


FIGURE 7: Dependence of cohesive element size in the maximum frictional force.

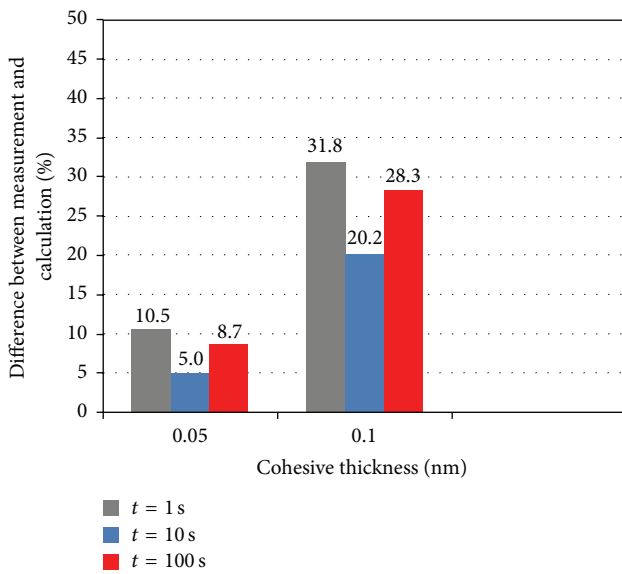


FIGURE 8: Dependence of cohesive thickness in the maximum frictional force. Cohesive element size was 0.05 nm in all cases.

frictional force; in case of a cohesive thickness of 0.1 nm and an element size of 0.05 nm, the difference between measured and calculated forces was greater than 20 percent. Figures 7 and 8 provide adequate mesh size and cohesive thickness for obtaining accurate simulation result. That is, cohesive element size and cohesive thickness need to be lower than 0.05 nm to obtain the error of 10 percent in the maximum frictional force.

In this study, a bilinear cohesive zone law was applied to the modelling of frictional aging of self-mated silica. A proposed method allows simulating the strengthening of bonding resulting from frictional aging. The transition from partial slip to full slip was simulated with the softening

of a cohesive zone law. The drop rates of the calculated frictional force after 10 and 100 seconds were somewhat different than experimental ones. Thus, further work needs to include an investigation into the difference between the drop rates. In addition, increase in contact area occurs during frictional aging. In this study, the contact area between silica materials was assumed to be constant regardless of hold time. Therefore, further modelling should include the increase in actual contact area with hold time.

5. Conclusions

The following conclusions were drawn:

- (i) It was possible to simulate static friction between self-mated silica materials with a bilinear cohesive zone at the nanoscale.
- (ii) Strengthening of interfacial bonding during frictional aging can be reproduced with the increased cohesive energy in a bilinear cohesive zone law.
- (iii) An element size of 0.05 nm and a cohesive thickness of 0.05 nm were proposed to obtain simulation results with less than 10 percent in error.

Further work needs to simulate the transition from partial slip to full slip (kinetic friction). In addition, the increase of actual contact area during frictional aging needs to be included in a model.

Nomenclature

a :	Actual contact radius
A :	Actual contact area
D :	Damage variable
E :	Modulus of elasticity
G :	Time-dependent cohesive energy
k_s :	Shear stiffness
k_n :	Normal stiffness
P :	Normal force
Q^{\max} :	Maximum frictional force
Q_0^{\max} :	Initial frictional force
R :	Radius of a rounded tip
t :	Time
δ_n :	Normal displacement
δ_s :	Shear displacement
δ_s^f :	Final displacement to complete failure
δ^{\max} :	Total displacement
δ_s^o :	Displacement at the maximum stress
δ_s^o :	Shear displacement at the maximum shear stress
δ_s^f :	Final shear displacement to complete failure
δ_n^o :	Normal displacement at the maximum tensile stress
δ_n^f :	Final normal displacement to complete failure
ν :	Poisson's ratio
σ :	Tensile stress
σ_c :	Compressive stress
σ^{\max} :	Maximum tensile stress
τ :	Shear stress
τ^{\max} :	Maximum shear stress

- τ_o^{\max} : Initial shear stress
 β : Constant for time-dependent frictional force
 $\Delta\delta_s^f$: Effective relative shear displacement to failure.

Conflict of Interests

The authors declare that there is no conflict of interests regarding the publication of this paper.

Acknowledgment

This work was supported by 2016 Korea Aerospace University Faculty Research Grant.

References

- [1] Y. Liu and I. Szlufarska, "Chemical origins of frictional aging," *Physical Review Letters*, vol. 109, no. 18, Article ID 186102, 2012.
- [2] J. H. Dieterich, "Modeling of rock friction: 1. Experimental results and constitutive equations," *Journal of Geophysical Research*, vol. 84, no. 5, pp. 2161–2168, 1979.
- [3] K. M. Frye and C. Marone, "Effect of humidity on granular friction at room temperature," *Journal of Geophysical Research*, vol. 107, no. B11, pp. ETG 11-1–ETG 11-13, 2002.
- [4] Q. Li, T. E. Tullis, D. Goldsby, and R. W. Carpick, "Frictional ageing from interfacial bonding and the origins of rate and state friction," *Nature*, vol. 480, no. 7376, pp. 233–236, 2011.
- [5] R. Capozza, I. Barel, and M. Urbakh, "Probing and tuning frictional aging at the nanoscale," *Scientific Reports*, vol. 3, article 1896, 2013.
- [6] K. Kim, "Creep-rupture model of aluminium alloys: cohesive zone approach," *Proceedings of the Institution of Mechanical Engineers*, vol. 299, no. 8, pp. 1343–1347, 2015.
- [7] K. Kim and M.-J. Yoon, "Fretting fatigue simulation for aluminium alloy using cohesive zone law approach," *International Journal of Mechanical Sciences*, vol. 85, no. 1, pp. 30–37, 2014.
- [8] K. Kim, B. Forest, and J. Geringer, "Two-dimensional finite element simulation of fracture and fatigue behaviours of alumina microstructures for hip prosthesis," *Proceedings of the Institution of Mechanical Engineers, Part H: Journal of Engineering in Medicine*, vol. 225, no. 12, pp. 1158–1168, 2011.
- [9] K. Kim, "Softening behaviour modelling of aluminium alloy 6082 using a non-linear cohesive zone law," *Proceedings of the Institution of Mechanical Engineers, Part L: Journal of Materials: Design and Applications*, vol. 229, no. 5, pp. 431–435, 2015.
- [10] M. Zou and D. Yang, "Nanoindentation of silica nanoparticles attached to a silicon substrate," *Tribology Letters*, vol. 22, no. 2, pp. 189–196, 2006.
- [11] A. Sackfield, D. A. Hills, and D. Nowell, *Mechanics of Elastic Contacts*, Butterworth-Heinemann, Oxford, UK, 1st edition, 1993.